Study on Nitride-based Light Emitting Diodes Grown on Nano-structured Templates

Cao MIAO

TABLE OF CONTENTS

1. Introduction

1.1 Advantages of the III-nitride Material System

In the past decades, the semiconductor technology has fundamentally changed our daily lives.

Nowadays, the semiconductor devices and components are almost indispensible in every field,

such as economy, education, industry, entertainment and so on. The materials supporting the

tremendous industry are silicon, which is used for the fabrication of the integrated circuits, and

III-V compound semiconductors such as GaAs, which is usually used in telecommunication based

on optical fiber network. The emerging III-nitrides material system, which includes GaN, InN,

AlN as well as their alloys has gained much research interest from worldwide. This material

system has many distinct properties. III nitrides are wide, direct bandgap semiconductors. The

bandgap energy of their alloys covers a wide range from 0.7 eV for InN and 3.4 eV for GaN to 6.1

eV for AlN at room temperature, corresponding to a spectrum from near infrared until deep

ultraviolet. This makes it very suitable for short wavelength optoelectronic devices, such as

ultraviolet or blue light emitting diodes and laser diodes.[1] Besides, The physical and chemical

properties of the III-nitrides are very stable. The strong chemical bonds of the nitrides makes the

material very resistant to high temperature and chemical corrosion.[2,3] GaN and AlGaN have very

high breakdown voltage and high electron velocity. The breakdown field for Si is 2×10^5 V/cm, for

GaAs 4×10^5 V/cm, and for GaN it is 3×10^6 V/cm.[4,5] The Monte Carlo simulated peak electron

velocity in GaN is close to 3×10^7 cm/s and the saturation velocity is 1.5×10^7 cm/s, considerably

higher than the values for Si and GaAs.[6] The different peak and saturation velocities are due to

the intervalley transfer of carriers. Moreover, III-nitrides and their alloys could form p-n junctions

and heterostructures such as InGaN/GaN multiple quantum wells (MQWs), GaN/AlGaN MQWs

and superlattices. These structures makes it possible to fabricate modern semiconductor devices

such as light emitting diodes,[7-10] laser diodes,[11-14] and high electron mobility transistors.[15-18]

1.2 Advantages of the Nitride-based LEDs

Among the applications of nitride semiconductors, light emitting diodes are now enjoying the

largest application and a very rapid growing market. Not only short wavelength LEDs such as blue,

violet, ultraviolet LEDs could be fabricated with III-nitride materials, but also white LEDs for

general illumination could be realized by combine the blue LED with yellow phosphors.

Compared to the traditional light source such as incandescent lamps or fluorescent lamps, the

nitride based LEDs, which is also mentioned as solid state lighting, have a lot of advantages. First

and foremost, the nitride based LEDs have a much higher energy conversion efficiency. At present,

the commercial white LED lamps have reached a luminous efficacy of about 150 lm/W.[19] The

consumed energy is just 1/5 of the incandescent lamps and 1/2 of the fluorescent lamps. A high

luminous efficacy over 300 lm/W with good color rending has been theoretically predicted.[20]

Since lighting consumes about 22% of the generated electricity, and two-thirds of that

energy is wasted as heat during the light generation process, the energy saving would

be substantial. Besides, energy saving will also help improve the environment since

lower energy consumption results in less emission of CO_2 and other waste such as

SO_2 from the power plants. Compared with fluorescent lamps, nitride-based LEDs don't contain poisonous chemicals such as mercury. The nitride based LEDs have a much smaller volume, so apparatus with LEDs as the light source would have less weight and a much compact volume. The life time of LEDs is about 50000 hours in contrast to the life time of 2000 hours for incandescent lamps and 10000 hours for fluorescent lamps, respectively. Nitride based high-efficiency light emitting diode has already been widely used as traffic signals, large panel display, indoor and outdoor illumination, backlighting of LCDs, the headlights of vehicles, and so on.

1.3 Critical Issues for Improving the LED Efficiency

Despite the great success of the nitride based LEDs, there are still some fundamental factors that restrains the LED efficiency. Firstly, due to the lack of lattice-matched templates, the GaN material was grown on foreign substrates such as sapphire or silicon carbide. In a long history, single crystal GaN film could not be obtained due to the large lattice and thermal mismatch between GaN and the foreign substrates. In 1989, Akasaki and Amano et al. reported for the first time high-quality single crystal GaN film with mirror-like surface by introducing a low-temperature AlN buffer layer.[21,22] Although single-crystal GaN films grown on c-plane sapphire templates with low-temperature buffer technology still exhibit a typical dislocation density in the range of $10^8 \sim 10^{10}$ cm^{-2}, highly efficient nitride based short-wavelength light emitting diodes have been successfully realized and commercialized.

Table 1.1 Lattice and thermal expansion mismatch between GaN
and various candidate substrates.[23]

Material	Lattice constant (Å)	Coefficient of thermal expansion (10^{-6}/K)	Lattice mismatch of GaN on material (%)	Thermal mismatch with GaN (%)
GaN	a = 3.189 c = 5.185	5.59 3.17	-	-
AlN	a = 3.111 c = 4.978	4.20 5.30	2.4	25
Si (111)	a = 5.430 a_{eff} = 3.840	3.59	-16.9	54
ZnO	a = 3.2496 c = 5.2065	5.2065	1.8	7
Sapphire	a = 4.758 c = 12.99 a_{eff} = 2.747	7.50 8.5	16	-34
6H-SiC	a = 3.080 c = 15.120	4.2	3.5	25

To further improve the device performance, various methods have been studied to improve the

GaN crystal quality. It was reported that by intentionally prolong the three dimensional growth,

the dislocation density could be reduced.[24-26] However, with longer three dimensional growth

time, the time needed for island coalescence will be accordingly longer, therefore, there is a

tradeoff between the crystal quality and film thickness. Epitaxial lateral overgrowth (ELO) was

another effective way to drastically reducing the dislocation density.[27-30] This technology uses

micro scale dielectric patterns as growth mask. At the overgrown "wing" region, the dislocation

density could be drastically reduced.[31] However, at the window region, the dislocation from the

underlying template will penetrate into the regrown film, and at the coalescence front at the center

of "wing" region, new dislocation will be generated. Therefore, ELO will form periodic low

dislocation density and high dislocation density regions, which leads to a limited size of applicable

low dislocation area. An attempt to solve the problem of non-uniform dislocation distribution in

ELO is to use the nanoscale ELO (NELO).[32-35] Due to the nanoscale spacing of the mask, the

distribution of the dislocations would become more uniform and high-density dislocation assembly in the microscale ELO would be eliminated. While the dislocation filtering is still effective for dislocation reduction, new dislocation bending mechanism was also reported for NELO. However, NELO technology will also introduce new dislocations at the coalescence front. Therefore, the dislocation reduction will not be as effective when the dislocation density of the template is quite low (~10^8 cm^{-2}).[36] Besides, the NELO will also require a thicker film for coalescence when the spacing of the mask window is larger, sometimes the full coalescence will be very difficult.[37] Patterned sapphire substrate (PSS) technology has become quite mature and has been adopted by many LED epi-wafer companies. PSS is a desirable technology because it can not only reduce dislocation density but also improve the light extraction efficiency.[10,38-40] Compared with the ELO technology, PSS method is more cost-effective since it does not require another regrowth step. Hydride vapour phase epitaxy (HVPE) is a technology to grow high-quality thick GaN substrates.[41-43] Dislocation reduction in this technology was based on the fact that the dislocation density became lower with increasing growth thickness due to dislocation annihilation. By growing to a thickness of 100–300 µm, GaN substrate with dislocation density typically between 10^6 and 10^7 cm^{-2} could be obtained.[44] The critical issue for GaN substrates by HVPE is the relatively high cost.

Another factor that restrains the LED performance is the spontaneous and piezoelectric polarization induced quantum confined quantum stark (QCSE) effect, which causes the separation

5

of the electron and hole wave functions in the multi-quantum wells and results in a reduced

radiative recombination rate.[45-47] According to the theoretical calculation, the QCSE effect could

be almost eliminated when growing MQWs on nonpolar planes such as (1-100) or (11-20) planes,

and the piezoelectric field could also be reduced to 40% in value when growing MQWs on

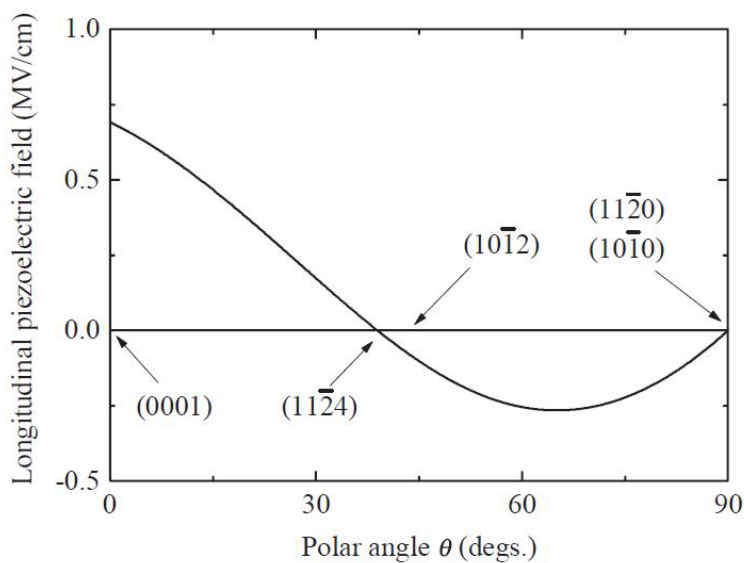semipolar planes such as the (1-101) plane compared with the (0001) orientation.[48,49]

Fig. 1.1 Calculated longitudinal piezoelectric field in strained $GaN_{0.9}In_{0.1}N$
on GaN as a function of the polar angle from (0001).[48]

LED grown on nonpolar or semipolar GaN substrate has been reported by many groups.[50-54]

However, the nonopolar or semipolar GaN films are very expensive and has very limited size,

which makes it less likely for mass production. An alternative way to derive nonpolar or semipolar

planes is to implement the nanostructures. Nonpolar (1-100) and semipolar (1-101) planes are

usually observed when growing GaN nanorods or nanopyramids.[55-57] By growing MQWs on such

templates with nanostructures, it's also possible to reduce QCSE. Besides, due to the nanoscale

size, strain relaxation was usually observed for the nanostructures.[58,59] Strain relaxation will lead

to a reduction of piezoelectric field and hence a further reduction of the QCSE.

Due to the high refractive index of GaN (~2.5), the total reflection angle into the air is only

23.5°. The fraction of light that is emitted into the escape cone is about ≈0.04.[60] A large portion of

the emitted light is confined inside the LED chip and after repeated reflections eventually been
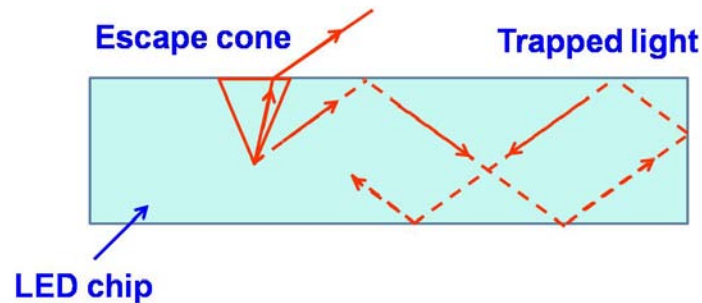
absorbed and dissipated as heat.

Fig. 1.2 Schematic of light trapping inside a LED chip.

The LED external quantum efficiency is calculated as:

External quantum efficiency = internal quantum efficiency (IQE) × light extraction efficiency

(LEE)

For nitride based highly efficient blue LED, the IQE could be around 90%. A main factor

limiting the device performance is the light extraction efficiency. There are a lot of reports on

improving the LEE, for example, by surface roughening or texturing,[61-63] by using microscale or

nanoscale structures such as nanopillar or nanoporous templates,[64,65] or by using patterned

sapphire substrates.[38,39]

7

1.4 Organization of This Thesis

In this thesis, aiming at the above mentioned critical issues, we designed and studied several novel nanostructures which has the potential to improve the LED performance.

In Chapter 2, the metalorganic vapour phase epitaxy (MOVPE) growth system and the common characterization systems were introduced.

In chapter 3, first, the nanoscale patterning with nanoimprint was introduced. Then, the fabrication processes of the nanohole-patterned SiO_2 mask as well as the the nanohole-patterned GaN templates were introduced.

In chapter 4, we propose a novel thermal etching process for nanoporous template fabrication. Compared with common nanostructures fabricated by dry etching, the thermal etching method was dislocation sensitive, which could greatly increase the crystal quality. Meanwhile, dense embedded voids with lengths more than 1 µm were formed, which could greatly enhance the light extraction efficiency. The applications of the nanoporous templates to overgrown GaN as well as InGaN/GaN MQWs were characterized in detail. However, the QCSE could not be reduced by such structure since the MQWs were still grown on the coalesced planar c-plane surface.

In chapter 5, MQWs were directly grown on the semipolar (1-101) planes of the GaN nanopyramids to reduce the QCSE. Until now, in all the reported GaN nanopyramid based LEDs, unlike the microscale pyramids, the size of the nanopyramids was restricted by the mask window. We realized highly uniform nanopyramid arrays with controllable size while abnormal island was completely suppressed. This technology is expected to have a much faster coalescence of p-GaN

layer and thus a reduced serial resistance of the nanopyramid based LED. A larger light emitting

area and a better crystal quality are also expected. The structural and optical properties were

characterized and discussed in detail. However, just like the other reported nanostructures, the

indium composition distribution was not uniform on the nanopyramids. Besides, by forming a flat

p-GaN surface, the light extraction efficiency by such nanostructure will be minimized.

In Chapter 6, we report the results of InGaN/GaN MQWs as well as LEDs grown on regular

nanohole-patterned GaN templates. The MQWs were directly grown the strain relaxed nanohole

template. This structure showed greatly improved light extraction efficiency due to forming

distinct nanostructures. The structural and optical properties of the samples were investigated in

detail.

In Chapter 7, we summarize the results and suggest the future work. A overview of the content

in each chapter is illustrated in Fig. 1.3. The schematic cross-sectional images of crystal structures

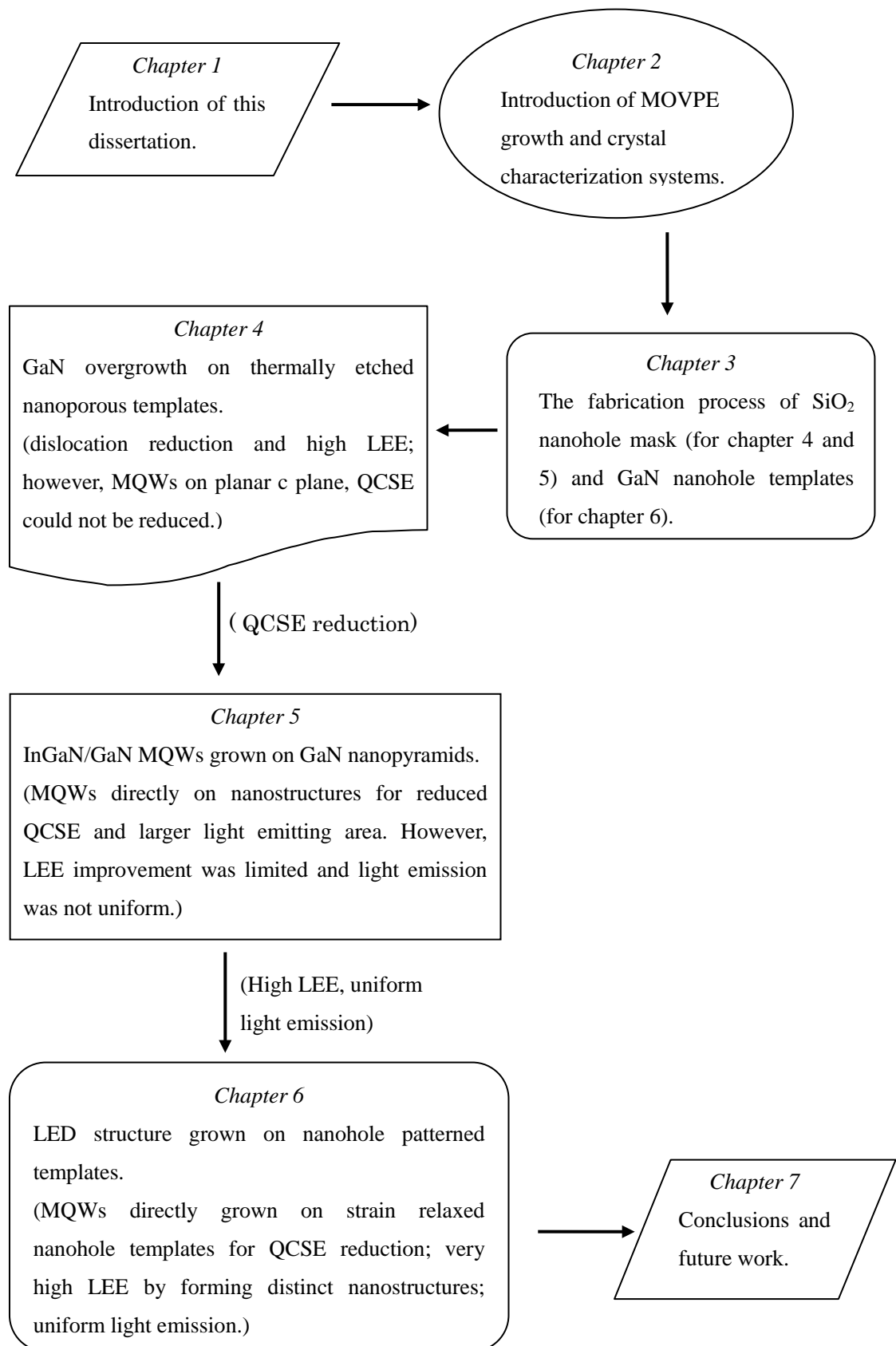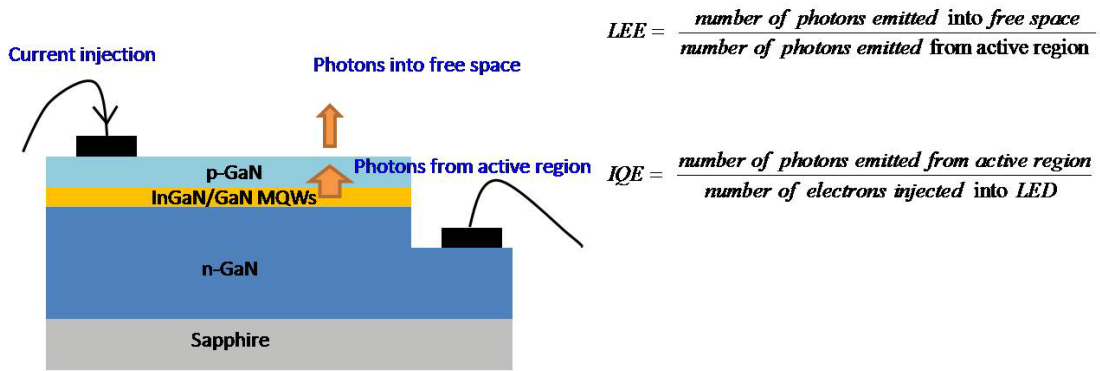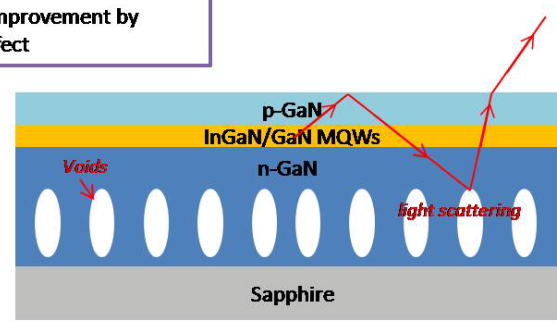studied in this thesis are shown in Fig. 1.4.

Chapter 1
Introduction of this dissertation.

Chapter 2
Introduction of MOVPE growth and crystal characterization systems.

Chapter 4
GaN overgrowth on thermally etched nanoporous templates.
(dislocation reduction and high LEE; however, MQWs on planar c plane, QCSE could not be reduced.)

Chapter 3
The fabrication process of SiO_2 nanohole mask (for chapter 4 and 5) and GaN nanohole templates (for chapter 6).

(QCSE reduction)

Chapter 5
InGaN/GaN MQWs grown on GaN nanopyramids.
(MQWs directly on nanostructures for reduced QCSE and larger light emitting area. However, LEE improvement was limited and light emission was not uniform.)

(High LEE, uniform light emission)

Chapter 6
LED structure grown on nanohole patterned templates.
(MQWs directly grown on strain relaxed nanohole templates for QCSE reduction; very high LEE by forming distinct nanostructures; uniform light emission.)

Chapter 7
Conclusions and future work.

Fig. 1.3 Schematic diagram of the content in each chapter.

$$LEE = \frac{number\ of\ photons\ emitted\ into\ free\ space}{number\ of\ photons\ emitted\ from\ active\ region}$$

$$IQE = \frac{number\ of\ photons\ emitted\ from\ active\ region}{number\ of\ electrons\ injected\ into\ LED}$$

Chapter 4
Mainly LEE improvement by scattering effect

Chapter 5
Higher IQE owing to reduced QCSE in MQWs on semipolar planes; LEE improvement was limited.
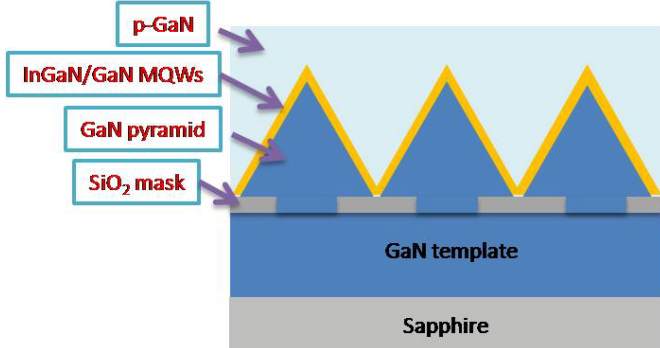
Chapter 6
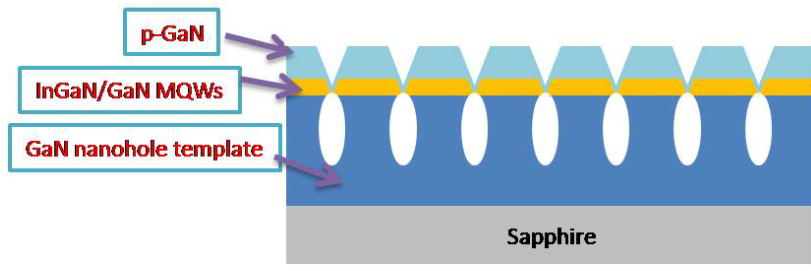Distinct nanostructures for very high LEE; strain relaxed nanohole template for reduced QCSE.

Fig. 1.4. Schematic cross-sectional view images of the crystal structures and research interest in each chapter.

11

References

1) I. Akasaki and H. Amano: Jpn J. Appl. Phys. **36** (1997) 5393.

2) S. C. Jain, M. Willander, J. Narayan, and R. Van Overstraeten: J. Appl. Phys. **87** (2000) 965.

3) M. Razeghi and A. Rogalski: J. Appl. Phys. **79** (1996) 7433.

4) J. L. Hudgins, G. S. Simin, E. Santi, and M. A. Khan: IEEE Trans. Power Electron. **18** (2003) 907.

5) Z. Z. Bandic, P. M. Bridger, E. C. Piquette, T. C. McGill, R. P. Vaudo, V. M. Phanse, and J. M. Redwing: Appl. Phys. Lett. **74** (1999) 1266.

6) B. Gelmont, K. Kim and M. Shur: J. Appl. Phys. **74** (1993) 1818.

7) I. Akasaki, H. Amano, H. Murakami, M. Sassa, H. Kato, and K. Manabe: J. Cryst. Growth **128** (1993) 379.

8) S. Nakamura, T. Mukai and M. Senoh: Appl. Phys. Lett. **64** (1994) 1687.

9) S. Nakamura, N. Senoh, N. Iwasa, and S. I. Nagahama: Jpn. J. Appl. Phys. **34** (1995) L797.

10) K. Tadatomo, H. Okagawa, Y. Ohuchi, T. Tsunekawa, Y. Imada, M. Kato, and T. Taguchi: Jpn. J. Appl. Phys. **40** (2001) L583.

11) S. Nakamura, M. Senoh, S. Nagahama, N. Iwasa, T. Matsushita, and T. Mukai: Appl. Phys. Lett. **76** (2000) 22.

12) I. Akasaki, S. Sota, H. Sakai, T. Tanaka, M. Koike, and H. Amano: Electron. Lett. **32** (1996) 1105.

13) S. Nakamura, M. Senoh, S. Nagahama, N. Iwasa, T. Yamada, T. Matsushita, H. Kiyoku, Y. Sugimoto, T. Kozaki, H. Umemoto, M. Sano, and K. Chocho: Appl. Phys. Lett. **72** (1998) 2014.

14) Y. Yoshizumi, M. Adachi, Y. Enya, T. Kyono, S. Tokuyama, T. Sumitomo, K. Akita, T. Ikegami, M. Ueno, K. Katayama, and T. Nakamura: Appl. Phys. Express **2** (2009) 0921019.

15) M. A. Khan, A. Bhattarai, J. N. Kuznia, and D. T. Olson: Appl. Phys. Lett. **63** (1993) 1214.

16) S. C. Binari, J. M. Redwing, G. Kelner, and W. Kruppa: Electron. Lett. **33** (1997) 242.

17) S. Keller, G. Parish, P. T. Fini, S. Heikman, C. H. Chen, N. Zhang, S. P. DenBaars, U. K. Mishra, and Y. F. Wu: J. Appl. Phys. **86** (1999) 5850.

18) M. A. Khan, J. W. Yang, W. Knap, E. Frayssinet, X. Hu, G. Simin, P. Prystawko, M. Leszczynski, I. Grzegory, S. Porowski, R. Gaska, M. S. Shur, B. Beaumont, M. Teisseire, and G. Neu: Appl. Phys. Lett. **76** (2000) 3807.

19) Y. Narukawa, M. Ichikawa, D. Sanga, M. Sano, and T. Mukai: J. Phys. D-Appl. Phys. **43** (2010) 354002.

20) Y. Uchida and T. Taguchi: Proc. SPIE **4996** (2003) 166.

21) H. Amano, N. Sawaki, I. Akasaki, and Y. Toyoda: Appl. Phys. Lett. **48** (1986) 353.

22) I. Akasaki, H. Amano, Y. Koide, K. Hiramatsu, and N. Sawaki: J. Cryst. Growth **98** (1989) 209.

23) Z. C. Feng, *III-nitride Devices and Nanoengineering*; (Imerial College Press, London, 2008).

24) H. Lahreche, P. Vennegues, B. Beaumont, and P. Gibart: J. Cryst. Growth **205** (1999) 245.

25) D. D. Koleske, A. J. Fischer, A. A. Allerman, C. C. Mitchell, K. C. Cross, S. R. Kurtz, J. J. Figiel, K. W. Fullmer, and W. G. Breiland: Appl. Phys. Lett. **81** (2002) 1940.

26) R. Gutt, L. Kirste, T. Passow, M. Kunzer, K. Kohler, and J. Wagner: Phys. Status Solidi B-Basic Solid State Phys. **247** (2010) 1710.

27) K. Hiramatsu, K. Nishiyama, A. Motogaito, H. Miyake, Y. Iyechika, and T. Maeda: Phys. Status Solidi A. **176** (1999) 535.

28) X. Zhang, P. D. Dapkus and D. H. Rich: Appl. Phys. Lett. **77** (2000) 1496.

29) T. S. Zheleva, S. A. Smith, D. B. Thomson, T. Gehrke, K. J. Linthicum, P. Rajagopal, E. Carlson, W. M. Ashmawi, and R. F. Davis: MRS INTERNET JOURNAL OF NITRIDE

SEMICONDUCTOR RESEARCH **41** (1999) G3.

30) K. Hiramatsu, K. Nishiyama, M. Onishi, H. Mizutani, M. Narukawa, A. Motogaito, H. Miyake, Y. Iyechika, and T. Maeda: J. Cryst. Growth **221** (2000) 316.

31) O. H. Nam, M. D. Bremser, T. S. Zheleva, and R. F. Davis: Appl. Phys. Lett. **71** (1997) 2638.

32) S. D. Hersee, D. Zubia, X. Y. Sun, R. Bommena, M. Fairchild, S. Zhang, D. Burckel, A. Frauenglass, and S. Brueck: IEEE J. Quantum Electron. **38** (2002) 1017.

33) C. H. Chiu, D. W. Lin, Z. Y. Li, C. H. Chiu, C. L. Chao, C. C. Tu, H. C. Kuo, T. C. Lu, and S. C. Wang: Jpn. J. Appl. Phys. **49** (2010) 105501.

34) Y. D. Wang, K. Y. Zang, S. J. Chua, S. Tripathy, P. Chen, and C. G. Fonstad: Appl. Phys. Lett. **87** (2005) 251915.

35) C. H. Chiu, C. C. Lin, H. V. Han, C. Y. Liu, Y. H. Chen, Y. P. Lan, P. C. Yu, H. C. Kuo, T. C. Lu, S. C. Wang, and C. Y. Chang: Nanotechnology **23** (2012) 045303.

36) M. J. Kappers, R. Datta, R. A. Oliver, F. Rayment, M. E. Vickers, and C. J. Humphreys: J. Cryst. Growth **300** (2007) 70.

37) Y. Fu, F. Yun, Y. T. Moon, U. Ozgur, J. Q. Xie, X. F. Ni, N. Biyikli, H. Morkoc, L. Zhou, D. J. Smith, C. K. Inoki, and T. S. Kuan: J. Appl. Phys. **99** (2006) 033518.

38) C. T. Chang, S. K. Hsiao, E. Y. Chang, Y. L. Hsiao, J. C. Huang, C. Y. Lu, H. C. Chang, K. W. Cheng, and C. T. Lee: IEEE Photonics Technol. Lett. **21** (2009) 1366.

39) E. H. Park, J. Jang, S. Gupta, I. Ferguson, C. H. Kim, S. K. Jeon, and J. S. Park: Appl. Phys. Lett. **93** (2008) 191103.

40) J. H. Lee, D. Y. Lee, B. W. Oh, and J. H. Lee: IEEE Trans. Electron Devices **57** (2010) 157.

41) A. Usui, H. Sunakawa, A. Sakai, and A. A. Yamaguchi: Jpn. J. Appl. Phys. **36** (1997) L899.

42) R. J. Molnar, W. Gotz, L. T. Romano, and N. M. Johnson: J. Cryst. Growth **178** (1997) 147.

43) X. P. Xu, R. P. Vaudo, C. Loria, A. Salant, G. R. Brandes, and J. Chaudhuri: J. Cryst. Growth

246 (2002) 223.

44) J. A. Freitas: J. Phys. D Appl. Phys. **43** (2010) 073001.

45) T. Takeuchi, S. Sota, M. Katsuragawa, M. Komori, H. Takeuchi, H. Amano, and I. Akasaki: Jpn. J. Appl. Phys. **36** (1997) L382.

46) S. F. Chichibu, T. Sota, K. Wada, O. Brandt, K. H. Ploog, S. P. DenBaars, and S. Nakamura: Phys. Status Solidi A. **183** (2001) 91.

47) J. H. Ryou, P. D. Yoder, J. P. Liu, Z. Lochner, H. Kim, S. Choi, H. J. Kim, and R. D. Dupuis: IEEE J. Sel. Top. Quantum Electron. **15** (2009) 1080.

48) T. Takeuchi, H. Amano and I. Akasaki: Jpn J. Appl. Phys. **39** (2000) 413.

49) A. E. Romanov, T. J. Baker, S. Nakamura, and J. S. Speck: J. Appl. Phys. **100** (2006) 023522.

50) H. Masui, S. Nakamura, S. P. DenBaars, and U. K. Mishra: IEEE Trans. Electron Devices **57** (2010) 88.

51) K. C. Kim, M. C. Schmidt, H. Sato, F. Wu, N. Fellows, Z. Jia, M. Saito, S. Nakamura, S. P. DenBaars, and J. S. Speck: Appl. Phys. Lett. **91** (2007) 181120.

52) T. Detchprohm, M. W. Zhu, Y. F. Li, Y. Xia, C. Wetzel, E. A. Preble, L. H. Liu, T. Paskova, and D. Hanser: Appl. Phys. Lett. **92** (2008) 241109.

53) M. Funato, M. Ueda, Y. Kawakami, Y. Narukawa, T. Kosugi, M. Takahashi, and T. Mukai: Jpn. J. Appl. Phys. **45** (2006) L659.

54) H. Sato, A. Tyagi, H. Zhong, N. Fellows, R. B. Chung, M. Saito, K. Fujito, J. S. Speck, S. P. DenBaars, and S. Nakamura: Phys. Status Solidi -R **1** (2007) 162.

55) S. D. Hersee, X. Y. Sun and X. Wang: Nano Lett. **6** (2006) 1808.

56) Y. H. Ko, J. H. Kim, L. H. Jin, S. M. Ko, B. J. Kwon, J. Kim, T. Kim, and Y. H. Cho: Adv. Mater. **23** (2011) 5364.

57) R. Leute, D. Heinz, J. Wang, F. Lipski, T. Meisch, K. Thonke, J. Thalmair, J. Zweck, and F.

Scholz: J. Cryst. Growth **370** (2013) 101.

58) J. Bai, Q. Wang and T. Wang: J. Appl. Phys. **111** (2012) 113103.

59) V. Ramesh, A. Kikuchi, K. Kishino, M. Funato, and Y. Kawakami: J. Appl. Phys. **107** (2010) 114303.

60) A. I. Zhmakin: Phys. Rep.-Rev. Sec. Phys. Lett. **498** (2011) 189.

61) H. Kasugai, Y. Miyake, A. Honshio, S. Mishima, T. Kawashima, K. Iida, M. Iwaya, S. Kamiyama, H. Amano, I. Akasaki, H. Kinoshita, and H. Shiomi: Jpn. J. Appl. Phys. **44** (2005) 7414.

62) T. Fujii, Y. Gao, R. Sharma, E. L. Hu, S. P. DenBaars, and S. Nakamura: Appl. Phys. Lett. **84** (2004) 855.

63) I. Schnitzer, E. Yablonovitch, C. Caneau, T. J. Gmitter, and A. Scherer: Appl. Phys. Lett. **63** (1993) 2174.

64) H. M. Kim, Y. H. Cho, H. Lee, S. I. Kim, S. R. Ryu, D. Y. Kim, T. W. Kang, and K. S. Chung: Nano Lett. **4** (2004) 1059.

65) P. Frajtag, J. P. Samberg, N. A. El-Masry, N. Nepal, and S. M. Bedair: J. Cryst. Growth **322** (2011) 27.

2. Metalorganic Vapour Phase Epitaxy and Characterization Systems

2.1 MOVPE Growth System

In this research, we used an MOVPE equipment for nitride growth. Samples were grown in a horizontal MOVPE reactor made by EpiQuest, Inc. Figure 2.1 shows the growth chamber and the loadlock chamber that are connected with a transfer gate. The loadlock chamber configuration decreases the possibility of contaminating the growth chamber when setting samples into the chamber. During growth the chamber pressure was controlled manually by a valve and the chamber pressure was constantly monitored. The growth pressure could be varied from about 100 Torr to 760 Torr when using the standard flow rates.
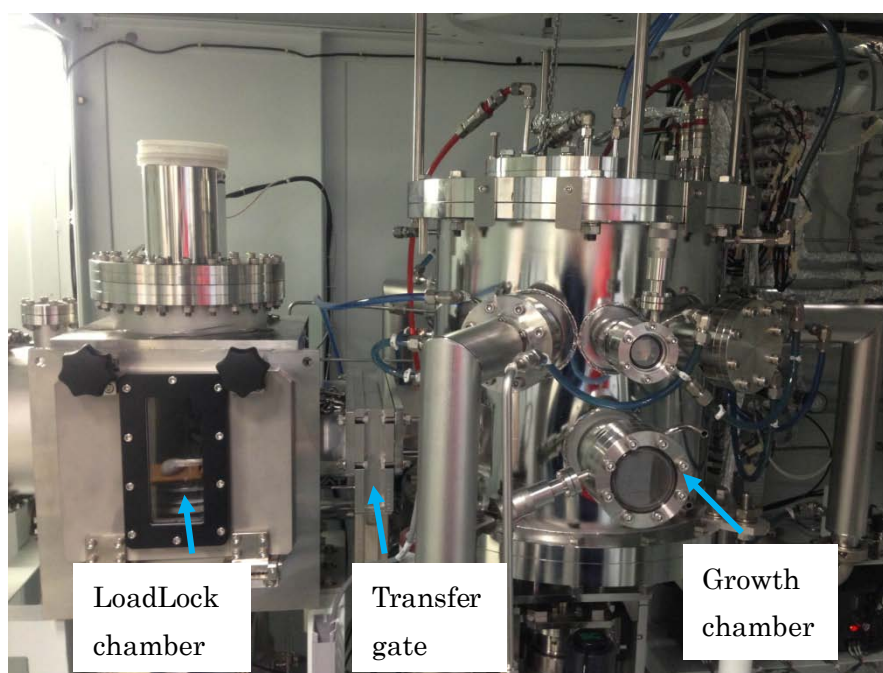
Fig. 2.1 Photograph of the growth chamber and the loadlock chamber.

The schematic of the MOVPE system is shown in Fig. 2.2. Trimethalgallium (TMG), Trimethalaluminum (TMA), Trimethalindium (TMI), and Triethalgallium (TEG) are used as III

precursors, ammonia with purity of 5N is used as the V precursor. Bis-ethylcyclopentadienyl magnesium (EtCp$_2$Mg) was used as the dopant for p-GaN growth, and (CH$_3$)$_4$Si was used as dopant for n-GaN growth. Purified hydrogen and nitrogen were used as the carrier gas. The III precursors and ammonia are introduced into the growth chamber separately to avoid the parasitic reaction. The precursors were mixed just before reaching the susceptor. This is realized by optimizing the flow rates of the MO pushing line and ammonia pushing line. The III-line and V-line could both be introduced into the chamber or be directed to a bypass line by switching the valves. When switching the flows into the growth chamber, a dummy line with the same flow rate is always used in order to keep the flow inside the chamber stable. This machine is initially designed for atomic layer deposition of III-nitrides, therefore the valves controlling the precursors into the growth chamber have a very high switching speed of 0.1 s. There are three gas flows introduced into the flow channel: the ammonia flow is at the bottom to make more efficient decomposition of the ammonia. At the middle it is the III-line flow. The n and p dopants are also introduced from the III-line. At the top there is a sub-flow to "press" the precursors, making them more effectively react on the susceptor. The susceptors are coated with BN or SiC, and the susceptor temperature is detected by a thermal couple right beneath the susceptor and controlled by PID control. There are susceptors for 1 piece 4" wafer or 3 pieces of 2" wafers. Still we can use even smaller pieces of templates (a quarter of 2" wafer or 1×1 cm^2) for growth along with dummy templates.
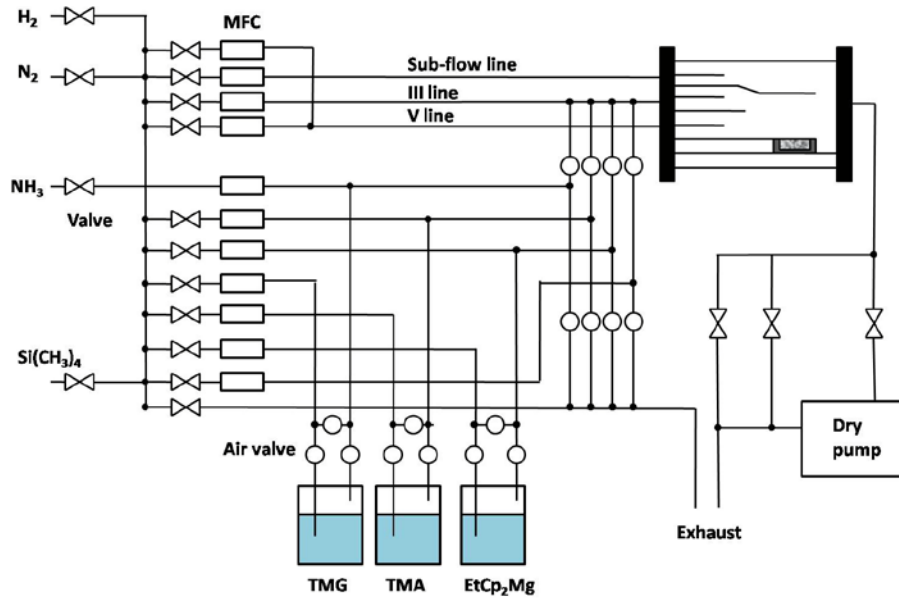
Fig. 2.2 A schematic of the MOVPE system.

Some of the samples were also grown by MOVPE with a showerhead configuration. The showerhead structure is shown in Fig. 2.3.
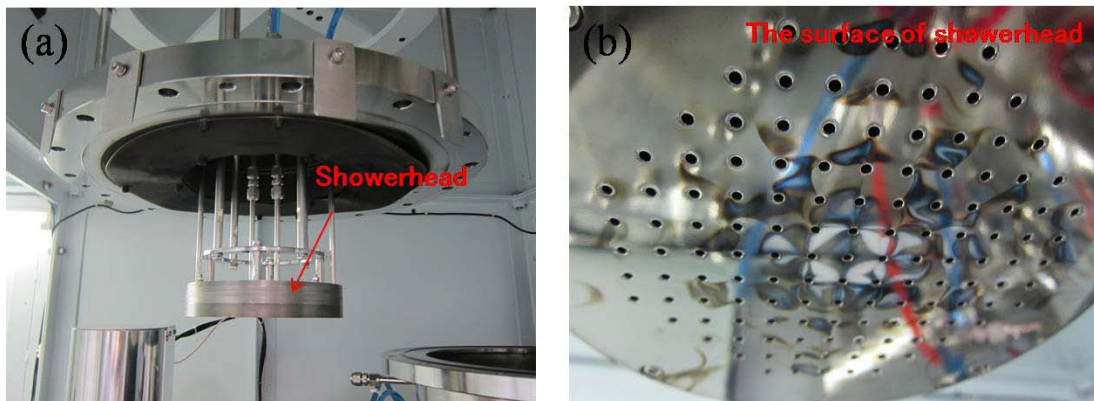

Fig. 2.3 (a) photograph of the showerhead structure, (b) photograph of the surface of the showerhead structure.

2.2 Introduction of Nitride Growth Process

Typical growth process for the GaN templates used in this research are shown in
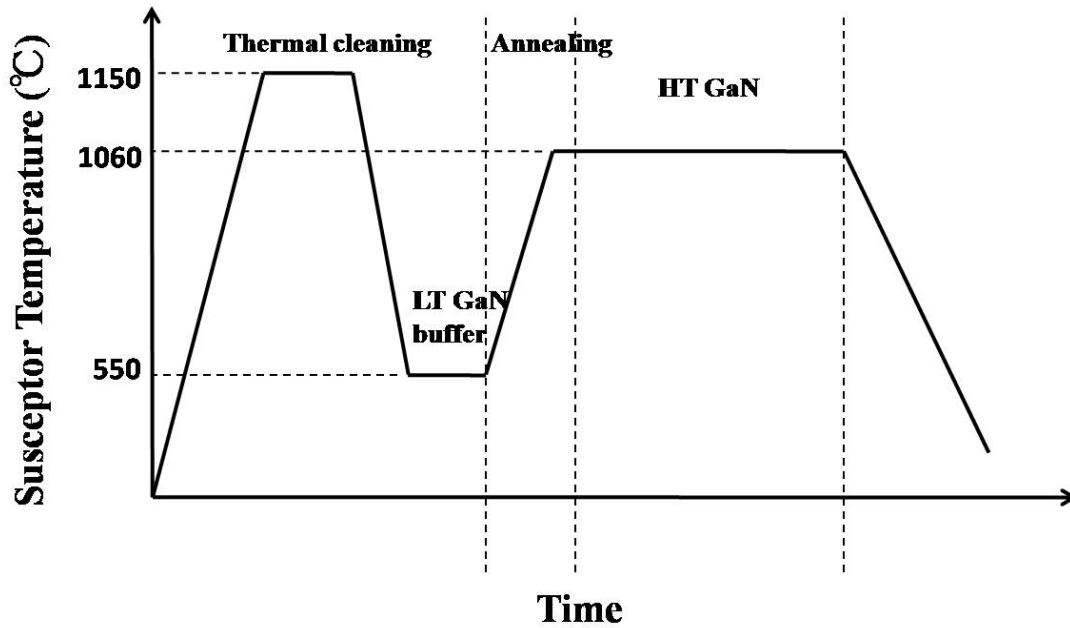
Figure 2.4.

Fig. 2.4 Typical growth process of the GaN templates.

Growth conditions for GaN templates are summized in Table 2.1. 0.2^{o} off cut c-plane sapphire substrates (Namiki Precision Jewel Co., Ltd.) were used. The steps including high temperature (HT) cleaning, low temperature (LT) nucleation, annealing of LT buffer layer, and HT GaN growth are crucial for high quality GaN films.[1,2] The growth process of the undoped GaN template using the showerhead structure is similar to that of the side flow structure. The undoped GaN templates are generally n-type with a background elctron of ~3×10^{16} cm^{-3}, which may be caused by nitrogen vacancies [3] or unintentioally incorporated impurities such as oxygen.[4]

Table 2.1 Typical growth condition for GaN templates.

	LT GaN buffer	HT GaN
Temperature (℃)	550	1100
Pressure (Torr)	500	500
NH_3 flow rate (sccm)	5000	5000
TMG Flow rate (sccm)	6	20
V/III ratio	7145	2144
Growth time (min)	7	60

For the growth of InGaN/GaN MQWs, to effectively incorporate indium, nitrogen is usually used as the carrier gas instead of hydrogen. A large ammonia flow could be used to suppress the decomposition of InGaN. The typical InGaN growth temperature used in this research was between 730~800 ^{o}C. Different growth temperatures of the InGaN quantum well and the GaN barrier layer were sometimes used in previous reports to improve the barrier crystal quality. In our experiment, a higher barrier growth temperature didn't show obvious improvement of the crystal quality, which might be due to the decomposition of the InGaN wells. Therefore, a constant temperature is used for InGaN well and GaN barrier growth. A typical InGaN/GaN MQWs growth process is shown in Fig. 2.5. The coresponding growth parameters are listed in Table 2.2. Here we used a relatively high growth rate for the InGaN quantum wells. In order to keep a blue emission with a wavelength around 450 nm, decreasing the growth rate will lead to a lower indium incorporation, which requires to decrease the growth temperature to keep the indium composition almost the same. Although the InGaN well growth condion was not fully optimized, we found this condtion gave an intense photoluminescence (PL) emission and satisfied our experimental porpose

for comparison of the different templates. Before regrowth of the MQWs, the fabricated templates

were thermal cleaned at 950 ^{o}C for 5 min to remove possible contaminations or surface impurities

such as oxygen. No higer thermal cleaning temperatuer was used in order to prevent the
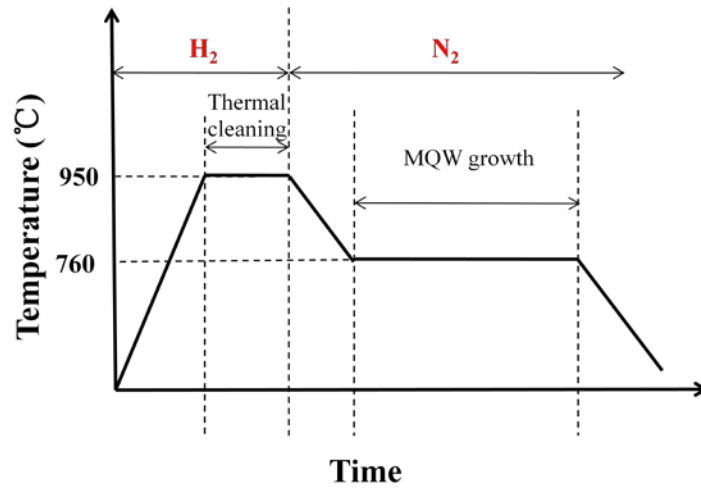
deformation and desorption of the nanostructures.

Fig. 2.5 Typical growth process of InGaN/GaN MQWs.

Table 2.2 Typical growth condition of InGaN/GaN MQWs.

	GaN barrier	InGaN well
TEG (μmol/min)	15.56	15.56
TMI (μmol/min)	--	10.38
TMI/(TEG+TMI)	--	0.56
NH$_3$ (SLM)	8	8
Growth Temp. (℃)	760	760
Pressure (Torr)	500	500
Process Time (min)	6	1

The growth conditions of the p-GaN, n-GaN, and AlGaN electron blocking layer were investigated using the showerhead configuration.

The growth condition of n-GaN was based on the undoped GaN growth condition. Highly conductive n-GaN layers with an electron concentration of 3.72×10^{18} cm^{-3} and a mobility of 217 cm^2/Vs at room temperature were obtained with a $(CH_3)_4Si$/TMG flow rate ratio of 8.2×10^{-5}.

For AlGaN growth, growth pressure is an important factor. In our experiment, we found it very difficult to incorporate the aluminum when using a pressure of 200 Torr, which was the growth pressure for GaN template. When the growth pressure was decreased to 100 torr, the aluminum was successfully incorporated. This is attributed to a decrease of parasitic reaction, i.e. vapor phase reaction of the precurors before reaching the sample surface, which has been reported in the literature.[5-7] With a TMA/(TMG+TMA) mol fraction of 0.25, AlGaN film with an Al composition ratio of 10% was obtained.

For p-GaN growth condition investigation, we decreased the growth temperature to 950~980 $^{\circ}$C, which is the typical p-GaN growth temperature for the LED strucuture. The lower growth temperature is used to protect the underlying InGaN quantum wells from decomposition. When the growth was conducted at 200 Torr, we found it very difficult to incorporate magesium, which is very similar to the case of AlGaN growth at 200 Torr. When the growth pressure was reduced to 100 Torr, Mg incorporation was obviously improved, which suggested that probably parasitic reaction resulted in the poor magnesium incorporation at the pressure of 200 Torr. The

incorporated Mg concentration could be roughly estimated by the peak position of the PL spectrum.[8] For highly Mg doped GaN films (Mg concentration $> 1\times10^{19}$ cm^{-3}), the GaN bandedge emission usually disappears and another broad blue emission peak at about 430 nm arises.[8-10] This blue emission peak might be related to the transitions from a deep donor to the shallow Mg_{Ga} acceptor.[11] Comparing the room temperature PL spectra of the p-GaN layers in Fig. 2.6, we found a high-concentration Mg incorporation at a $EtCp_2Mg$ flow rate larger than 90 sccm at a pressure of 100 torr.
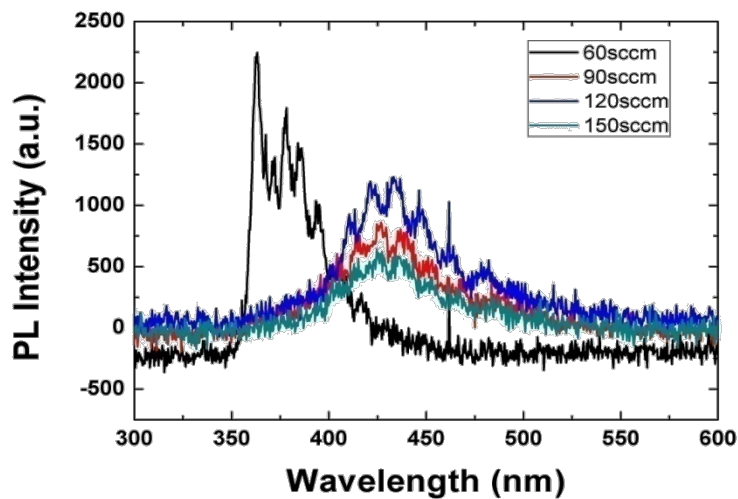
Fig. 2.6 Room temperature PL spectra of the p-GaN layers
with different $EtCp_2Mg$ flow rate at a pressure of 100 Torr.

Secondary ion mass spectrometry (SIMS) of this sample in Fig. 2.7 showed a Mg concentration of 3×10^{19} cm^{-3}. However, including this sample, no p-type conductivity was observed for any of the p-GaN films by Hall measuement. In the SIMS result, we found a drastic increase of carbon concentration when we started to grow p-GaN layer at a lower temperature of 960 ^{o}C, which suggested a great impact of the growth temperature on the film properites. Comparing the Hall

24

measurement results of the undoped GaN films grown under 1100 ^{o}C and 960 ^{o}C, we found a much larger background electron concentration ($>1\times10^{18}$ cm^{-3}) in the film grown at the lower growth temperature compared with a concentration of 3×10^{16} cm^{-3} in the film grown at the higher temperature. To confirm whether the high background electron concentration should account for the difficulty in getting p-type GaN, we performed p-GaN growth at elevated temperatures. Two magnesium-doped GaN films were grown at 1025 ^{o}C and 1050 ^{o}C while keeping other parameters the same as the sample in Fig. 2.7. Although the sample grown at 1025 ^{o}C still showed n-type conductivity, the sample grown at 1050 ^{o}C showed p-type conductivity with a hole concentration of 4.98×10^{17} cm^{-3} and a mobility of 7.2 cm^{2}/Vs. Therefore, the difficulty in realizing p-GaN in our experiment was confirmed to result from the high backgound electron concentration at growth temperatures lower than 1050 ^{o}C. However, the origin of the high background eletron concentration is still unclear. Further optimization of the p-GaN growth condition is required.
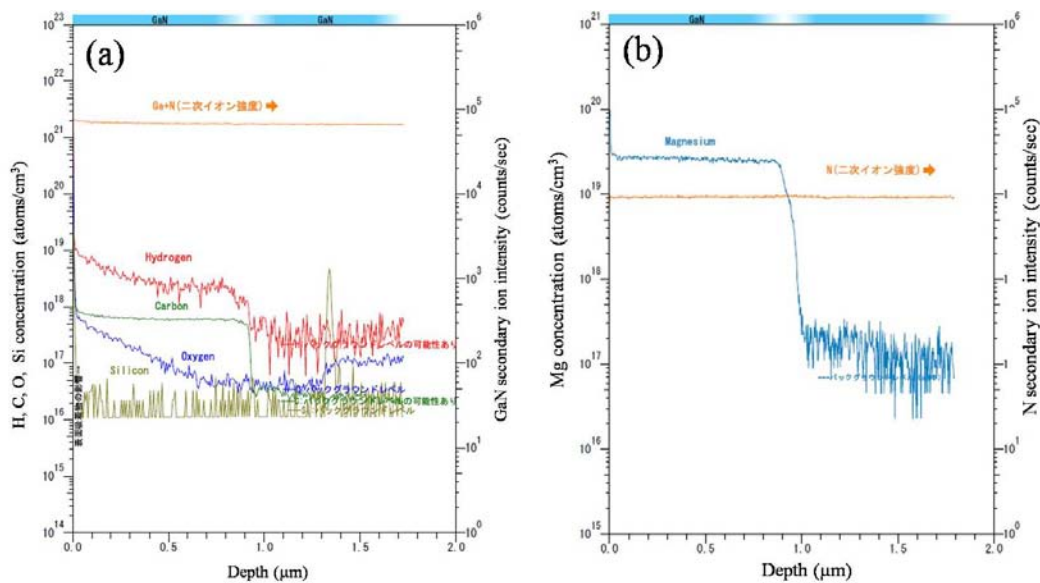

Fig. 2.7 SIMS depth profile of H, C, Si concentrations (a) and Mg concentration (b) of the p-GaN film with a EtCp$_2$Mg flow rate of 90 sccm.

2.3 Characterization Systems

For III-nitride epi-layer characterization, several common characterization systems are used.

PL spectra were measured by a micro PL system using a 325 nm He-Cd laser source. A compact micro PL system with a excitation wavelength of 405 nm was also used for LED structure measurement. Another 405 micro PL system with tunable excitation power was set up for internal quantum efficiency measurement using the method proposed by Dai et al.[12] The excitation power could be varied automatically by switching the neutral density filter, and the integrated PL intensity is automatically calculated by the software.

X-ray diffraction (XRD) is an effective and indispensible way for nitride epi-layer characterization. The XRD equipment (SmartLab, Rigaku) uses a 2-bounce Ge (220) crystal monochromator and a 2-bounce Ge (220) analyzer to improve the resolution. AuK_α target ($\lambda = 1.280100$ Å) is used here instead of the more commonly used CuK_α target ($\lambda = 1.54056$ Å), so the diffraction angle may be different from some other reports. The crystal quality of the GaN template was characterized by the full width of half maximum (FWHM) of the rocking curve scan of the (002) and (102) planes. The FWHM of the (002) is related to the screw dislocation density and that of the (102) plane is related to a combination of the screw and edge dislocation densities.[13] The barrier and well thickness of InGaN/GaN multiple quantum wells grown on c-plane as well as the In composition was derived by the (002) 2θ-ω scan followed by simulation using the software provided by Rigaku assuming the fully strained state of the InGaN quantum wells and the AlGaN electron blocking layer. The thickness as well as the aluminum composition

of the AlGaN electron blocking layer could be derived in a similar way. The strain state of the

MQWs was characterized by reciprocal space mapping of the asymmetrical reflection of the (105)

plane.[14,15]

The surface roughness of the samples are characterized by atomic force microscope (AFM)

(Nanocute, SII NanoTech, Inc.). Unlike the conventional AFM equipment, the laser is integrated

inside the probe, so no special adjustment of the laser is required. The probe-sample contact was

also controlled automatically by the piezoelectric effect of the probe. Therefore, the measurement

is quite automatic and convenient. In this research, the surface roughness of the GaN films and

MQWs was characterized by root mean square (RMS) value. By comparing the number of surface

step terminations, a rough comparison of the dislocation density of the GaN films could be

made.[16,17] The pit density and surface roughness are important values to judge the crystal quality

of the MQWs.

Cathodoluminescence (CL) measurement is an important tool for nitride material

characterization. In this research, panchromatic CL images were used to directly measure the

dislocation densities of the GaN films.[18,19] The CL spectrum of the MQWs could be used to

determine the crystal quality and indium content. The monochromatic CL images of the MQWs on

nanostructures were measured to investigate the microscale origins of light emission at different

wavelengths.[20] The indium composition distribution could also be deduced.

The strain state of the nanostructures such as the nanoporous template was characterized by

Raman measurement. The raman measurement equipment (inVia Raman microscope, Renishaw) utilizes a 532 nm laser source. The resolution of Raman spectrum is 1.5 cm^{-1}. A better resolution could be obtained by fitting the spectra with a commercial software provided with the equipment. Before measurement, the equipment is calibrated with a standard silicon sample. A nearly strain free bulk GaN substrate was usually used as a reference. The strain state of the GaN film was reported to be related to the peak position of the E_2^{high} mode of the Raman spectrum. A redshift from the peak position of strain free state stands for a compressive stress which was usually observed in GaN grown on sapphire substrates; while a blueshift stands for a tensile stress which presents in GaN grown on silicon substrates [21]. The strain relaxation of the GaN film could be calculated by the equation

$$\Delta \omega = k_{Ra, a}\sigma_a,$$

where $k_{Ra, a} = 4.2$ cm^{-1} GPa^{-1} is the Raman factor, σ_a is the biaxial stress, and $\Delta\omega$ is the Raman shift of the E_2^{high} mode.[21]

References

1) I. Akasaki, H. Amano, Y. Kiode, K. Hiramatsu, and N. Sawaki: J. Cryst. Growth **98** (1989) 209.

2) H. Amano, N. Sawaki, I. Akasaki, and Y. Toyoda: Appl. Phys. Lett. **48** (1986) 353.

3) Z. Yang, L. K. Li, J. Alperin, and W. I. Wang: J. Electrochem. Soc. **144** (1997) 3474.

4) B. C. Chung and M. Gershenzon: J. Appl. Phys. **72** (1992) 651.

5) C. H. Chen, H. Liu, D. Steigerwald, W. Imler, C. P. Kuo, M. G. Craford, M. Ludowise, S. Lester, and J. Amano: J. Electron. Mater. **25** (1996) 1004.

6) J. R. Creighton, G. T. Wang, W. G. Breiland, and M. E. Coltrin: J. Cryst. Growth **261** (2004) 204.

7) J. Stellmach, M. Pristovsek, O. Savas, J. Schlegel, E. V. Yakovlev, and M. Kneissl: J. Cryst. Growth **315** (2011) 229.

8) Y. L. Xian, S. J. Huang, Z. Y. Zheng, B. F. Fan, Z. S. Wu, H. Jiang, and G. Wang: J. Cryst. Growth **325** (2011) 32.

9) J. K. Sheu, Y. K. Su, G. C. Chi, B. J. Pong, C. Y. Chen, C. N. Huang, and W. C. Chen: J. Appl. Phys. **84** (1998) 4590.

10) S. Nakamura, N. Iwasa, M. Senoh, and T. Mukai: Jpn J. Appl. Phys. **31** (1992) 1258.

11) M. A. Reshchikov and H. Morkoc: J. Appl. Phys. **97** (2005) 061301.

12) Q. Dai, M. F. Schubert, M. H. Kim, J. K. Kim, E. F. Schubert, D. D. Koleske, M. H. Crawford, S. R. Lee, A. J. Fischer, G. Thaler, and M. A. Banas: Appl. Phys. Lett. **94** (2009) 111109.

13) M. A. Moram and M. E. Vickers: Rep. Prog. Phys. **72** (2009) 036502.

14) S. Pereira, M. R. Correia, E. Pereira, K. P. O'Donnell, E. Alves, A. D. Sequeira, N. Franco, I.

M. Watson, and C. J. Deatcher: Appl. Phys. Lett. **80** (2002) 3913.

15) A. Krost, J. Blasing, M. Lunenburger, H. Protzmann, and M. Heuken: Appl. Phys. Lett. **75** (1999) 689.

16) B. Heying, E. J. Tarsa, C. R. Elsass, P. Fini, S. P. DenBaars, and J. S. Speck: J. Appl. Phys. **85** (1999) 6470.

17) H. Morkoc: Mater. Sci. Eng. R-Rep. **33** (2001) 135.

18) S. J. Rosner, E. C. Carr, M. J. Ludowise, G. Girolami, and H. I. Erikson: Appl. Phys. Lett. **70** (1997) 420.

19) T. Sugahara, H. Sato, M. S. Hao, Y. Naoi, S. Kurai, S. Tottori, K. Yamashita, K. Nishino, L. T. Romano, and S. Sakai: Jpn. J. Appl. Phys. **37** (1998) L398.

20) C. H. Liao, W. M. Chang, Y. F. Yao, H. T. Chen, C. Y. Su, C. Y. Chen, C. Hsieh, H. S. Chen, C. G. Tu, Y. W. Kiang, C. C. Yang, and T. C. Hsu: J. Appl. Phys. **113** (2013) 054315.

21) C. Kisielowski, J. Kruger, S. Ruvimov, T. Suski, J. W. Ager, E. Jones, Z. LilientalWeber, M. Rubin, E. R. Weber, M. D. Bremser, and R. F. Davis: Phys. Rev. B **54** (1996) 17745.

3. Nano-patterned Mask Fabrication

3.1 Nanoimprint Process

For the nanopattern fabrication for nitride growth, several methods have been developed. Electron beam lithography (EBL) can be used to design arbitrary nanopatterns with very high resolution.[1,2] Lift-off method could also be combined with EBL to fabricate other hard etching masks such as nickel, by which the etching selectivity to GaN could be greatly increased. However, the EBL is usually very time consuming and the patterned area is usually quite limited, which limits its application to mass production. Spontaneously formed nanoscale Ni particles by rapid thermal annealing has also been reported for nanopattern fabrication.[3,4] With this method, large scale nanopatterns could be fabricated. However, the distribution of Ni particles is random, and the size and shape of the nanoparticles could not be well controlled, which makes it not suitable for regular pattern fabrication. In this research, nanoimprint lithography (NIL) was used for nanopattern fabrication. Nanoimprint, invented in 1995 by Stephen Y. Chou, is a high-throughput, low-cost nanoscale patterning method.[5] Compared to the above mentioned methods, the NIL technology could fabricate nanopatterns on a very large scale. The nanopatterns could be precisely transferred from the molder to the resist. Very regular patterns could be fabricated with high reproducibility.

In this research, all the nanopatterns were processed by a thermal nanoimprint process. The nanoimprint equipment X500 made by SCIVAX was used. The nanoimprint molder with nanohole pattern was made of silicon and processed by EBL. The patterned area of the molder was 4 inch in

diameter. The nanohole pattern is illustrated in Fig. 3.1.
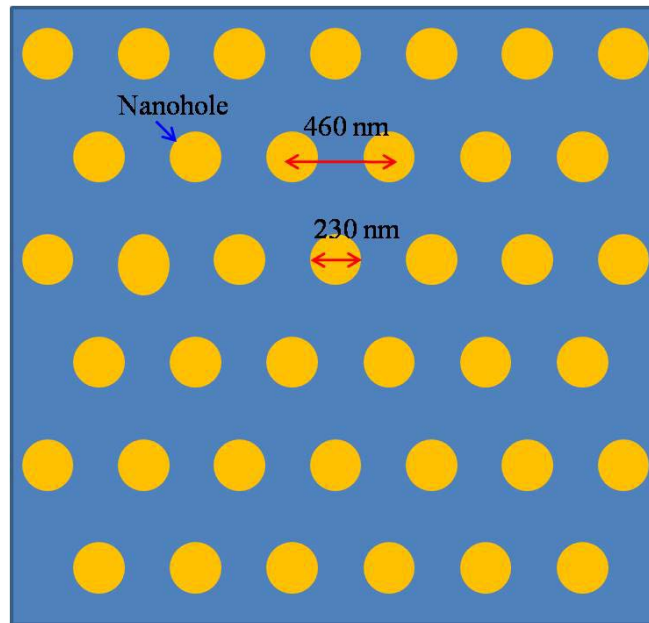

Fig. 3.1 Schematic of the nanohole-pattern distribution
on the silicon molder.

The nanoholes are regularly distributed in a hexagonal geometry. The hole diameter and pitch

was 230 and 460 nm, respectively. The height of the nanopattern was 200 nm. The thickness of the

resist required for such pattern could be easily calculated by keeping constant the resist volume

before and after NIL. The calculated thickness is about 150 nm for the nanohole pattern. With this

thickness the nanopattern will have maximum height and the least residual resist. Then the

nanopattern was transferred to a film (ZF 16-100, Zeon Corporation) by a thermal nanoimprint

process. The films are used as the direct molders for nanopattern fabrication on the wafers. Before

the NIL process, the silicon molders are processed with a release agent (Optool HD-2100Z,

Daikin Industries, Ltd.) for better demolding. This could also protect the nanopatterns on the

molder. After pattern formation, the film was coated with ~20 nm nickel by sputtering to increase

the hardness and lifetime of the film mask. Then the film is also processed with a release agent (Optool HD-1100Z, Daikin Industries, Ltd.) for better demolding. One film could be used for about 10 times or even more with good precision as suggested by the equipment vendor. This greatly increases the lifetime of the silicon molder.

The nanoimprint resist was injected using a syringe capped with a filter to prevent small particles. There were two types of thermal resist used in this research. One was MTR-01 provided by MARUZEN PETROCHEMICAL CO., LTD. The other was NXR-1025 provided by Nanonex. For MTR-01, a 3000 rpm spin coating rate was used. After that, the sample was heated in a vacuum oven at 100 ^{o}C for 30 min and 200 ^{o}C for 20 min for dehydration and finally naturally cooled down to room temperature. For the second resist, a 3500 rpm spin coating rate was used. Then the sample was heated with a hot plate at 150 ^{o}C for 5 min. In both cases, the thickness of the resist was about 150 nm.

The configuration of the nanoimprint parts is illustrated in Fig. 3.2. There was a 8 inch silicon wafer at the upper stage. On the lower stage, one 8 inch silicon wafer was bonded with another 6 inch wafer on top of it. A carbon sheet between the two silicon wafers on the lower stage was used as a "cushion" to prevent the silicon wafer from cracking during the high-pressure pushing process. The silicon wafers with very flat surface was used to obtain a uniform imprint pressure as well as good thermal conductivity. The sample and film mask was placed face-to-face. The upper and lower stages were heated to process temperature during the imprint process, and the cooling of the

stages could be either water cooling or air cooling. The water cooling has much fast cooling speed compared with air cooling. However, if the cooling speed is too high, then the automatic stage control speed, which was used to keep the pressure constant, may not be able to follow the thermal contraction of the resist. Therefore, we used air cooling at high temperatures to keep a good shape of the pattern. After the temperature is decreased, then water cooling is used for a fast cooling speed.
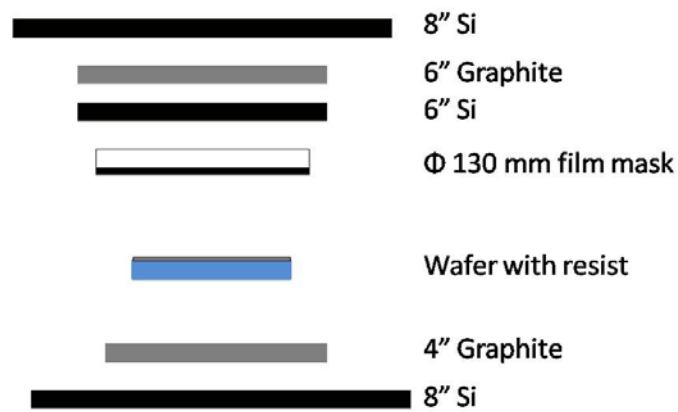

Fig. 3.2 The configuration of the nanoimprint parts.
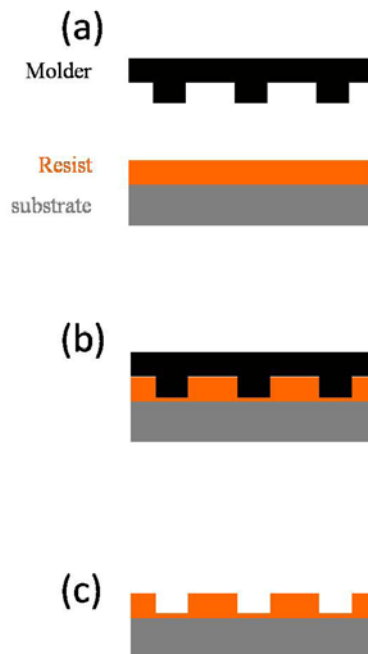
Fig. 3.3 Typical thermal nanoimprint process.

The typical thermal nanoimprint process is illustrated in Fig. 3.3. The process steps of a typical nanoimprint recipe are as follows:

1) Pressurizing: to lower down the upper stage to the position ready for chamber sealing and evacuation.

2) Vacuum: pump down the chamber pressure from atmosphere by -70 KPa to evacuate the air. Without this step, small air bubbles might present between the sample and the film mask. In such case uniform nanopatterns could not be fabricated.

3) Pressurizing: to make the film mask just start to contact with the sample surface by exerting a small load. In this step the upper stage position is controlled with a relatively fast speed to save the process time.

4) Heating: the sample was heated to the glass-transition temperature of the resist provided by the vendors. For MTR-01, the process temperature was 155 ^{o}C, and for NXR-1025, the process temperature was 120 ^{o}C.

5) Pressurizing: during this step, the nanopattern on the film mask was transferred to the resist by pressing the film mask towards the resist with a uniform high pressure. In this research, a high pressure of 8~11 MPa was used.

6) Cooling: The resist was cooled down to make the resist pattern solid. For MTR-01, air cooling was used to decrease the temperature to 125 ^{o}C before taking out the sample. However, for NXR-1025, a lower cooling temperature (~40 ^{o}C) was found to obviously

35

improve the quality of the nanopattern. Therefore, water cooling was used to decrease the temperature to about 40 $^{\circ}$C.

7) Demolding: chamber vent to atmosphere and the upper stage moves upward to the origin position automatically. The film mask automatically detaches from the sample.

The SEM images of the fabricated nanoimprint patterns were shown in Fig. 3.4. Very regularly distributed nanohole patterns were transferred from the film molder to the resist with high precision. The depth of the nanoholes in the resist was about 125 nm, and the residual resist at the bottom of the nanoholes was about 25 nm.
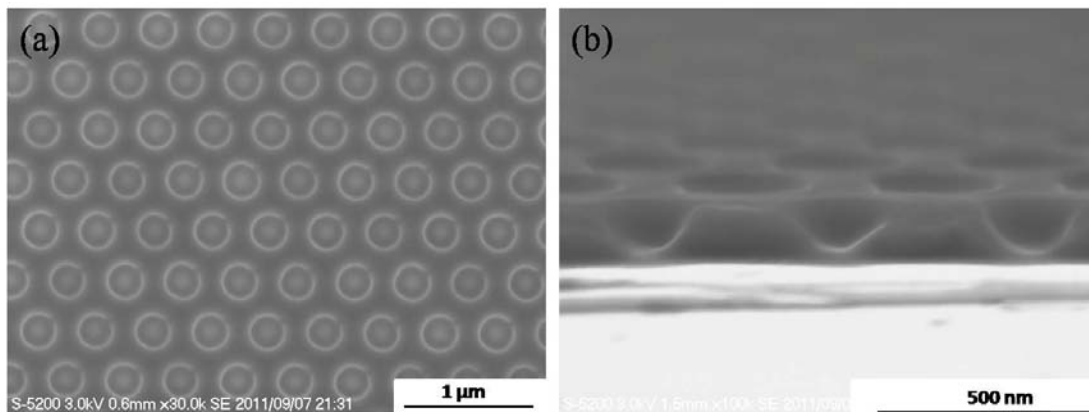
Fig. 3.4 (a) Plan-view and (b) cross-sectional view SEM images of the nanoholepattern formed on the resist after NIL.

3.2 Fabrication of the nanohole SiO$_2$ mask

The nanohole-patterned SiO$_2$ mask used in chapter 4 and chapter 5 was fabricated as follows. 2 inch GaN template with a thickness of 2 μm grown by MOVPE was used for the process. After standard sample cleaning procedure (acetone, methanol, and pure water in ultrasonic for 5 min and

nitrogen blow dry), a SiO_2 layer with a thickness of 45 nm was deposited on the template by

sputtering. The RF power of the sputtering process was 200 W and 20 sccm Ar gas was introduced.

The sputtering rate was 2.2 nm/min. Then a thermal nanoimprint process was used to form the

nanohole patterns on the resist, followed by a dry etching process to transfer the nanohole pattern

from the resist to the SiO_2 mask. A reactive ion etching equipment (RIE-10NR, Samco) was used

for SiO_2 dry etching. The maximum process area was 8 inch in diameter. Within this area, the

etching rate was quite uniform. CF_4 with a flow rate of 20 sccm was used as the etching gas. The

radio frequency (RF) power was 70 W and the chamber pressure was 5 Pa. The etching time was 4

min 30 sec. Here we used a relatively low RF power to reduce the physical bombardment of the

resist and increase the chemical etching effect. This is used to increase the etching selectivity and

achieve a largest possible etching depth. High etching selectivity is not essential for this SiO_2

pattern, but more important in fabricating the GaN nanohole template in chapter 6. This etching

condition will result in a slightly taped side wall due to the increased isotropic chemical etching.

We didn't calculate the average etching rate, since the nanoscale pattern may cause a non-constant

etching rate. Instead, we directly investigated different etching times and checked the etching

result by SEM to investigate the optimal process time. After the dry etching process, the residual

resist was removed by oxygen plasma ashing. This fabrication process is illustrated in Fig. 3.5

with an SEM image of the fabricated SiO_2 nanohole mask.
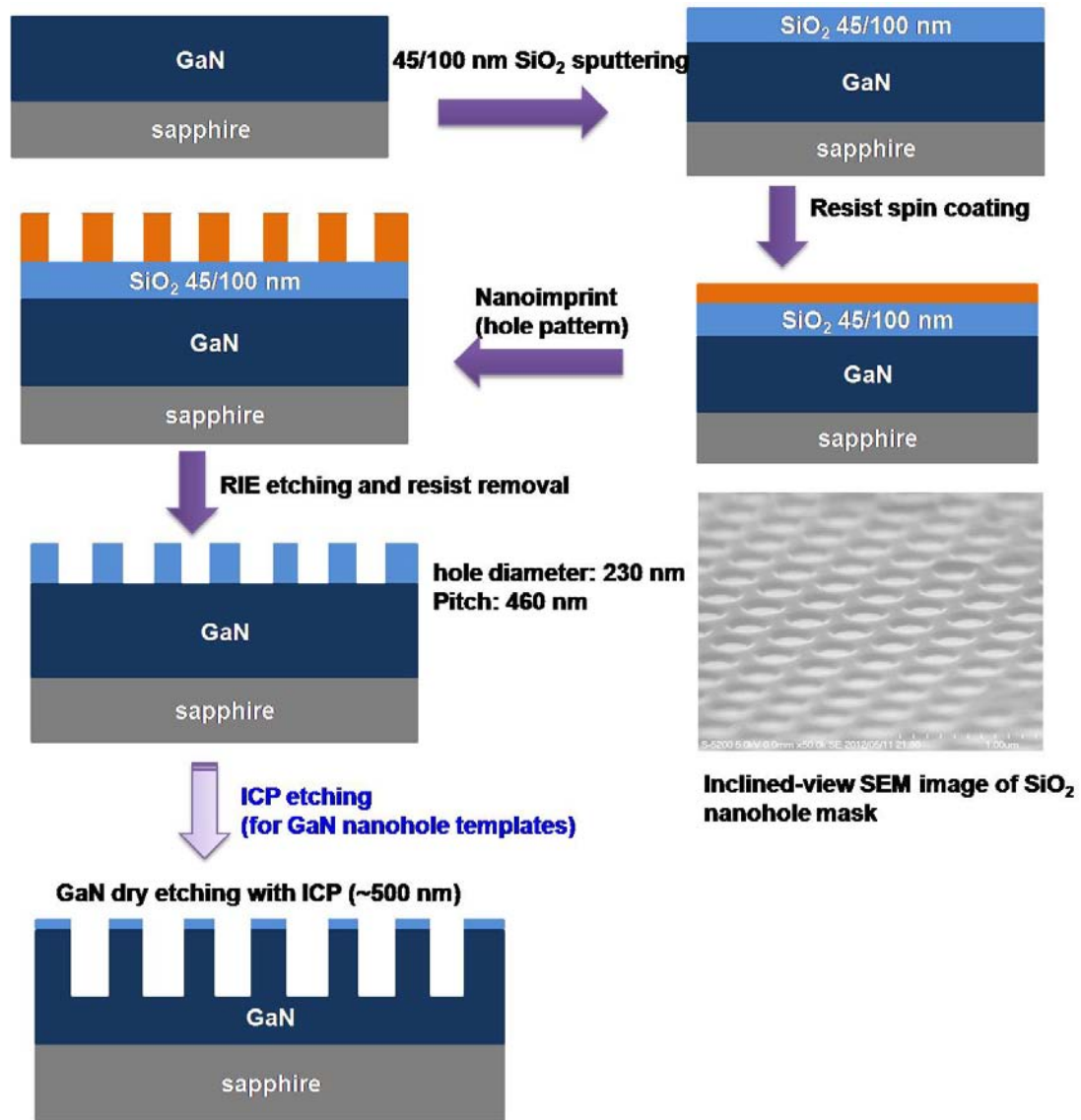
Fig. 3.5 The fabrication process of the SiO$_2$ nanohole mask and an SEM image of the fabricated mask.

3.3 Fabrication of the GaN nanohole template

The process flow of the the GaN nanohole templates used in chapter 6 was also illustrated in

Fig. 3.5. Silicon-doped 2 inch GaN template with a thickness of 3 μm grown by MOVPE was

used for the process. After standard sample cleaning, a SiO$_2$ layer with a thickness of 100 nm was

deposited on the template by sputtering. The RF power of the sputtering was 200 W and 20 sccm

Ar gas was introduced resulting in a sputtering rate of 2.2 nm/min. Then a thermal nanoimprint

process was used to form the nanohole patterns on the resist. The nanohole pattern was transferred

from the resist to the SiO_2 mask by RIE. The etching condition was the same as that mentioned

previously except a longer process time of 6 min. Here 100 nm thick SiO_2 was used in order to get

a SiO_2 nanohole pattern with maximum etching depth. Although relatively lower RF power was

used to increase the etching selectivity of resist to SiO_2, after 6 min etching, the resist was almost

totally etched. The etched SiO_2 thickness is about 85 nm, leaving about 15 nm residual SiO_2

remained in the hole region. In this way, we got the maximum possible etching depth.

Subsequently the sample was loaded into an inductively coupled plasma (ICP) etching chamber

(CE-300IN, ULVAC) for GaN dry etching. Pure Cl_2 was used as the etching gas. The flow rate

was 30 sccm, and the chamber pressure was 5 mTorr. The antenna power was 150 W and the DC

power is 10 W. The high vacuum atmosphere leads to a very anisotropic etching. A low DC power

of 10 W was used to reduce the surface damage. The average etching rate for a planar GaN

template was about 55 nm/min. However, the nanoscale pattern may cause a non-constant etching

rate. We directly investigated different etching times and checked the etching result by SEM. We

adjusted the etching time until the SiO_2 mask almost etched away but still a little thickness 10~15

nm left. In this way, we got the maximum GaN etching depth while keeping the c-plane surface

away from dry etching damage. By 8~10 min dry etching, nanohole pattern with a depth of

400~500 nm could be fabricated.

References

1) F. Barbagini, A. Bengoechea-Encabo, S. Albert, P. Lefebvre, J. Martinez, M. A. Sanchez-Garcia, A. Trampert, and E. Calleja: Microelectron. Eng. **98** (2012) 374.

2) W. H. Goh, G. Patriarche, P. L. Bonanno, S. Gautier, T. Moudakir, M. Abid, G. Orsal, A. A. Sirenko, Z. H. Cai, A. Martinez, A. Ramdane, L. Le Gratiet, D. Troadec, A. Soltani, and A. Ougazzaden: J. Cryst. Growth **315** (2011) 160.

3) H. W. Huang, C. C. Kao, T. H. Hsueh, C. C. Yu, C. F. Lin, J. T. Chu, H. C. Kuo, and S. C. Wang: Mat. Sci. Eng. B-Solid **113** (2004) 125.

4) T. H. Hsueh, H. W. Huang, C. C. Kao, Y. H. Chang, M. C. Ou-Yang, H. C. Kuo, and S. C. Wang: Jpn. J. Appl. Phys. **44** (2005) 2661.

5) S. Y. Chou, P. R. Krauss and P. J. Renstrom: J. Vac. Sci. Technol. B **14** (1996) 4129.

4. GaN Overgrowth on Thermally Etched Nanoporous Templates

4.1 Background

In recent years, the nanostructures have been intensively studied for III-nitride growth. The nanostructures were reported to effectively improve light extraction efficiency as well as crystal quality.[1-6] There are generally two categories considering the use of the nanostructure for nitride growth. One is to use nanostructures as templates for GaN film overgrowth. GaN was grown on such templates until a flat surface was achieved. Then InGaN/GaN MQWs or full LED structure could be grown on the coalesced film.[7,8] The other is to directly grow InGaN/GaN multiple quantum wells on the nanostructures. For the former case, the nanostructure is used for dislocation reduction as well as light extraction efficiency improvement. The latter case makes the full use of properties of the nanostructures. There might be larger light emitting area, and nonpolar and semipolar planes could be realized.[5,9] Therefore the QCSE effect could be suppressed leading to a higher internal quantum efficiency. However, this approach usually results in poor electric properties by introducing a larger serial resistance to the LED device. In this chapter, we report on a novel thermal-etching method for the fabrication of nanoporous templates. The direct growth of MQWs on nanostructures will be discussed in chapter 5 and 6. To fabricate large-scale nanoporous GaN templates, inductively coupled plasma (ICP) dry etching using an anodic aluminum oxide nanohole mask and electrochemical etching methods have been reported.[3,10,11] However, the limited selectivity of ICP dry etching makes deep-hole fabrication quite difficult. Long time dry

etching will introduce damage to the surface of the nanostructures. By electrochemical etching, dense nanoscale voids with very small size could be formed in the GaN template.[10] In these processes, GaN etching is carried out outside the growth chamber. Recently, Yeh et al. reported hydrogen etching of GaN templates in a hydride vapor phase epitaxy (HVPE) reactor for patterned structures.[12] Long nanopores with very small diameters were observed in the experiment. Such in-situ method offers a possibility to integrate the nanostructure fabrication with the growth process. However, the control of pore diameters was not reported. In addition, GaN overgrowth in their report showed little improvement in crystal quality. Until now, thermal etching in an MOVPE reactor for the fabrication of nanoporous structures has not been reported. Thermal etching in an MOVPE chamber for nanostructures is promising because almost all commercial LED wafers are produced by MOVPE. Here, we report on a thermal-etching method for the fabrication of nanoporous templates. This method shows the capability of fabrication very deep nanoporous templates with tunable diameters. This method is also dislocation sensitive, which may make it more effective in dislocation reduction.

4.2 Thermal Etching Process for Fabrication of Nanoporous Templates

To fabricate the nanohole template by thermal etching, the GaN nitride templates with SiO_2 nanohole mask pattern was fabricated by nanoimprint and followed by RIE dry etching. The detailed process was introduced in Chapter 3. Two kinds of GaN templates grown by MOVPE were used for experiments. One had a high dislocation density of 3×10^9 cm^{-2} with a film thickness

of 1 µm. The other had a low dislocation density (4×10^8 cm^{-2}) with a film thickness of 2 µm. After

dry etching, the residual resist was removed by oxygen plasma ashing. Then the templates was

cleaned and loaded to an MOVPE chamber. A pulsed etching process consisting of 60 periods of

pulsed steps was used. The etching process was carried out at 1060 ℃ at a pressure of 130 Torr.

TMG and ammonia were alternately introduced with durations of 5 and 10 s, respectively. There

was a 2 s purge after each pulse. The flow rates were 50 µmol/min for TMGa and 2500 sccm for

NH$_3$ with hydrogen as the carrier gas. The total hydrogen flow rate was 6.5 standard liter per

minute (SLM). The parameters for this thermal etching process is summarized in Table 4.1. The

pulsed gas flow is illustrated in Fig. 4.1.

Table 4.1 Thermal etching condition for nanoporous
GaN template.

TMG (µmol/min)	50 (5s)
NH$_3$ (sccm)	2500 (10 s)
Purge Time	2 s
Pressure (Torr)	130
Temperature (℃)	1060
Period	60
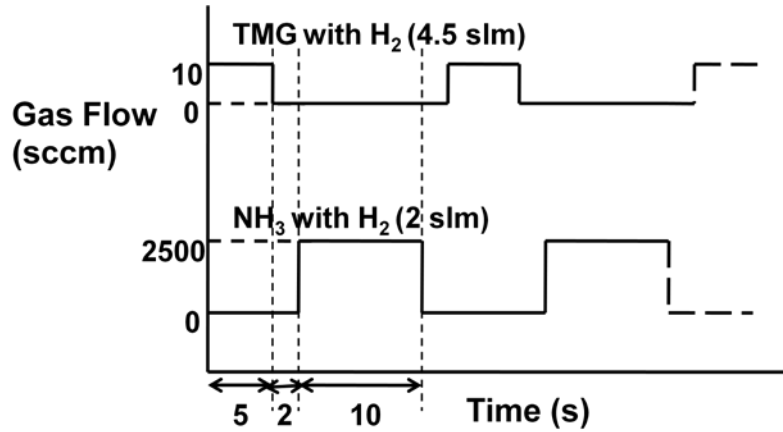
Fig. 4.1 Pulsed gas flow of the thermal etching process.

Actually at the beginning, this pulsed process was intended for nanostructure growth. However,

no GaN growth was observed after this process. In contrast, deep and dense voids were observed

(Fig. 4.2 (a)). Inclined-view and plan-view SEM images of the 2-µm-thick sample after thermal

etching are shown in Figs. 4.2 (a) and 4.2(b), respectively. Yeh et al. reported on the hydrogen

etching of a bare GaN template in an HVPE reactor and formed a nanostructure. However, the

diameter of the etched pores are small, the control of the pore diameter was not reported. Larger

pore diameter would improve the functions of such templates such as light scattering effect and

dislocation reduction effect.
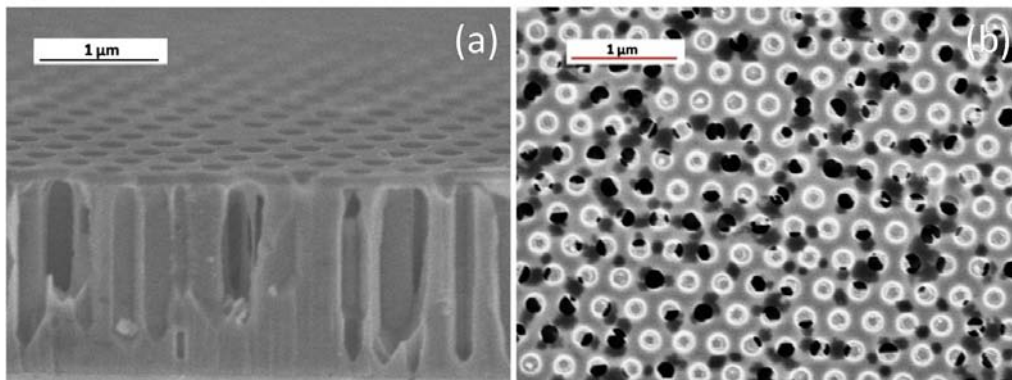
Figs. 4.2 (a) Inclined-view and (b) plan-view SEM images of the 2-µm-thick
sample after thermal etching.

After the thermal etching process, the SiO_2 mask was removed by HF. The plan-view SEM

image of the etched sample after SiO_2 removal is shown in Fig. 4.3.
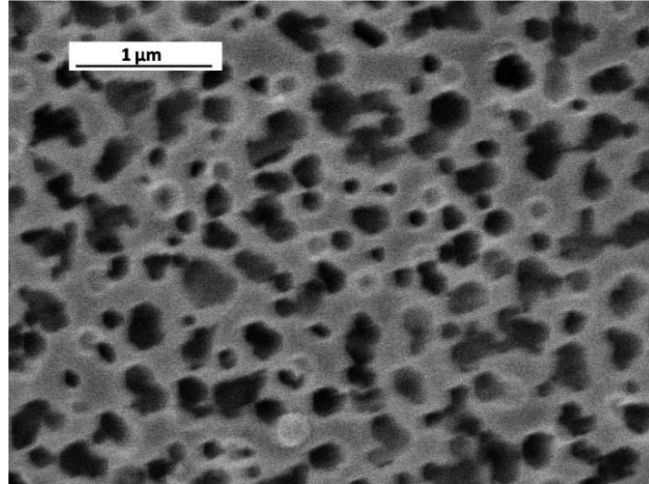
Fig. 4.3. Plan-view SEM image of the etched sample after SiO_2 removal.

The SiO_2 nanohole mask stayed intact during this thermal etching process. Long and dense

voids were formed in the GaN template after etching. Some of the voids were even etched from

the surface down to the sapphire substrate. Under our etching conditions, the etching rate was

rather anisotropic. The etching rate along the c-plane was much higher than that of the sidewall.

Except the merged voids, the lateral diameter of a relatively large void was about 230 nm,

however, the length could be as long as 1400 nm. If we consider the lateral etching depth of one

side wall to be 115 nm, then the etching rate of the c plane was more than 10 times higher than

that of the side wall. The void density was estimated to be approximately 1×10^9 cm^{-2}, whereas the

SiO_2 nanohole density was 5.5×10^8 cm^{-2}. One can see that there were also many etched voids

under the mask, whereas the window area was only partially etched. However, this does not

necessarily mean that the mask cannot protect the underlying GaN template from decomposition.

To demonstrate this, We also used a GaN template without a mask in the same etching process for

comparison. The etched GaN template exhibited a roughened surface throughout the sample

caused by thermal etching (Fig. 4.4). However, no nanoporous structure was observed. Actually,

the thickness of the sample was obviously reduced. We consider that this is because the etching

effect was so strong that the decomposition of GaN occurred everywhere resulting in a low

etching selectivity. Without the protection of SiO_2 mask, due to a larger surface energy of the

nanostructure, the decomposition will be even faster than the planar region. This prevent the

formation of similar nanoporous structure.
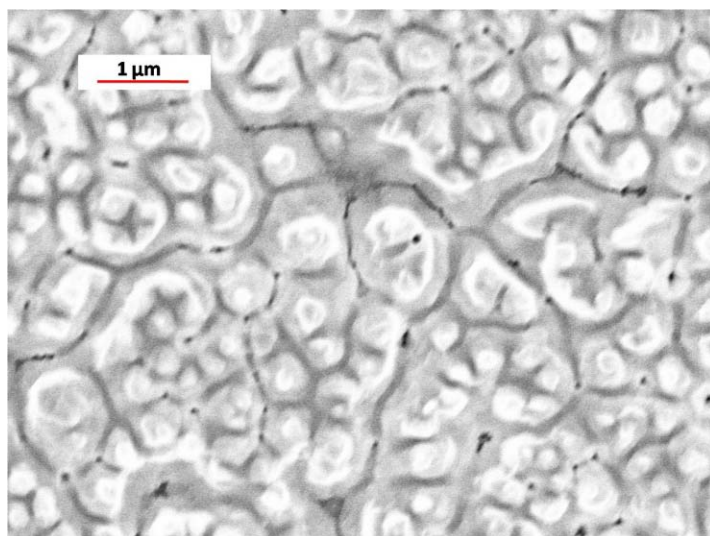
Fig. 4.4 Plan-view SEM image of a planar GaN template without
SiO_2 mask after the same etching process.

We also observed that in some defective areas where the nanohole window failed to develop,

which resulted in a large-area (several micrometers in diameter) continuous SiO_2 mask, the

underlying GaN was completely protected (Fig. 4.5). Therefore, it appears that the nanohole mask

was essential for fabricating nanoporous templates.
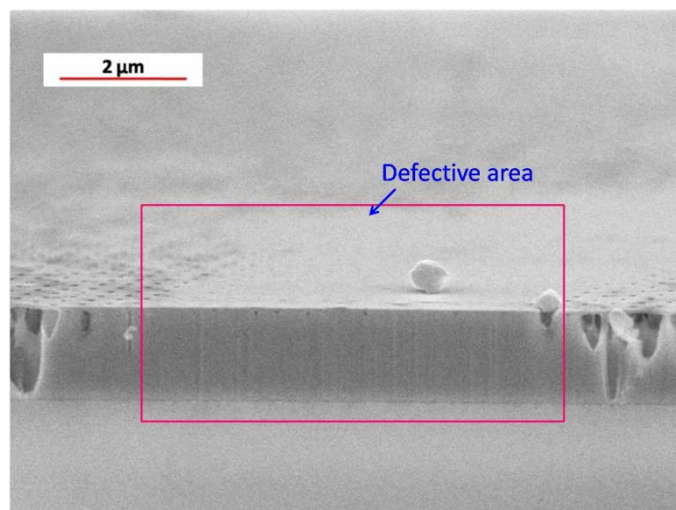
Fig. 4.5 Inclined view SEM image of a defective area where
the nanohole window failed to develop.

The nanoporous structure indicates that the template was selectively etched, and the void

density was on the same order as dislocation density. We suppose that this thermal etching process

might be dislocation-sensitive. Dislocation-sensitive etching has been used for etch pit density

measurement and in-situ etching by SiH_4.[13,14] Besides, dislocation-sensitive dry etching of GaN

film has also been reported. [15] The formation of the nanoporous structure could be explained as

follows. Under the mask, the GaN etching rate was markedly reduced, only spots with a low

bonding energy where dislocations were located tended to decompose. The products of

decomposition could escape through the interface of the GaN template and the SiO_2 mask when

the escaping path was small, one example is the nanohole mask. If the escaping path was too long,

then the products of decomposition could not escape efficiently, the decomposition will be

suppressed, just like where the nanohole mask window failed to develop. In some nanohole window region, if a threading dislocation happened to exist, then it will be easily etched leaving a large nanohole. However, if there happened to be no dislocation, then the GaN would be of high quality and very difficult to decompose. In such window region, deep nanoholes were not formed. Besides, the Ga atoms in the etching products may react with nitrogen atoms in the window region again resulting in the redeposition of GaN. Sometimes this will lead to the formation of nanostructures, which will be shown later. However, when the etching rate was high in the window region, very few nanostructures could emerge from the mask window.

We also investigated the functions of each precursors in this pulsed etching process. Figure 4.6 shows the same pulsed etching process but without the TMG flow. It was found that a similar structure could still be formed without a TMG flow, which means that TMG does not seem to be essential in this process.
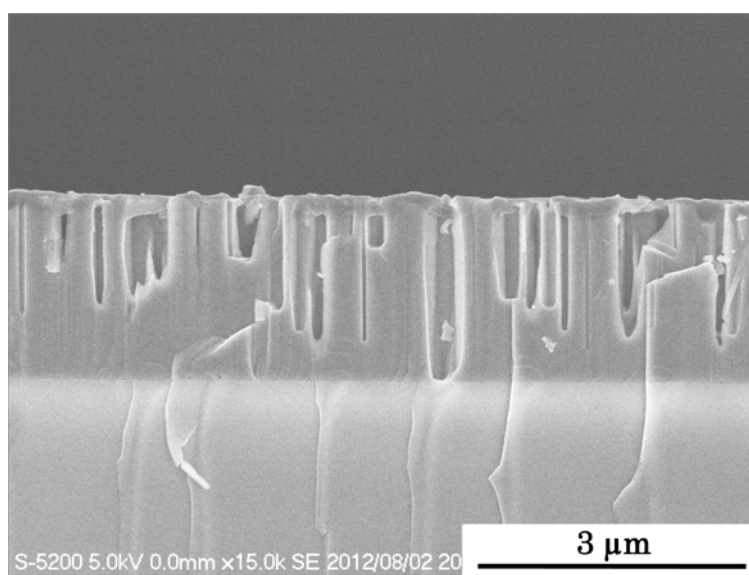
Fig. 4.6 Cross-sectional view SEM image of a GaN template after the thermal etching process without a TMG flow.

However, when the ammonia flow was introduced continuously instead of a pulsed

supply, even without a TMG flow, GaN nanopyramids were spontaneously formed in

every nanohole as well as a few larger islands on the micrometer scale. The SEM

images are shown in Fig. 4.7.
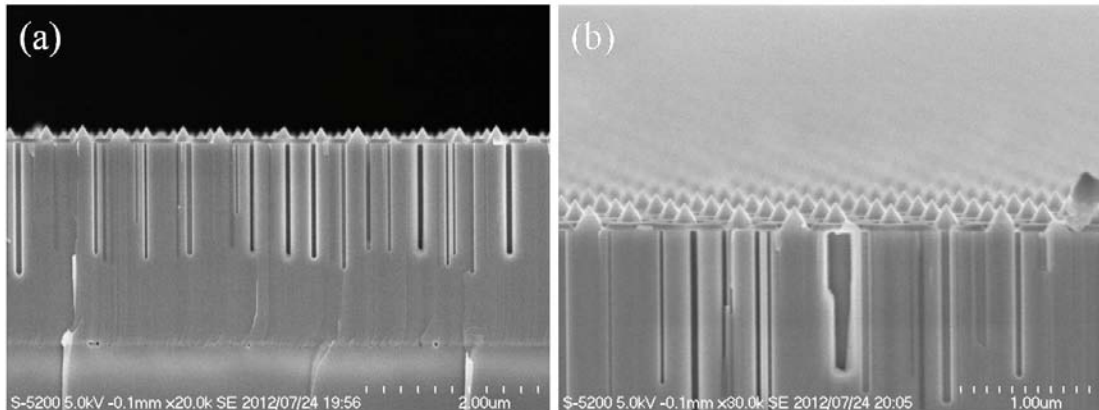
Figs. 4.7 (a) Cross-sectional view and (b) inclined-view SEM images of a GaN
template after the thermal etching with continuous NH$_3$ flow.
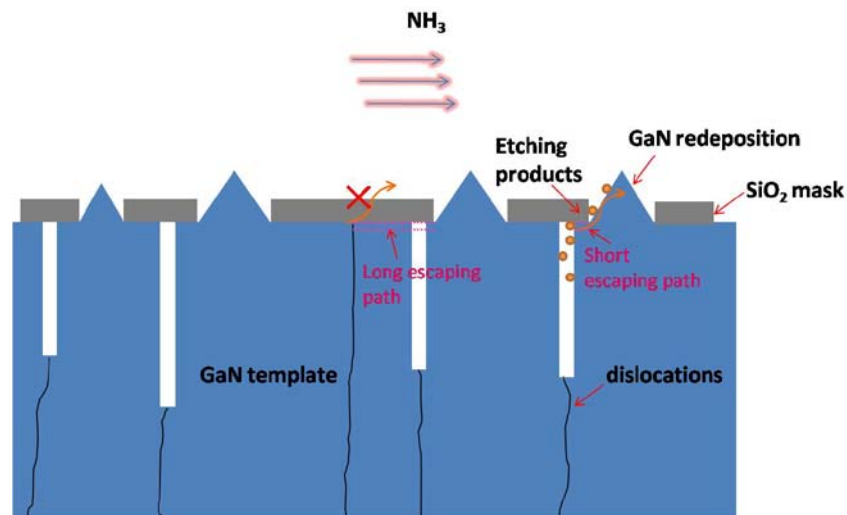
Fig. 4.8 The mechanism of spontaneous formation of GaN nanopyramids by thermal etching.

The formation of nanopyramids might be due to mass transport of etching products

from the voids. As illustrated in Fig. 4.8, when there were defective areas in the SiO$_2$

49

mask, the dislocations beneath the defective SiO_2 mask area might have a long distance to the nearest mask window. The escaping path for the etching products between the SiO_2-GaN interface to the window region was long and the etching process was suppressed. However, for the normally fabricated nanohole mask, the dislocations had a very short escaping path for the etching products, therefore, the etching process could continue. The etching products escaped from the short escaping path and encountered the NH_3 at the mask window region. Due to the reduced etching effect by using a continuous NH_3 flow, GaN redeposition rate became larger than the etching rate at the window region, which was in contrast to the pulsed NH_3 case. This resulted in the formation of GaN pyramids although no TMG flow was introduced. Under continuous NH_3 flow, the diameter of the pores became very small (~20 nm), and extremely large aspect ratio was achieved. The side walls of the pores were very smooth and straight. No such structure was reported in the literature. Comparing the structure with the pulsed etching case, we conclude that the ammonia could very effectively protect the nonpolar side walls and promote anisotropic etching, while the hydrogen will cause isotropic etching, making pores with large diameter.

The etched structure evolution versus etching time was also investigated. The inclined view SEM images of nanohole templates after 6 min, 13 min and 20 min etching were shown in Fig. 4. 9 (a)-(c). When the etching time was 6 min, the etching process had just started, there were small

nanoscale voids emerging from the surface. At some locations voids with larger diameter were observed. This might be because a dislocation happened to exist in a nanohole window. When the etching time increased to 13 min, very dense voids were formed in the whole sample with large length reaching the GaN and sapphire interface. The diameter was also increased. When the etching time further increases to 20 min, the length of the voids stayed the same since it has already reached the sapphire template. However, laterally the diameter of the voids continuously grew and the voids even started to merge and form larger voids. Templates with larger voids were expected to be more effective in dislocation reduction, strain relaxation as well as light extraction efficiency improvement. However, with increasing larger void size, the structure will become more fragile both mechanically and thermally, making it difficult for high temperature regrowth.
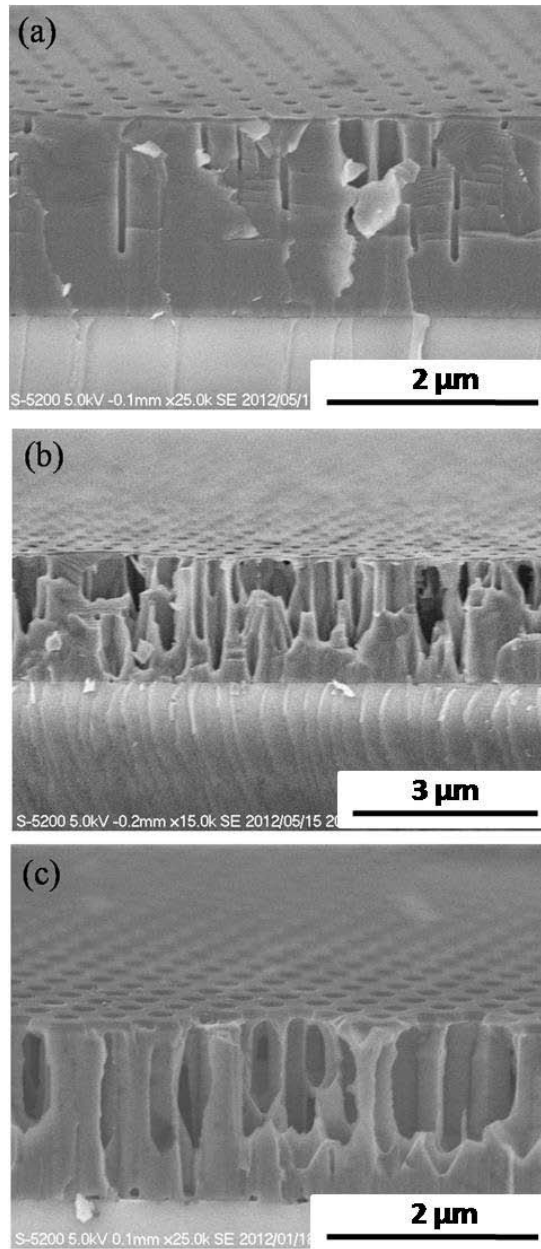
Fig. 4. 9 The inclined view SEM images of the nanohole templates

after (a) 6 min, (b) 13 min and (c) 20 min pulsed thermal etching.

The room temperature PL spectra of the GaN template of high dislocation density and the

fabricated nanoporous structure are shown in Fig. 4.10. The nanoporous GaN exhibited a fivefold

increase in intensity. On the other hand, the peak wavelength showed a 2 nm redshift from 361 to

363 nm. The increased intensity is due to the improved light extraction caused by the scattering

effect of the nanoporous structure and the better coupling of the incident light due to reduced light

reflection at the sample surface. The redshift can be associated with the relaxation of compressive stress.[2,16)]
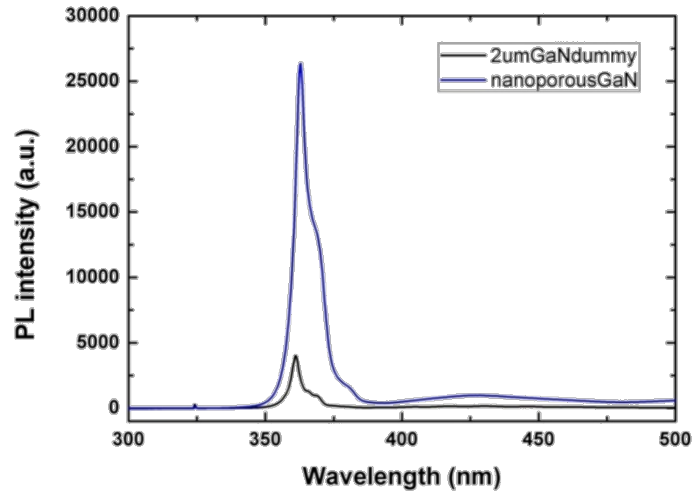
Fig. 4.10 Room temperature PL spectra of the GaN template of high dislocation density and the fabricated nanoporous structure.

To confirm the strain relaxation of the nanohole template, a comparison of the Raman spectra of the nanoporous template and the GaN template was carried out (Fig. 4.11). The peak position of the E_2^{high} mode was shifted from 569.1 to 567.2 cm^{-1}, while the peak position of a strain-free GaN substrate reference was 567.3 cm^{-1}, which indicates a nearly complete strain relaxation of the nanohole sample. The strain relaxation was calculated to be 0.45 GPa using the formula $\Delta\omega = k_{Ra, a}\sigma_a$ in chapter 2.
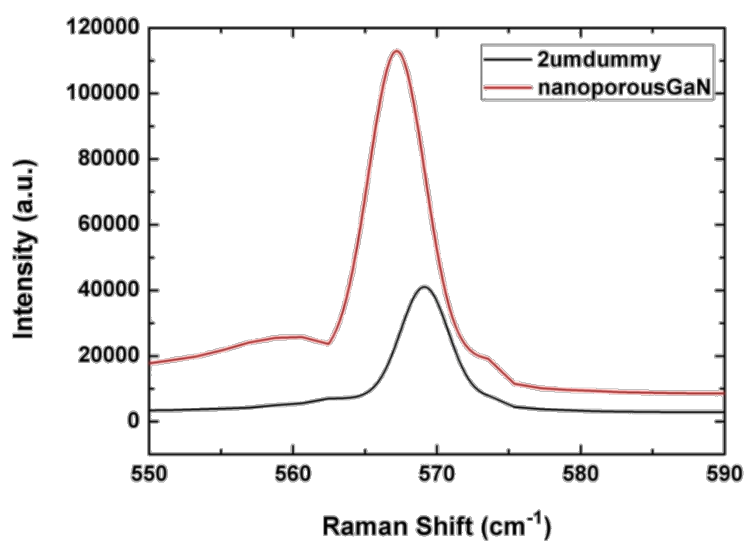
Fig. 4.11   Raman spectra of the nanoporous template and the GaN template.

4.3 GaN Film Overgrowth on Nanoporous Templates

To demonstrate possible applications of such nanoporous templates, GaN films were overgrown on such nanoporous templates. After removing the SiO_2 mask using buffered fluoric acid and sample cleaning, the nanoporous template was used for overgrowth.
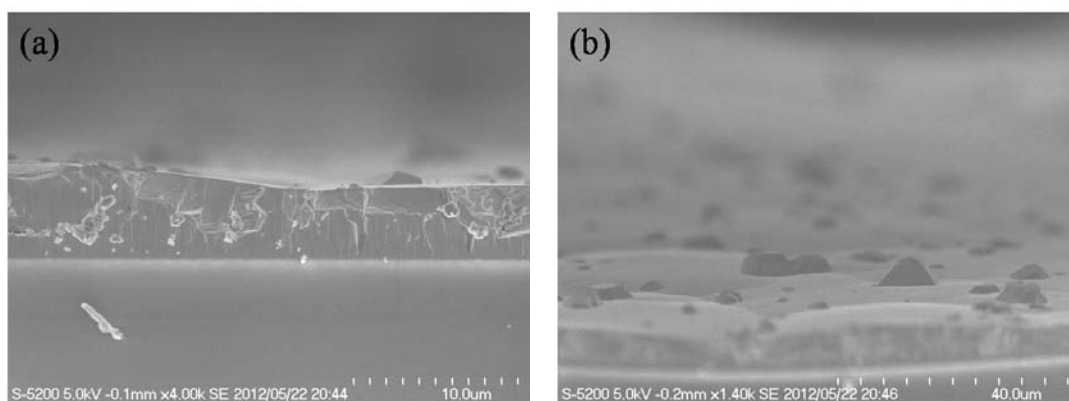
Fig. 4.12 (a) Cross-sectional view and (b) inclined view SEM images of the GaN film overgrown on the nanoporous template at 1090 ^{o}C.

When the growth temperature was set to 1090 ^{o}C under a chamber pressure of 500 torr with a

NH_3 flow rate of 5000 sccm, which was a proper growth condition for high temperature GaN

54

temperature growth, we found that no nanostructures could be observed after growth (Fig. 4.12). The film thickness showed large fluctuations and there were random islands formed on the surface. We believe this was caused by the deformation and decomposition of the nanoporous template during temperature ramping.

To suppress the decomposition of the nanoporous template, we adjusted the growth process and growth condtion. For GaN regrowth on the nanohole template, no intentional thermal cleaning step was used in order to prevent the decomposition. The growth temperature was decreased to 1060 ℃. A chamber pressure of 200 Torr was used, and the NH_3 flow rate was also increased to 7000 sccm leading to a V/III ratio of 4300. The detailed growth condition is listed in Table. 4.2.

Table. 4.2 Condition for GaN overgrowth on nanoporous template.

TMG (sccm)	20
NH3 (sccm)	7000
V/III ratio	4288
Pressure (Torr)	200
Temperature (℃)	1060
Time (min)	90

Large ammonia flow rate and low growth pressure was intended to protect the nanohole template from decomposition at high temperature. Large ammonia flow is a common approach to prevent InGaN decomposition during InGaN well growth. High growth pressure in hydrogen

ambient will enhance the etching effect and promote GaN decomposition.[17] Previously it has been reported by Hiramatsu et al. that large V/III ratio and low growth pressure will promote the GaN lateral growth, while the opposite direction will promote vertical growth rate.[18] Therefore, such growth condition could also promote the lateral growth rate and result in a faster coalescence.

Plan-view and cross-sectional view SEM images of a nanoporous template after temperature ramping was shown in Fig. 4.13(a) and 4.13(b), respectively. It was observed that after temperature ramping there was no strong decomposition and deformation of the nanostructure. However, locally convex shapes formed on the surface. A lot of the voids seemed distributed along their boundaries.
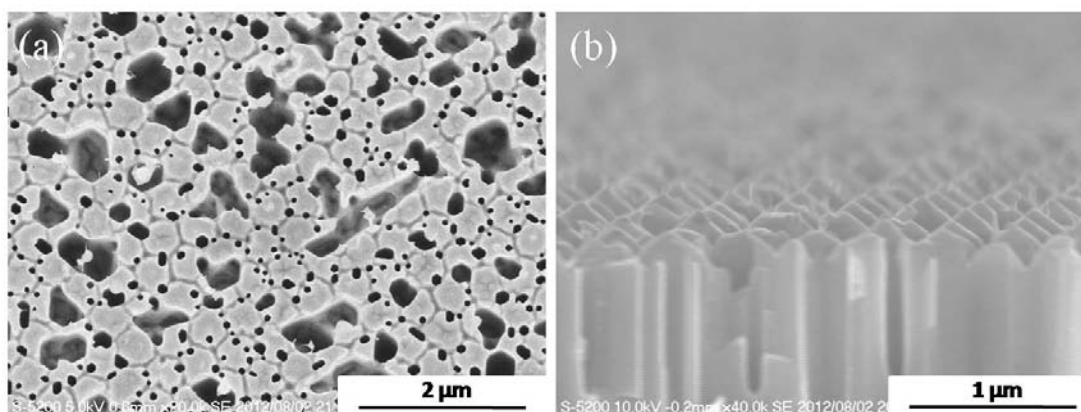
Fig. 4.13 (a) Plan-view and (b) cross-sectional view SEM images of a nanoporous template after temperature ramping.

The SEM images of a nanohole template after 15 min regrowth growth were shown in Fig. 4.14. The growth thickness was around 500 nm. It's found that during the initial growth on the nanohole template, there were no local large islands formed as nuclei. On the contrary, the regrowth was quite uniform across the sample surface. The growth showed a very fast coalescence. A large

portion of the nanoholes disappeared from the surface after growth, while only some nanoholes with small diameter remains. From the cross sectional view, high-density embedded voids with quite large diameters were observed. Some of the voids were as long as 1.5 µm. From the SEM images, we confirmed that the template was well protected from decomposition during the regrowth.
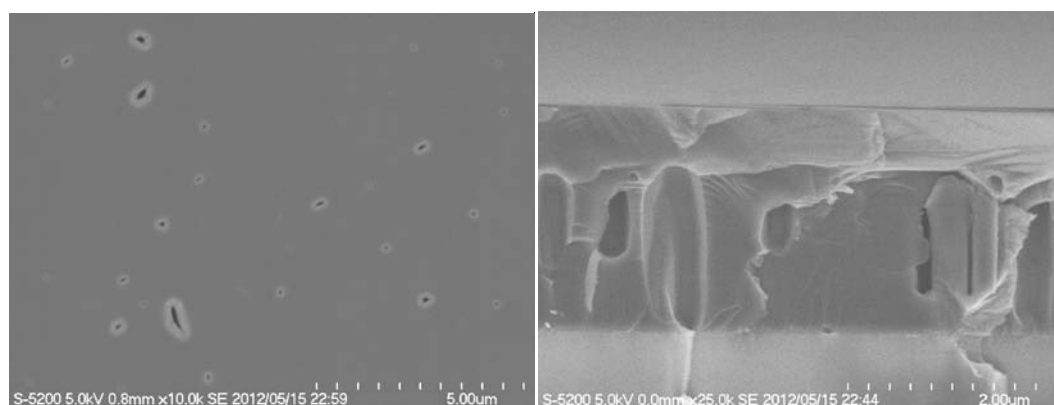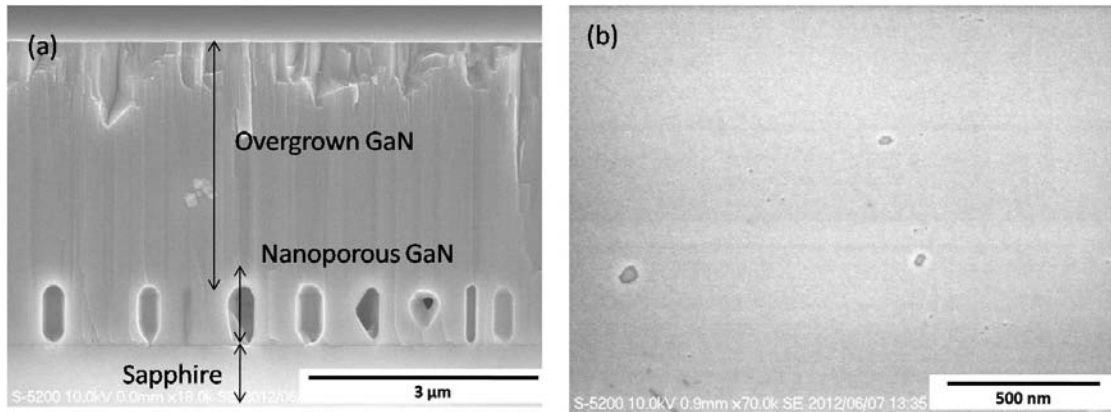

Fig. 4.14 (a) Plan-view and (b) cross-sectional view SEM images of a nanoporous template after 15 min regrowth.

Subsequently, a 3 µm GaN layer was grown using the same growth condition. As is mentioned previously, two kinds of GaN templates were used for experiments. One had a high dislocation density of 3×10^9 cm^{-2} with a film thickness of about 1 µm. The other had a low dislocation density (4×10^8 cm^{-2}) with a film thickness of about 2 µm. For the template with high dislocation density, the cross-sectional and plan-view SEM images of the overgrown sample are shown in Figs 4.15(a) and 4.15(b), respectively. Embedded high-density nanoscale voids could still be observed after the overgrowth, and complete coalescence was achieved after 3 µm growth.

57

Figs 4.15 (a) Cross-sectional and (b) plan-view SEM images of the nanoporous template after 3µm overgrown.
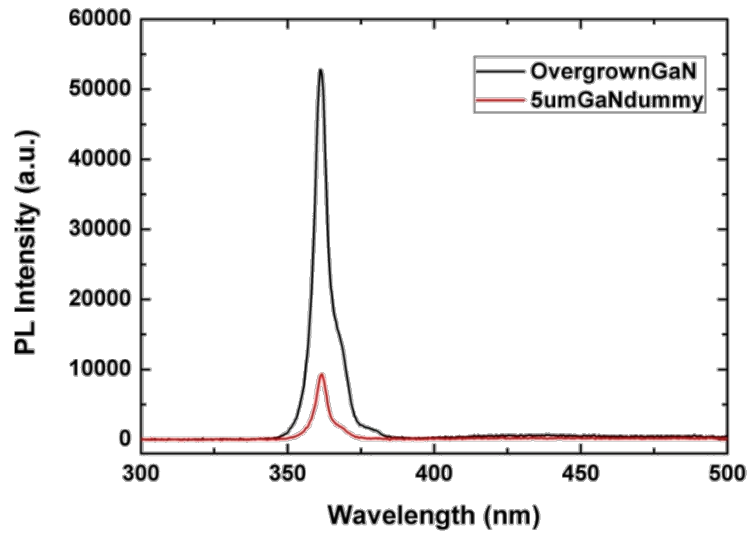
Fig. 4.16 Room temperature PL spectrum of the overgrown GaN film.

The room temperature PL spectrum of the overgrown GaN film is shown in Fig. 4.16. The peak intensity of the PL spectrum showed five-fold increase compared with that of 5 µm dummy, which was grown in parallel. This was attributed to the improvement of the crystal quality which was confirmed by XRD measurement later as well as a great enhance of the light extraction efficiency

by strong scattering effect of the embedded nanoholes. However, in contrast to the nanohole template, the overgrown GaN film showed a slight blue shift (0.7 nm) of the PL peak, which implied a rebuilt compressive strain. The strain state was confirmed by Raman spectra, which is shown in Fig. 4.17. Indeed the strain was rebuilt after overgrowth since the E_2^{high} peak position of the nanoporous sample was almost the same as that of the planar samples. A similar phenomenon was also reported by Tang et al. for GaN overgrowth on a nanocolumn template,[19] which was probably due to the large thermal mismatch between the overgrown GaN layer and the sapphire substrate.
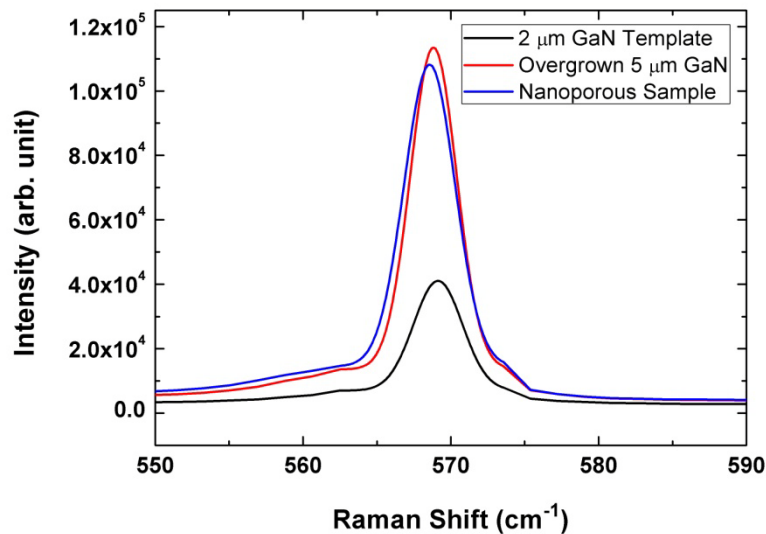
Fig. 4.17 Raman spectra of a 2 µm GaN template, a 5 µm GaN template after overgrowth, and a GaN template overgrown on a nanoporous template.

From X-ray rocking curve (XRC) data shown in Table 4.3, we found that for the sample with a high threading dislocation density of 3×10^9 cm^{-2}, the crystal quality was greatly improved by overgrowth. The XRC full widths at half maximum

(FWHMs) for the (002) and (102) planes were reduced from 326 and 882 arcsec to 203

and 464 arcsec, respectively. The dislocation density was reduced to about 4×10^8 cm^{-2}

as determined by panchromatic CL measurement.

Table 4.3   XRC FWHMs of (002) and (102) planes for the 2 µm GaN template, overgrown 5 µm GaN and the nanoporous sample.

Sample	002 (arcsec)	102 (arcsec)
2 µm GaN template	326	882
Overgrown 5 µm GaN	245	839
GaN on nanoporous template	203	464

(a)
5 µm GaN dummy: RMS 0.23 nm

(b)
Overgrown GaN: RMS 0.16 nm
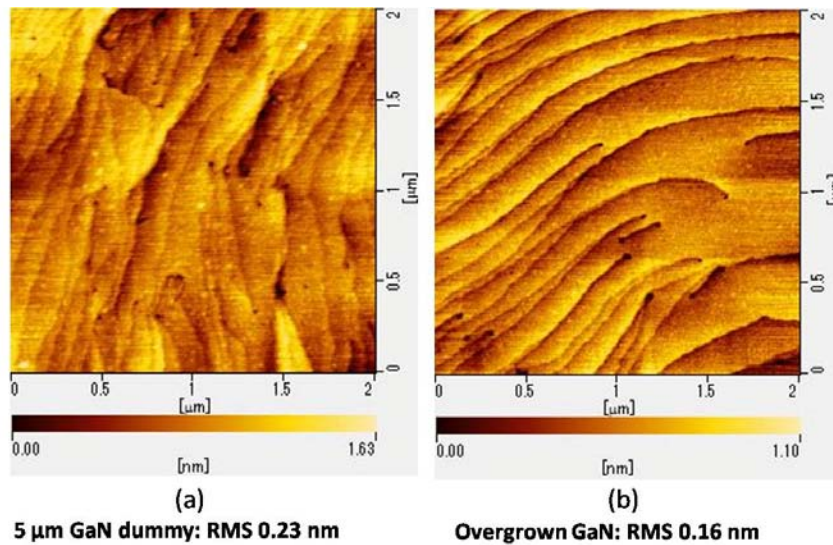
Fig. 4.18 2×2 µm AFM scan of the overgrown 5 µm GaN and the nanoporous sample.

The surface morphology was measured by AFM (Fig. 4.18). The overgrown GaN showed

obviously improved surface flatness. The 2×2 µm root mean square (RMS) value was reduced

from 0.23 nm to 0.16 nm, and the atomic steps was quite clear.

60

To confirm the dislocation reduction effect for GaN templates with high dislocation density, the thermal etching and GaN overgrowth was also performed using MOVPE with a showerhead configuration.

GaN templates grown under the showerhead configuration generally have a larger dislocation density than the GaN templates grown by side-flow configuration. A larger TMG flow rate and higher growth temperature were used. The GaN template growth condition is listed in Table 4.4. The XRC FWHM of the (002) plane was 486 arcsec, and the (102) FWHM was too weak to be determined.

Table 4.4 Typical growth condition for GaN template on sapphire substrate with the showerhead configuration.

	LT buffer	HT GaN
TMG (sccm)	12	30
NH3 (sccm)	5000	5000
V/III ratio	3640	1456
Pressure (Torr)	200	200
Temperature (℃)	550	1100
Time (min)	3	60

The thermal etching condition is listed in Table 4.5. A similar pulsed thermal etching process without TMG flow was used. Similar structure could also be easily realized, suggesting the thermal etching method is suitable for different equipments. The fabricated nanoporous template is shown in Fig. 4.19.

Table 4.5 Thermal etching condition for nanoporous
GaN template using a showerhead configuration.

TMG (μmol/min)	0 (5s)
NH3 (sccm)	1500 (10 s)
Purge	2 s
Pressure (Torr)	100
Temperature (°C)	1150
Period	60
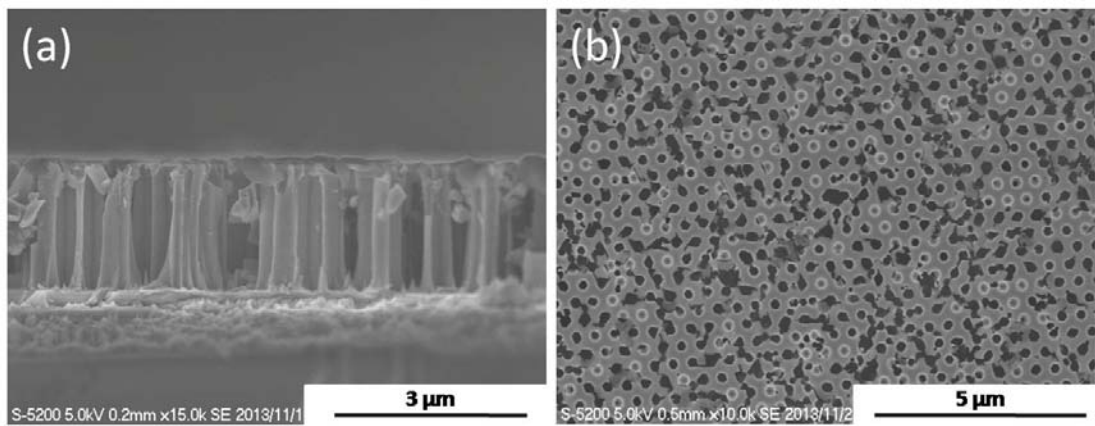
Fig. 4.19 (a) Cross-sectional and (b) plan-view SEM images of the nanoporous
template after thermal etching with a showerhead configuration.

For GaN overgrowth, another growth process was attempted. First, the GaN growth was

initiated at 950 ^{o}C for 10 min without intentional thermal cleaning step. The lower growth

temperature was intended for a better protection of the nanohole template from decomposition.

Then the growth temperature was further ramped to 1100 ^{o}C, which was the optimal growth

temperature for high temperature GaN. The growth time was 60 min with a thickness of about 1.8

um. During the regrowth, a planar sample was also grown in parallel for comparison. The XRC

FWHMs of the (002) and (102) planes of the overgrown nanohole sample were measured to be

428 and 728 arcsec, respectively, much smaller than the values 481 and 924 arcsec of the planar

sample. Another sample grown on a nanoporous template with the initial growth at 950 $^{\circ}$C for 20

min showed even lower XRC FWHMs of 383 and 613 arcsec for the (002) and (102) planes. The

XRD results are summarized in Table 4.6. The plan-view and cross-sectional view SEM images of

the nanoporous template after overgrowth (950 $^{\circ}$C 20 min) are shown in Fig. 4.20. Full

coalescence and flat surface was achieved after the overgrowth. In the cross-sectional view image,

very dense embedded voids as long as 1.8 µm were observed. The heights of the voids were quite

uniform which implied little decomposition or deformation of the nanoporous template during the

regrowth process.

Table 4.6 XRC FWHMs of (002) and (102) planes for the samples grown
with a showerhead configuration.

Sample	002 (arcsec)	102 (arcsec)
2 µm GaN template	486	–
Overgrown planar sample (950 °C 10 min)	481	924
Nanoporous template (950 °C 10 min)	428	728
Nanoporous template (950 °C 20 min)	383	613
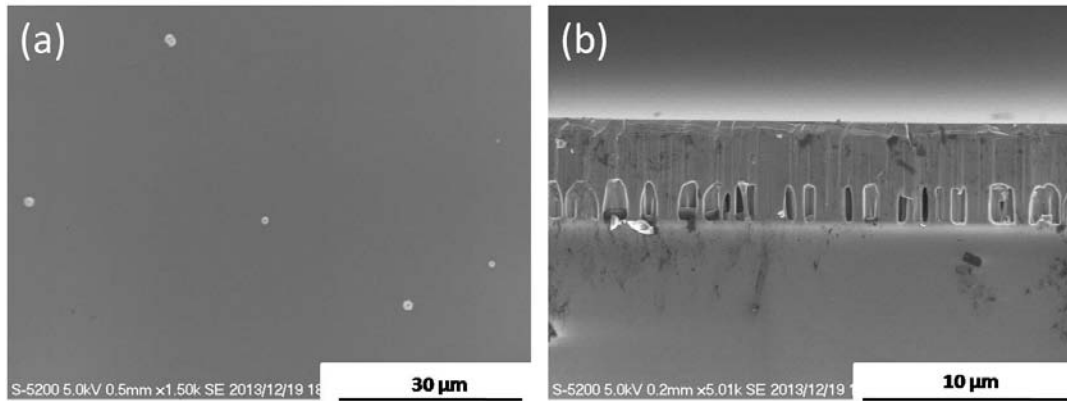
Fig. 4.20 (a) Plan-view and (b) cross-sectional view SEM images of the nanoporous template after overgrowth (950 $^\circ$C, 20 min).

However, for GaN templates with a higher quality (TDD, 4×10^8 cm^{-2}), little improvement could be observed. The TDD was still about 4×10^8 cm^{-2} after overgrowth as shown in Table 4.7.

Table 4.7   XRC FWHMs of (002) and (102) planes for overgrown 5 µm GaN and the nanoporous sample using the high quality GaN template.

Sample	002 (arcsec)	102 (arcsec)
Overgrown 5 µm GaN	237	379
GaN on nanoporous template	259	357

The PL intensity of the sample grown on a nanoporous template fabricated from low-dislocation density GaN template showed a two-fold increase compared to the 5 µm planar control sample (Fig. 4.21). This enhancement is not as strong as the template with higher dislocation density. This increase in PL intensity is mainly attributed to the strong scattering effect of the embedded nanoscale voids while the contribution from crystal quality improvement is trivial. One possible explanation is because the coalescence introduced dislocation density is on the same

64

order of that of the template. The dislocation densities of 4×10^8 cm^{-2} were determined

by counting the dark spots in cathodeluminescence images and may be

underestimated owing to the limited resolution of the images.
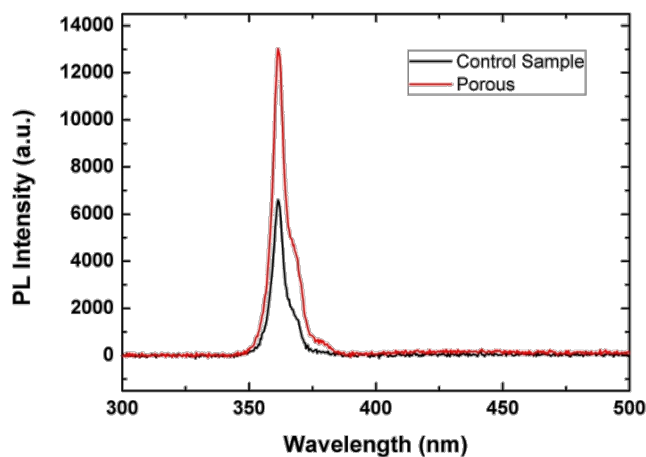
Fig. 4.21 PL spectra of overgrown 5 µm GaN and the nanoporous
sample using the high quality GaN template.

4.4 Properties of InGaN/GaN MQWs Grown on Nanoporous Templates

To assess the effect of such a structure on LED performance, following the GaN overgrowth

(side flow), three-period $In_{0.1}Ga_{0.9}N$/GaN multiple quantum wells (MQWs) were deposited on the

coalesced GaN film. For comparison of the properties of the MQWs, high quality GaN templates

were used. The crystal quality was unchanged after overgrowth according to the XRC results in

Table 4.4. The plan-view and cross-sectional view SEM images of MQWs grown on the

nanoporous template were shown in Fig. 4.22. From the cross-sectional view, we confirmed

high-density nanoscale voids after regrowth. The same structure was also grown on a planar GaN

template sample for comparison. The growth condition of the MQWs was listed in Table 4.8.

InGaN well and the GaN barrier had thicknesses of 4.5 and 15 nm, respectively. The thickness of

the GaN cap layer was 30 nm.
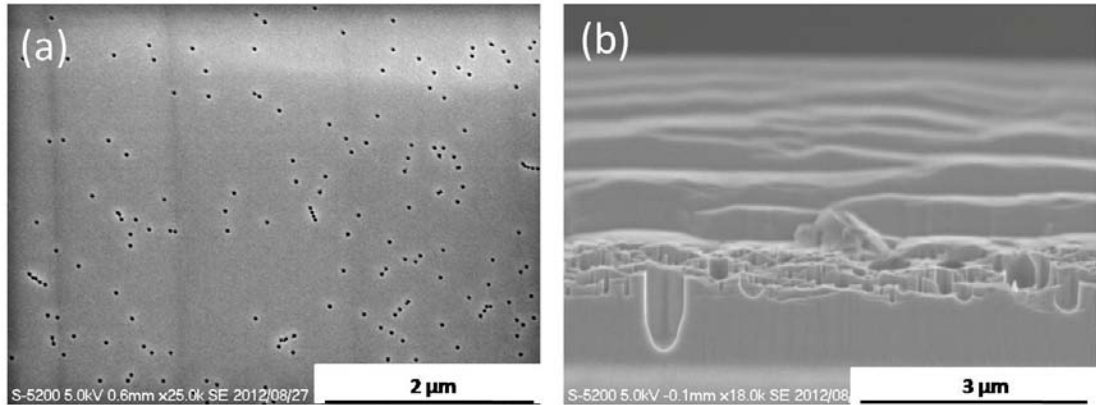
Fig. 4.22 (a) Plan-view and (b) cross-sectional view SEM images of MQWs grown
on the nanoporous template

Table 4.8 Growth condition of the InGaN/GaN MQWs.

	GaN barrier	InGaN well	GaN cap
TEG (μmol/min)	15.56	15.56	15.56
TMI (μmol/min)		10.38	
TMI/(TMG+TMI)		0.4	
NH$_3$ (SLM)	8	8	8
Carrier Gas	N$_2$	N$_2$	N$_2$
Growth Temp. (℃)	760	760	760
Pressure (torr)	500	500	500
Process Time (min)	6	1	12

The plan-view SEM image of a planar sample without the nanoporous structure was shown in

Fig. 4.23. Comparing the two plan-view images, it was found that the pit density of the MQWs,

which is usually related to the dislocation densities of the underlying GaN, were almost the same.

This is in agreement with the conclusion that the crystal quality stayed almost the same after

overgrowth.

66
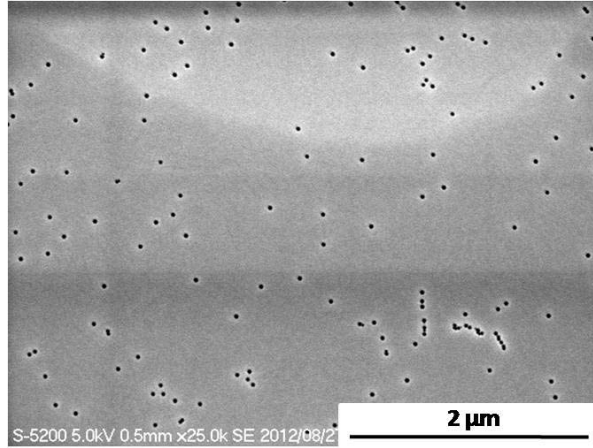
Fig. 4.23 Plan-view SEM image of MQWs grown on a planar sample.
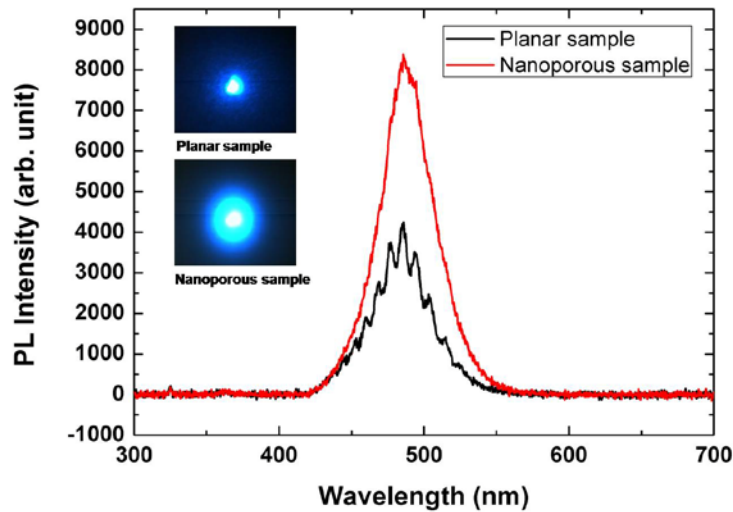
Fig. 4.24 PL spectra of the MQWs on the nanoporous GaN template and a planar template.

The PL spectrum of the MQWs on the nanoporous template in Fig. 4.24 showed the same peak

position as that of the control sample, but the intensity showed a 100% increase. It was believed

that this enhancement of PL intensity was mainly due to the increased light extraction efficiency

caused by the scattering effect of the underlying nanoporous structure. The two insets show

different PL patterns, both of which are in focus and were recorded by a CCD camera. The

enlarged emitting area confirms the scattering effect of the nanoporous template.

67

4.5 Summary

In this chapter, we reported a new thermal etching method in an MOVPE reactor for the fabrication of nanoporous templates. The nanoporous template showed dense voids with a density of approximately 1×10^9 cm^{-2}. The thermal etching process was quite anisotropic. The etching rate of the c-plane could be more than 10 times higher than that of the side wall. The nanohole SiO$_2$ mask was found to be essential in this process. If there was no SiO$_2$ mask on the GaN template or if there was no nanohole windows on the SiO$_2$ mask, the nanoporous structure could not be formed. Compared to the pulsed etching process, the nanoholes fabricated with continuous NH$_3$ flow showed much smaller lateral diameter and the side wall of the voids became very smooth, implying that NH$_3$ could effectively protect the side wall while the hydrogen carrier gas promoted the isotropic etching. When continuous NH$_3$ flow was introduced, nanopyramids were spontaneously formed in every mask window even without introducing a TMG flow. The formation of nanopyramids was explained by the mass transport process. The fabricated nanoporous template showed almost full strain relaxation and a five-fold increase in PL intensity compared with a planar GaN template. By adjusting the regrowth parameters, we suppressed the decomposition and deformation of the nanoporous templates during GaN regrowth. GaN films overgrown on the nanoporous templates fabricated from GaN templates with high dislocation density showed a five-fold increase in PL intensity. Besides, the crystal quality as well as surface flatness were also obviously improved. For nanoporous templates fabricated from high quality GaN template, however, the crystal quality was not obviously improved, the twofold increase in

PL intensity compared with the planar template was mainly attributed to the improved LEE. The

dislocation reduction and embedded void formation were also confirmed by using a showerhead

configuration. InGaN/GaN MQWs grown on the nanoporous templates that fabricated from high

quality GaN templates showed a twofold increase in PL intensity, which was also mainly

attributed to the improved LEE.

References

1) C. H. Chan, C. H. Hou, S. Z. Tseng, T. J. Chen, H. T. Chien, F. L. Hsiao, C. C. Lee, Y. L. Tsai, and C. C. Chen: Appl. Phys. Lett. **95** (2009) 011110.

2) J. H. Lee, J. T. Oh, Y. C. Kim, and J. H. Lee: IEEE Photonics Technol. Lett. **20** (2008) 1563.

3) K. Y. Zang, Y. D. Wang, H. F. Liu, and S. J. Chua: Appl. Phys. Lett. **89** (2006)

4) C. H. Chiu, P. M. Tu, C. C. Lin, D. W. Lin, Z. Y. Li, K. L. Chuang, J. R. Chang, T. C. Lu, H. W. Zan, C. Y. Chen, H. C. Kuo, S. C. Wang, and C. Y. Chang: IEEE J. Sel. Top. Quantum Electron. **17** (2011) 971.

5) Y. J. Hong, C. H. Lee, A. Yoon, M. Kim, H. K. Seong, H. J. Chung, C. Sone, Y. J. Park, and G. C. Yi: Adv. Mater. **23** (2011) 3284.

6) Y. K. Su, J. J. Chen, C. L. Lin, S. M. Chen, W. L. Li, and C. C. Kao: Jpn. J. Appl. Phys. **47** (2008) 6706.

7) T. Y. Tang, C. H. Lin, Y. S. Chen, W. Y. Shiao, W. M. Chang, C. H. Liao, K. C. Shen, C. C. Yang, M. C. Hsu, J. H. Yeh, and T. C. Hsu: IEEE Electron Device Lett. **57** (2010) 71.

8) C. H. Kuo, L. C. Chang, C. W. Kuo, and G. C. Chi: IEEE Photonics Technol. Lett. **22** (2010) 257.

9) S. P. Chang, Y. C. Chen, J. K. Huang, Y. J. Cheng, J. R. Chang, K. P. Sou, Y. T. Kang, H. C. Yang, T. C. Hsu, H. C. Kuo, and C. Y. Chang: Appl. Phys. Lett. **100** (2012) 061106.

10) C. B. Soh, H. Hartono, S. Y. Chow, S. J. Chua, and E. A. Fitzgerald: Appl. Phys. Lett. **90** (2007) 053112.

11) D. J. Diaz, T. L. Williamson, I. Adesida, P. W. Bohn, and R. J. Molnar: J. Appl. Phys. **94** (2003) 7526.

12) Y. H. Yeh, K. M. Chen, Y. H. Wu, Y. C. Hsu, T. Y. Yu, and W. I. Lee: J. Cryst. Growth **333** (2011) 16.

13) M. H. Lo, P. M. Tu, C. H. Wang, Y. J. Cheng, C. W. Hung, S. C. Hsu, H. C. Kuo, H. W. Zan, S. C. Wang, C. Y. Chang, and C. M. Liu: Appl. Phys. Lett. **95** (2009) 211103.

14) D. S. Wuu, W. K. Wang, K. S. Wen, S. C. Huang, S. H. Lin, S. Y. Huang, C. F. Lin, and R. H. Horng: Appl. Phys. Lett. **89** (2006) 161105.

15) P. Frajtag, J. P. Samberg, N. A. El-Masry, N. Nepal, S. M. Bedair: J. Cryst. Growth **322** (2011) 27.

16) A. Najar, M. Gerland and M. Jouiad: J. Appl. Phys. **111** (2012) 093513.

17) D. D. Koleske, A. E. Wickenden, R. L. Henry, J. C. Culbertson, and M. E. Twigg: J. Cryst. Growth **223** (2001) 466.

18) K. Hiramatsu, K. Nishiyama, A. Motogaito, H. Miyake, Y. Iyechika, and T. Maeda: Phys. Status Solidi A. **176** (1999) 535.

19) T. Y. Tang, W. Y. Shiao, C. H. Lin, K. C. Shen, J. J. Huang, S. Y. Ting, T. C. Liu, C. C. Yang, C. L. Yao, J. H. Yeh, T. C. Hsu, W. C. Chen, H. C. Hsu, and L. C. Chen: J. Appl. Phys. **105** (2009) 023501.

5. InGaN/GaN Multi-quatum Wells Grown on GaN Nanopyramids

5.1 Background and Motivation

In chapter 4, we discussed using nanoporous GaN template for GaN overgrowth. In this chapter, we focus on directly growing InGaN/GaN multiple quantum wells on the nanostructure. This makes the full use of properties of the nanostructures. One fundamental issue that limit the efficiency of nitride-based LED is the strong piezoelectric polarization induced QCSE.[1-3] Nonpolar or semipolar planes have been reported to eliminate or greatly reduce the QCSE in the quantum wells.[4-6] While nonpolar and semipolar GaN substrates that sliced from GaN bulk usually have very limited size and are quite expensive, semipolar planes and nonpolar planes were often observed when growing nanostructures.[7-10] Besides, LEDs grown on the nanostructures usually have larger light emitting area compared with the conventional planar LEDs. Strain relaxation effect and improved light extraction efficiency have also been reported for these nanostructures.[11-13]

Despite of these advantages, high-efficiency LEDs based on the nanostructures are still difficult to realize. Nanorod and nanopyramid structures have been successfully grown by selective area growth (SAG) by many groups. However, the coalescence and planarization of p-GaN surface, which is usually required for standard LED fabrication process, requires a thick p-GaN layer.[8,14] This substantially increases the resistance of LED device. In particular, for nanopyramid structure, the so-called "self-limiting" phenomenon was reported.[15,16] After GaN nanopyramid formation in the mask window region, the pyramids will stop growing and remain

the size restricted by mask window. Moreover, non-uniform growth with large islands formation have also been observed.[17] These phenomena make the surface planarization quite difficult.

Compared with a planar structure, a much thicker p-GaN layer is required for an LED grown on a nanopyramid structure.
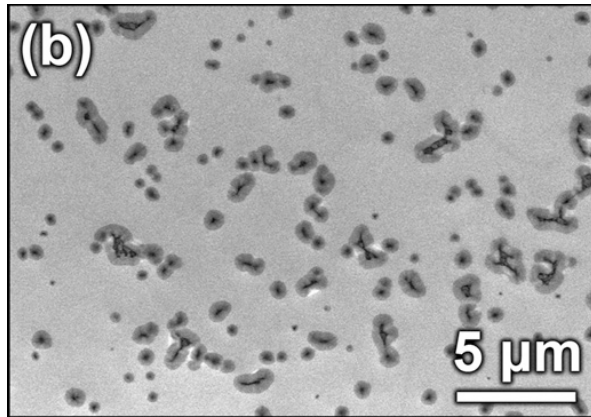

Fig. 5.1 Partially coalesced p-GaN after 30 min growth on a GaN nanopyramid template.[14]

To achieve a flat surface by a thin p-GaN layer, reducing the spacing between pyramids by uniformly increasing the pyramid size is desirable. Besides a faster coalescence, such structure has an even larger light emitting area and the crystal quality may also been improved by lateral overgrowth. The concept is shown schematically in Fig. 5.2.
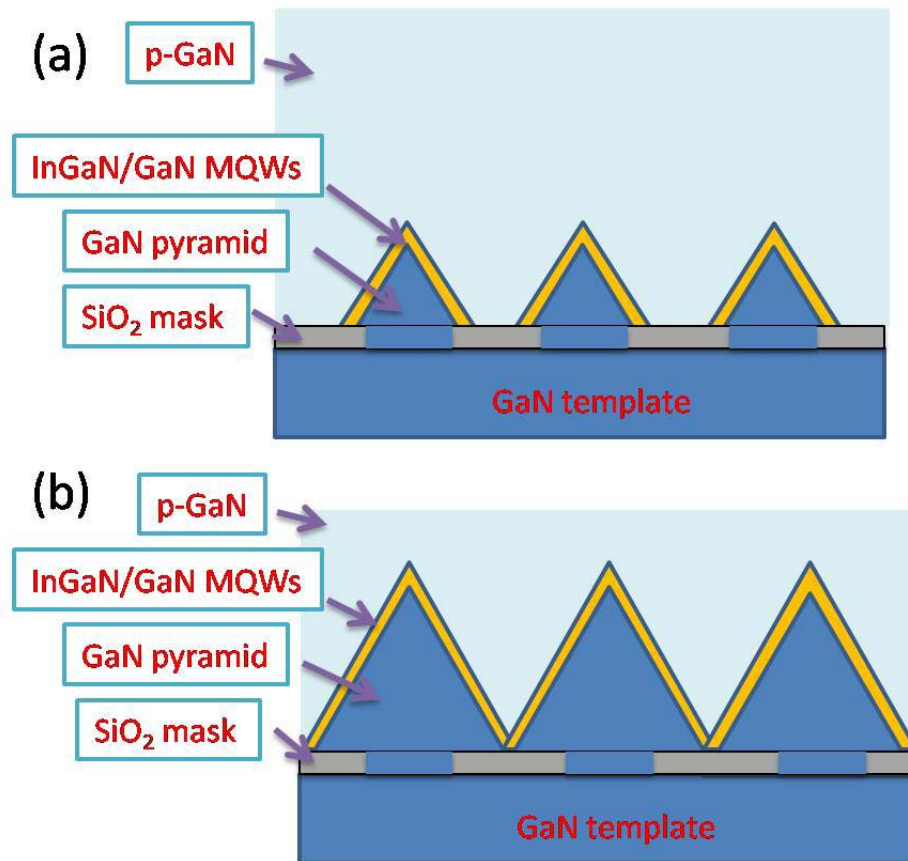
Fig. 5.2 (a) Conventional GaN nanopyramid based LED structure; (b) GaN Nanopyramid based LED structure proposed in this work.

In this research, the size of nanopyramids was successfully controlled by using relatively low growth temperature and nitrogen as carrier gas. MQW structure was subsequently grown on the nanopyramids. The structural and optical properties of such structure were investigated.

5.2 Growth of GaN Nanopyramids

The GaN templates with SiO_2 nanohole mask pattern was fabricated by nanoimprint and followed by RIE dry etching. The detailed process is introduced in Chapter 3. The residual resist was removed by oxygen plasma ashing. After cleaning, the template was loaded into an MOVPE

74

chamber for nanopyramid growth.

When the nanopyramids were grown under high temperature typically between 950~1100 ℃, which was the growth temperature used in almost all the researches in the literature, the so-called "self-limited growth" was dominant in the growth.[15,16] As an example, Figure 5.3 shows an inclined-view SEM image of GaN regrowth on a SiO_2-nanohole-patterned GaN template. The growth was performed at 1060 ^{o}C for 8 min. The flow rates of TMG and NH_3 were 103 umol/min and 5 SLM, respectively. The nominal growth rate on a planar template was 33 nm/min. Hydrogen was used as the carrier gas. We observed a lot of randomly distributed large islands in micro scale, which we called abnormal growth. Meanwhile, there were also a lot of small nanopyramids emerged from the nanohole mask window. The growth of pyramids was not uniform.
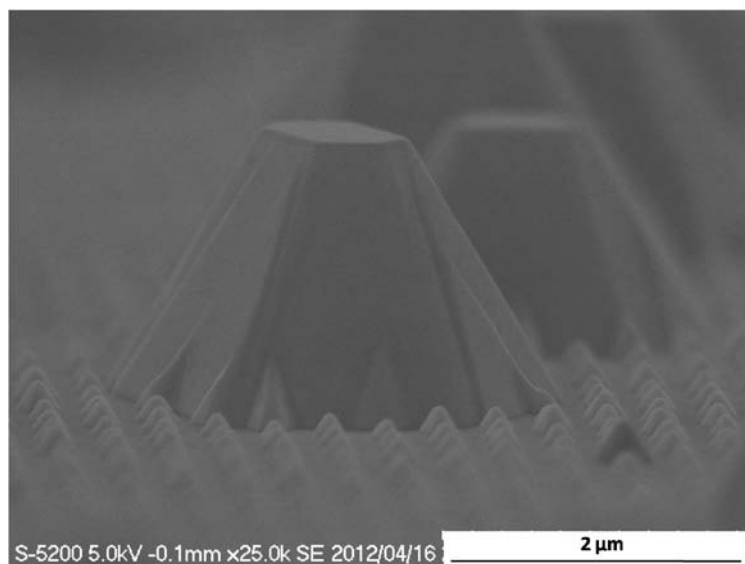
S-5200 5.0kV -0.1mm ×25.0k SE 2012/04/16   2 μm

Figure 5.3 shows an inclined-view SEM image of GaN regrowth
on a SiO_2-nanohole-patterned GaN template.

Growth conditions were also investigated using sapphire substrate with SiO_2 nanohole mask. As an example, Fig. 5.4 shows a plan-view SEM image of GaN regrowth at 950 ^{o}C for 15 min. The

growth was initiated by a low temperature nucleation layer using condition for the growth of

planar GaN templates. It was observed that even when grown under a lower temperature of 950 $^{\circ}$C,

the pyramid growth was still not uniform. Abnormal large islands formed while a lot of

nanopyramids stayed the size restricted by the mask window.
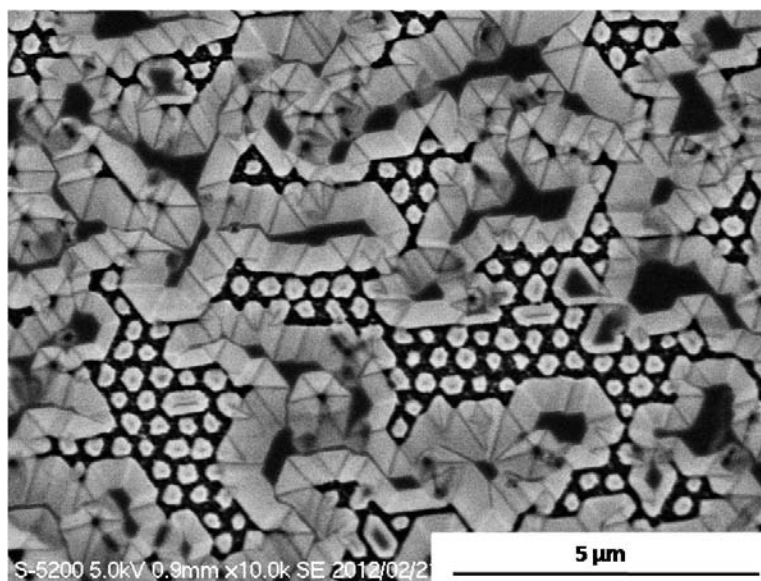
Fig. 5.4 plan-view SEM image of GaN regrowth on a sapphire substrate
with SiO$_2$ nanohole mask.

Because the number of dangling bonds of the semipolar {1-101} planes are small, these planes

are very stable during growth.[18,19] In particular, when growing nanopyramids by SAG, the very

small surface area of the nanopyramids results in very few atomic steps to accommodate adatoms.

Therefore, the adatoms have a large diffusion length and a very short dwell time on these

nanoscale planes. Once the nanopyramids with six {1-101} planes were formed, the growth would

stop and such structure remained very stable under a large range of growth conditions.[15]

To suppress the abnormal large islands as well as overcome the "self limiting growth", we tried

special growth conditions: the growth condition used for the GaN barrier of the InGaN/GaN

MQWs. This was based on the observation that when growing InGaN/GaN MQWs on nanopyramids, the MQWs seemed uniformly grown on the nanopyramids. Nitrogen was used as carrier gas instead of hydrogen, and the growth temperature was decreased, which reduced the diffusion length as well as desorption rate of the adatoms.

For nanopyramid growth, TEG, TMI, and ammonia were used as precursors. Nitrogen was used as the carrier gas. After thermal cleaning at 950 ℃ for 5 min, first, GaN pyramid was grown at 800 ℃ for 60 min. The flow rates of TEG and ammonia was kept at 15.56 µmol/min and 8 SLM, respectively. The growth pressure was kept at 500 torr. A plan-view SEM image of the sample after regrowth is shown in Fig 5.5.
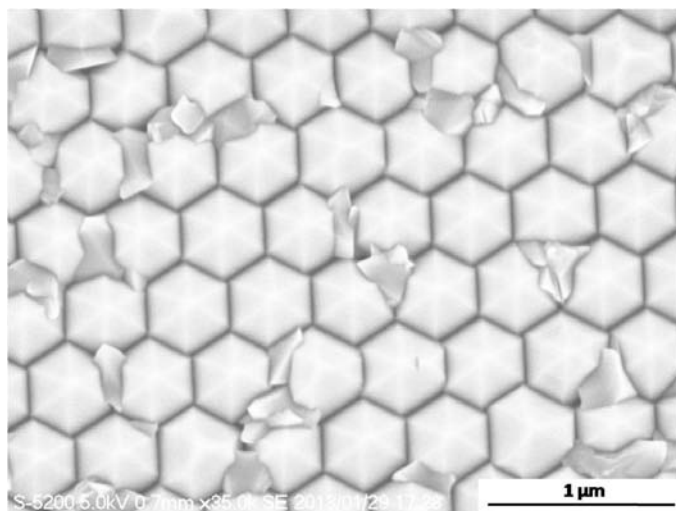
Fig 5.5 GaN pyramid was grown on a SiO_2 nanohole patterned
GaN template at 800 ℃ in a N_2 ambient.

Nanopyramids were observed in every nanohole mask windows. The size of the pyramid was no longer restricted by the mask window but obviously larger than the window size. The size of the pyramids became so large that the pyramids already contacted with each other and completely

77

covered the SiO$_2$ mask. Therefore, this growth condition indeed could be used to overcome the self-limiting growth. The pyramid size could be tuned by growth parameters. Moreover, throughout the whole sample, no abnormal large islands were observed, which means under such growth condition the pyramid growth was very uniform. However, we found many randomly grown GaN particles between the pyramids.

In order to suppress the random growth, two approaches were attempted. One was to introduce a small amount of hydrogen during the growth. Figure 5.6 shows the plan-view SEM image of the sample grown with 100 sccm hydrogen flow into the growth chamber. In the image we could see that the random growth was successfully suppressed. The pyramids showed quite uniform size which was obviously larger than the mask window. However, we observe that some pyramids showed not smooth surface. There seemed to be "steps" on the surface. The formation mechanism of these steps was still not clear. We suppose it was probably related to the etching effect of the hydrogen, which makes the dwell of the adatoms on the pyramid surface not uniform.
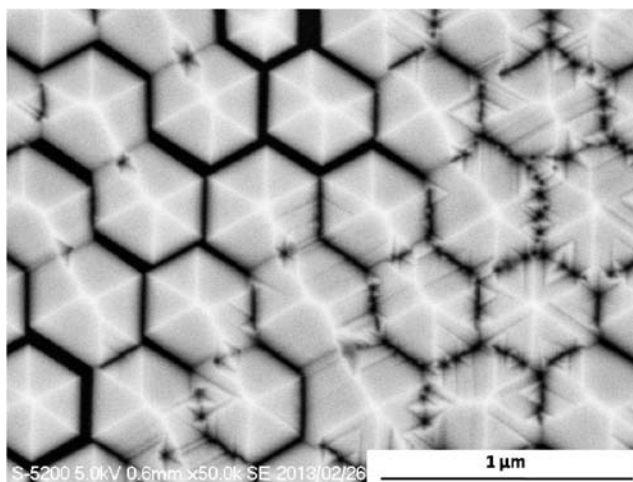
Figure 5.6 Plan-view SEM image of the GaN nanopyramids
grown with 100 sccm hydrogen flow.

The other approach to suppress the random growth was to elevate the growth temperature, from 800 ^{o}C to 850 ^{o}C in our experiment. The plan-view SEM image of the sample grown at 850 ^{o}C was shown in Fig. 5.7. The random growth was successfully suppressed by the higher growth temperature. Very regular nanopyramid arrays with uniform size were obtained. No abnormal large islands were observed. Both the "self limiting growth" as well as abnormal large islands were successfully suppressed.
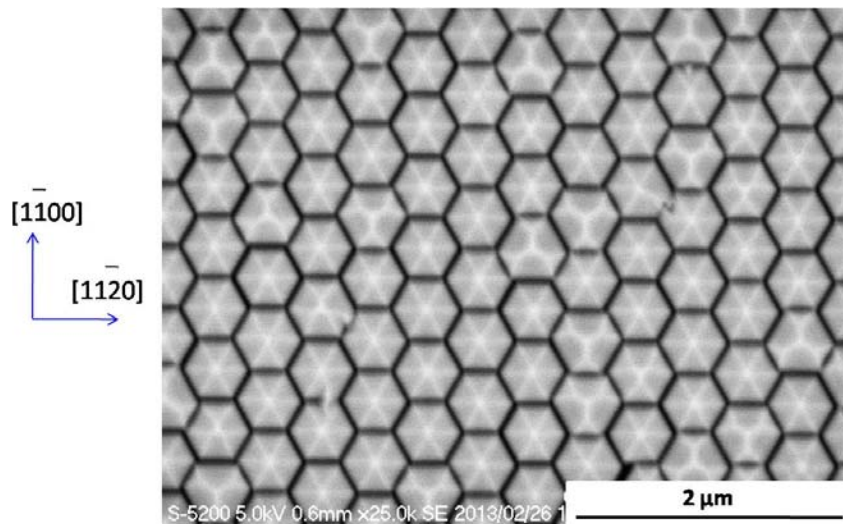

Fig. 5.7 Plan-view SEM image of the GaN pyramids grown at 850 ^{o}C in a N$_2$ ambient.

5.3 Growth and properties of MQWs on GaN nanopyramids

Five-period InGaN/GaN quantum wells were subsequently grown at 760 ℃, followed by a GaN cap layer. The TEG and TMI (only for quantum well growth) flow rates were 15.56 and 10.38 μmol/min, respectively. The growth time for InGaN quantum well and GaN barrier were 1, 6 min, respectively. Figure 5.8 show plan-view and cross-sectional SEM images of 5 period InGaN/GaN MQWs grown on the nanopyramids.
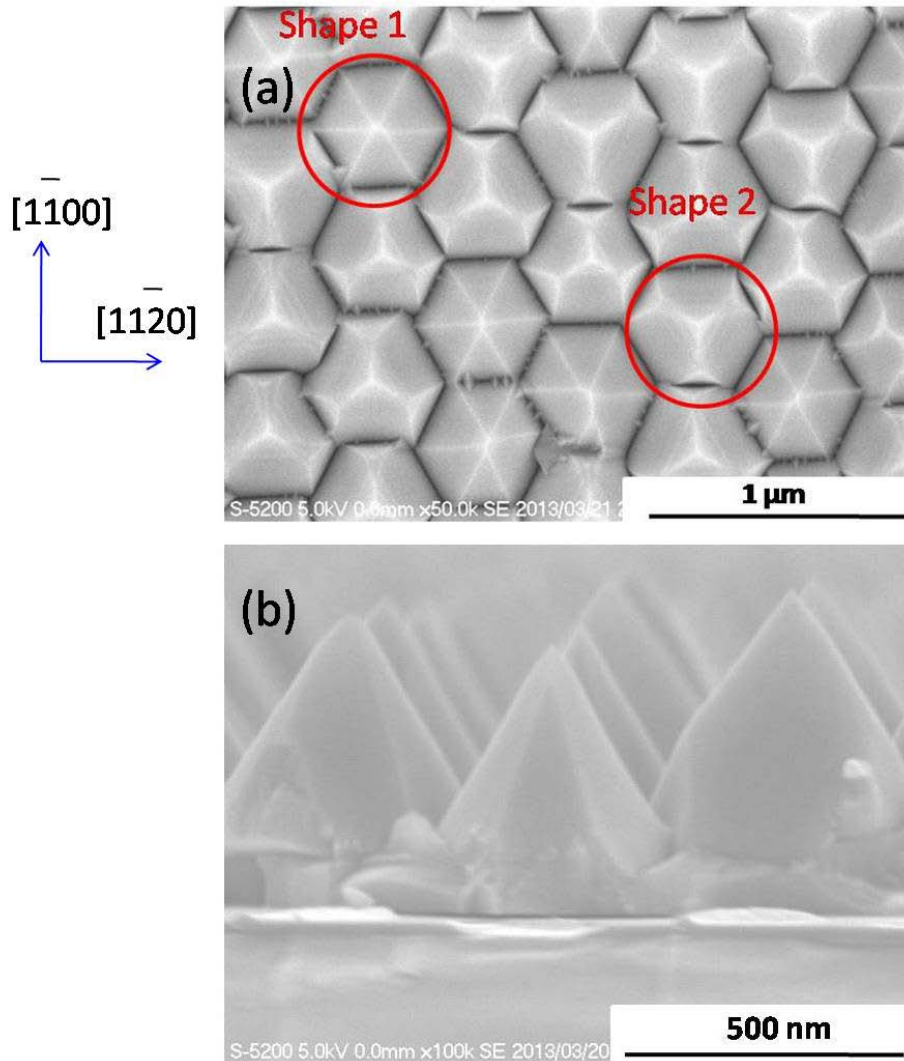
Figure 5.8 show plan-view and cross-sectional SEM images
of 5 period InGaN/GaN MQWs grown on the nanopyramids.

The spacing between adjacent nanopyramids became so small that the pyramids started to coalesce. The coalescence process was initiated by forming small crystalline as "bridges" when the spacing became small enough. The thicknesses of the InGaN quantum wells as well as the GaN barrier were measured by TEM (Fig. 5.9). Although the MQW growth condition should result in an InGaN quantum well and barrier thickness of 4.5 and 15 nm on planar templates, the

MQWs grown on the semipolar (1-101) planes showed a thickness of only 1.2 and 8 nm, respectively. This confirmed the much lower growth rate on the semipolar planes.
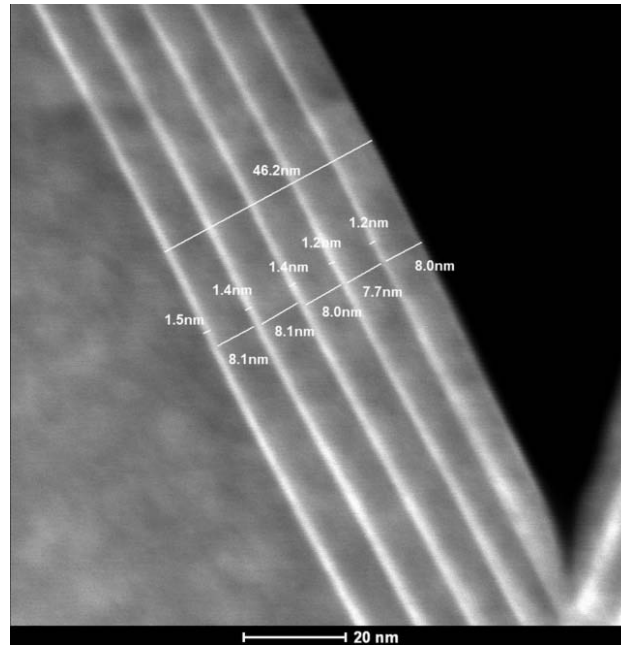
Fig. 5.9 TEM result of the MQWs grown on the semipolar (1-101) planes of the GaN pyramids.

In both Fig. 5.7 and Fig 5.8(a), two different shapes of pyramids could be observed. One shape was hexagonal pyramids with six fold symmetry (shape 1). The other shape also has six side planes. However, three planes were not fully developed. The three larger facets exhibited an angle of around 62° to the c-plane surface, which was the often reported (1-101) planes. The other three smaller facets exhibited an angle of around 73°, which was ascribed to (2-201) planes. Pyramids of this shape has a threefold symmetry and a triangle shaped apex (shape 2).
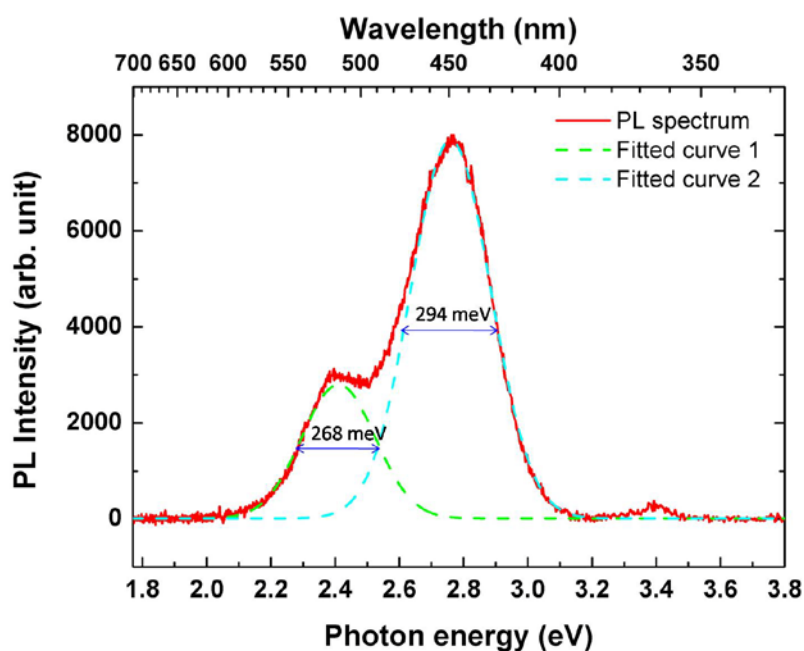
Fig. 5.10 Room temperature PL spectrum of MQWs grown on the nanopyramids.

The room temperature PL spectrum of MQWs grown on the nanopyramids is shown in Fig.

5.10. Two peaks originating from MQWs could be observed. By curve fitting, we derived one

peak with higher intensity centered at 2.76 eV with a FWHM of 294 meV, and another peak at

2.41 eV with lower intensity has a FWHM of 268 meV. To clarify the origin of peak emission, CL

measurement was carried out. Figure 5.11(a) shows the monochromatic CL spectrum of MQWs

grown on the nanopyramids. The two peaks in PL spectrum were also observed in the CL

spectrum. Figures 5.11 (b) and 5.11(c) show a plan-view SEM image and a plan-view

monochromatic CL image at a wavelength of 530 nm of the same location.
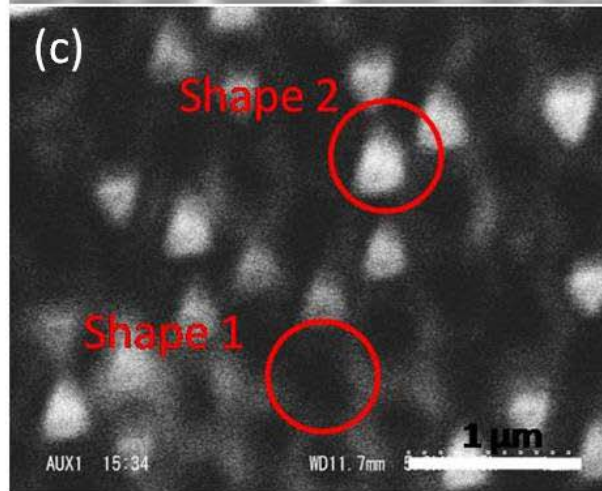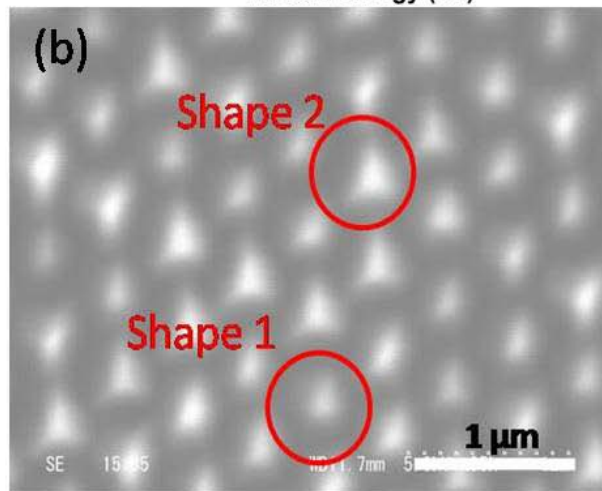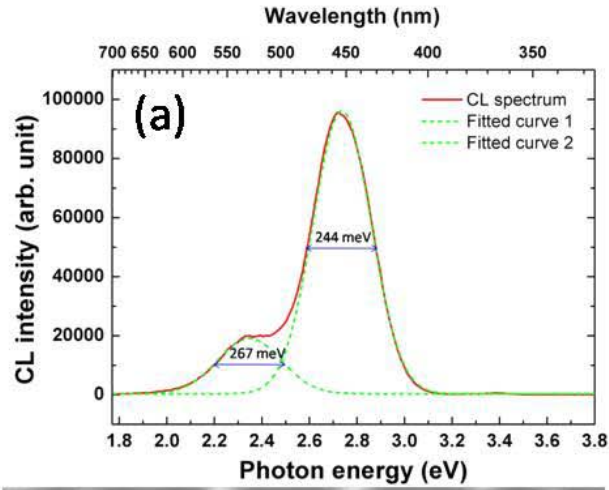
Figure 5.11 (a) Monochromatic CL spectrum of MQWs grown on the GaN pyramids, (b) plan-view SEM image and (c) plan-view monochromatic CL image at a wavelength of 530 nm of the same location.

The emission at 530 nm was only observed from the apexes of some pyramids. Comparing Figs. 5.11 (b) and 5.11(c), a relation between light emitting pyramids and pyramid shape could be observed. All the light emitting pyramids exhibited a triangle shaped apex, which means the emission at 530 nm wavelength originated from the apexes of the pyramids with a threefold symmetry. The monochromatic CL image at 460 nm along with the corresponding SEM image are shown in Figs. 5.12(a) and 5.12(b), respectively. In contrast to the CL image at 530 nm, the CL image at 460 nm showed a uniform emission intensity for all the pyramids in the whole area, which implied a quite uniform spatial distribution of the indium composition corresponding to the wavelength of 460 nm.
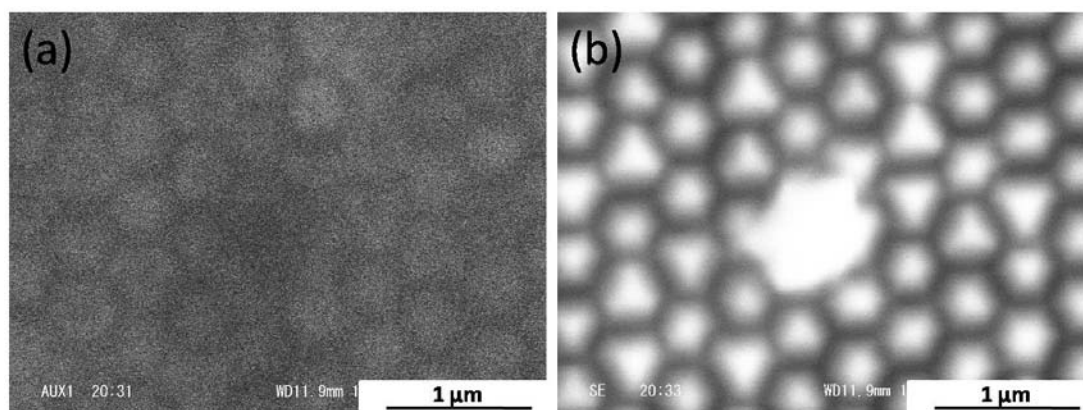
Figure 5.12 (a) plan-view monochromatic CL image at a wavelength of 460 nm
(b) plan-view   SEM image of the same location.

A detailed structure of the MQWs grown on nanopyramids was studied by transmission electron microscopy (TEM) measurement. Figure 5.13(a) shows a high-angle annular dark-field scanning TEM (HAADF-STEM) image of the cross section of MQWs grown on the nanopyramids. Surprisingly, we observed an embedded void in every nanopyramid. Figure 5.13(b) shows a bright

field TEM (BFTEM) cross-sectional image with a larger magnification. From Fig. 5.13(b), we found that new dislocations were generated at the regrowth interface. Besides the dislocations filtered by the SiO_2 mask, the dislocations that penetrated from the underlying template through mask window terminated at the bottom of voids along with the new generated dislocations. Almost no threading dislocations could be observed either above the voids or outside of the mask window area, which means an improved crystal quality by lateral overgrowth.
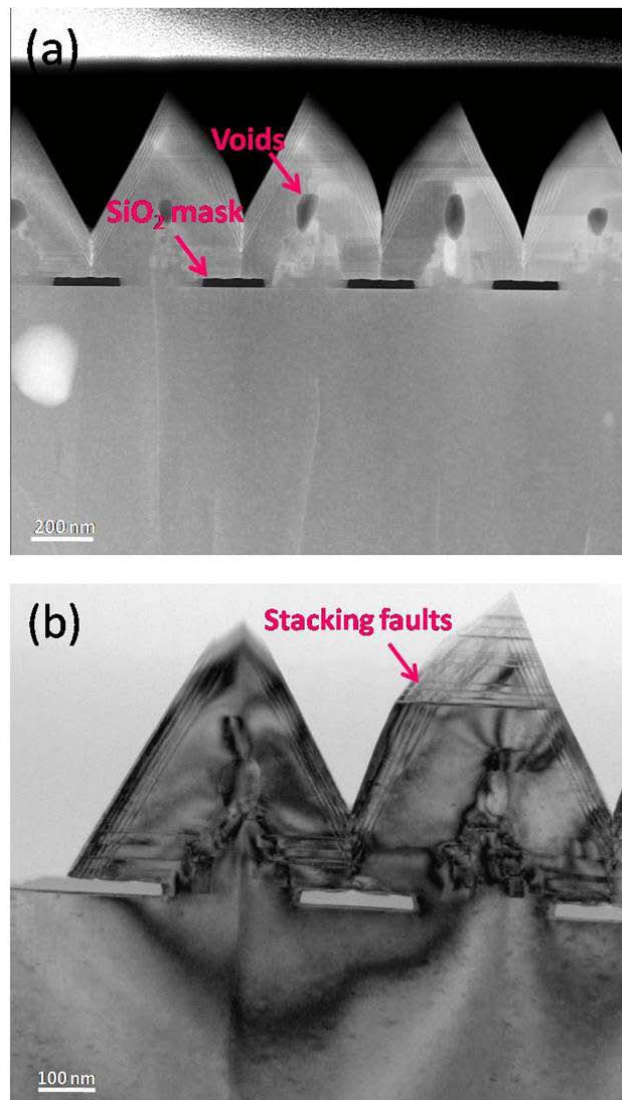
Figure 5.13 Cross-sectional HAADF-STEM image (a) and cross-sectional bright field
TEM image with a larger magnification (b) of the of MQWs grown on the nanopyramids.

The formation of new dislocations at the regrowth interface might be due to the relatively low growth temperature and using nitrogen as the carrier gas, which resulted in a very limited diffusion length. The adatoms could not dwell at the thermodynamically most stable sites. Moreover, the growth rate by SAG was promoted compared with on a planar sample. Therefore, at the initial growth stage, layer by layer growth was not achieved, which might be responsible for the formation of new dislocations at the interface. The formation of embedded voids inside pyramids could also be explained by the reduced diffusion length of adatoms. Because of selective area growth, there was a larger vapor phase precursor concentration at the window edge. Besides, there were also a large amount of adatoms supplied by surface diffusion from the mask to the edge of mask window, whereas at the center of window area the adatoms were provided by bare vapor phase diffusion. Higher precursor supply at the window edge caused the ridge growth as shown in Fig. 5.14. Due to the reduced diffusion length, the adatoms at the edge of mask window could not effectively migrate to the center region. This resulted in a much faster growth rate at the edge than at the center region. As the growth proceeded, the height of the GaN grown at the edge became larger than the center. When the growth fronts of the edges merged, the concave center stopped growing, and an embedded void formed. This process is schematically illustrated in Fig. 5.14.
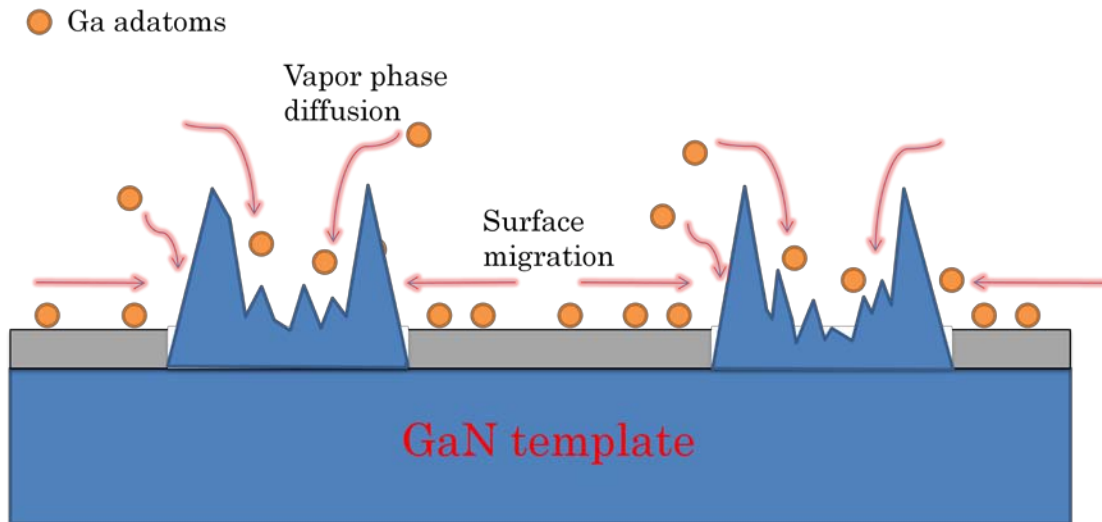
Fig. 5.14 Schematic of the embedded nanohole formation process.

Although there were very few threading dislocations at the top and the laterally grown region, stacking faults were usually observed. In particular, at the apexes of some pyramids, high-density stacking faults were clearly observed, whereas in some other pyramids stacking faults were not observed at the apexes, as shown in Fig. 5.13(b). Interestingly, it was found the pyramids with high-density stacking faults at the apex always exhibited an asymmetric shape, whereas the pyramids free of stacking faults showed a symmetric shape. Although at present there is no direct evidence, it's very likely the pyramids with stacking faults exhibited a shape of threefold symmetry and the pyramids without stacking faults at the apex exhibited a shape of six-fold symmetry (Fig. 5.15).
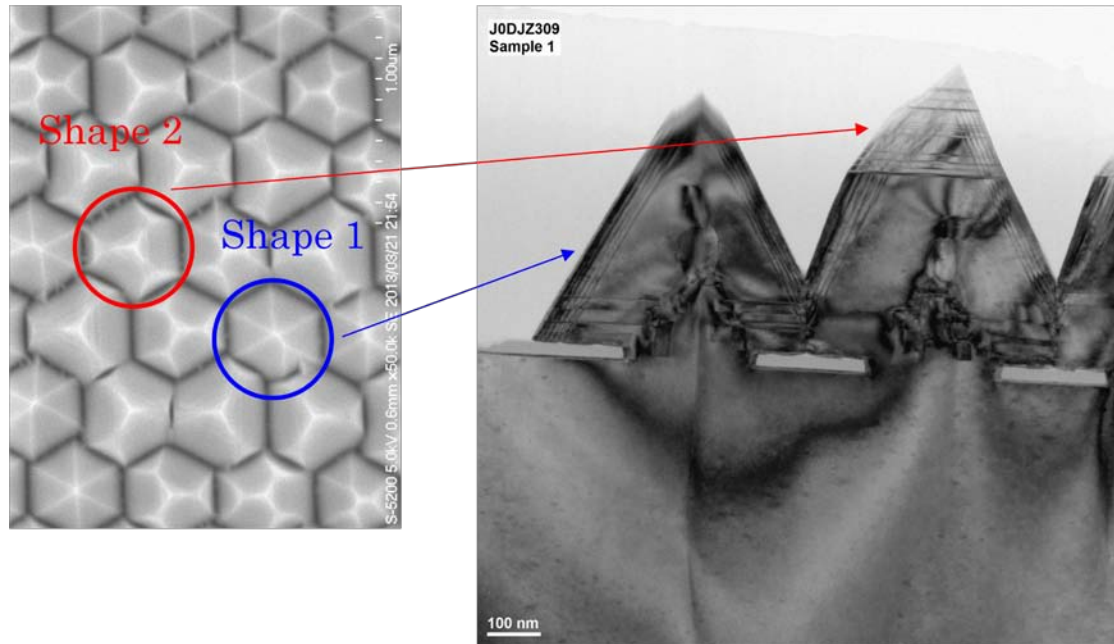
Fig. 5.15 Correlation between the pyramid shape and the high-density stacking faults at the apex.

In such case, the abnormal shape of the pyramids with threefold symmetry might be due to the formation of high-density stacking faults. The PL emission with longer wavelength at the apexes with a triangle shape might be tentatively explained by higher In incorporation rate caused by the stacking faults. The stacking faults could provide more kinks on the semipolar surfaces for capturing the adatoms. From Fig. 5.7 we found that during GaN nanopyramid growth and before the MQW structure was grown, pyramids with threefold symmetry had already formed, whereas in Fig. 5.13(b) the starting position of stacking faults was also clearly observed to be inside the GaN nanopyramids. Since such stacking faults was not reported previously in pyramid structures grown at high temperature in a hydrogen ambient previously,[20] the formation of stacking faults may be due to lower growth temperature and the nitrogen ambient. The same shapes have also

been reported by J. R. Chang et, al. when grew MQWs on GaN nanorods fabricated by top-down dry etching.[21] I. H. Wildeson et, al also reported planar defects at some of the nanopyrmid apexes.[14] We believe that the stacking faults formation might not be a particular case but a quite typical phenomenon when growing the apex of the nanopyramid structures under nitrogen ambient and relatively low growth temperature, especially when growing InGaN/GaN MQWs on this kind of nanostructures.

To confirm the fast coalescence using this approach, we continued to grow a 20-nm thick $Al_{0.2}Ga_{0.8}N$ electron blocking layer followed by a 300 nm p-GaN layer on the nanopyramids after the growth of MQWs. The p-GaN growth condition was listed in Table 5.1.

Table 5.1 Growth condition of p-GaN layer on the nanopyramids.

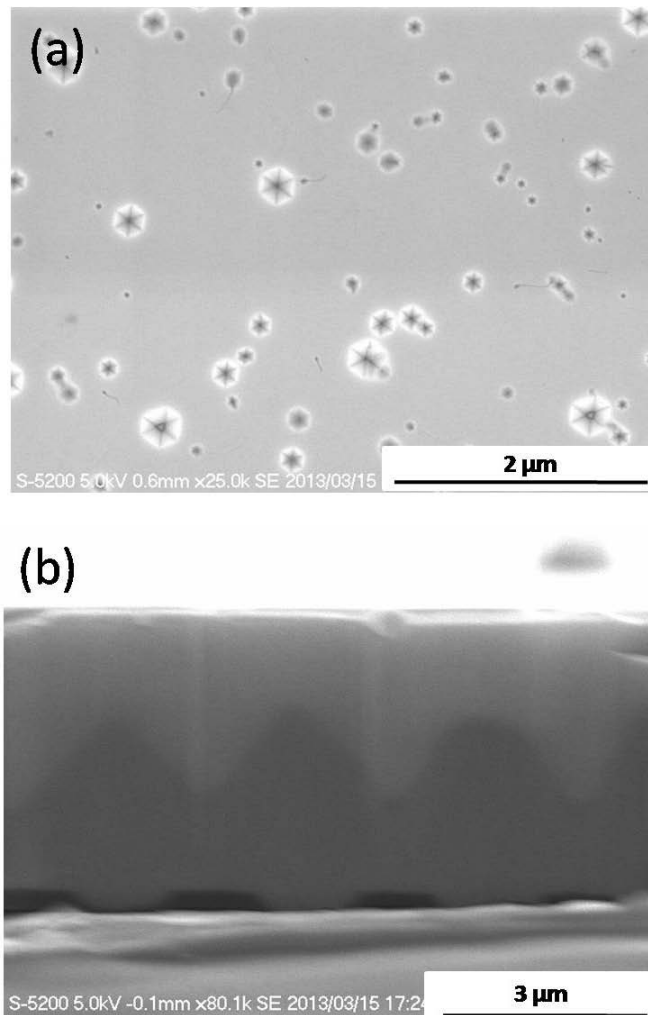|	
TMG (sccm)	15
$EtCp_2Mg$ (sccm)	60
NH_3 (SLM)	5
Growth Temp. (℃)	940
Pressure (torr)	200
Process Time (min)	12

Fig. 5.16 (a) Plan-view and (b) cross-sectional view SEM images of
300 nm p-GaN grown at 940 ^{o}C on nanopyramids after MQW growth.

The plan-view and cross-sectional view SEM images of the sample after p-GaN growth are

shown in Figs. 5.16(a) and 5.16(b), respectively. Full coalescence was achieved after growth.

However, there were many pits on the p-GaN surface. From the cross-sectional view image we

could observe the profile of the GaN pyramids. The coalescence was indeed achieved at the

targeted p-GaN thickness.

The p-GaN growth condition was further adjusted to suppress the pits and improve the surface

flatness. The growth temperature was raised to 1000 ^{o}C since higher growth temperature enhances lateral growth.[22] The plan-view and cross-sectional view SEM images after p-GaN growth are shown in Fig. 5.17.
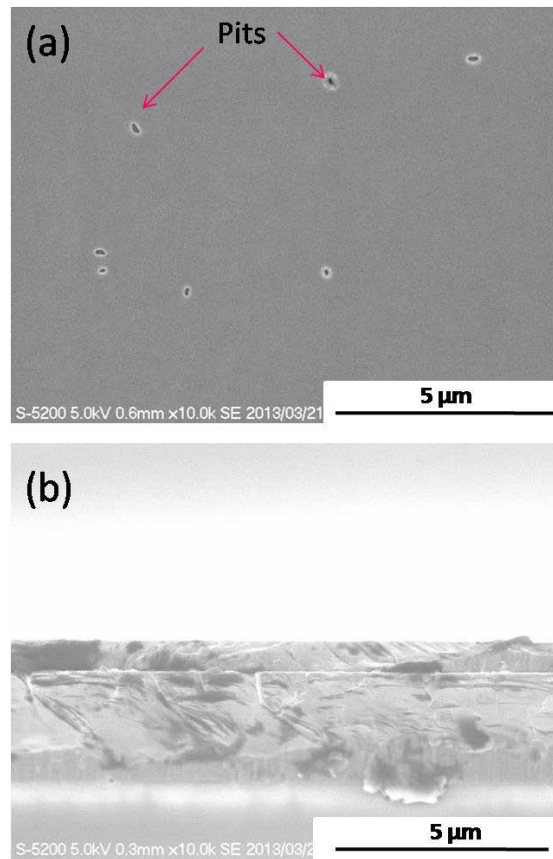

Fig. 5.17 (a) Plan-view and (b) cross-sectional view SEM images of
300 nm p-GaN grown at 940 ^{o}C on nanopyramids after MQW growth.

Full coalescence was achieved although a few small pits could be observed on the surface. This is in contrast to the partial coalescence after ~500 nm p-GaN growth.[14] This might be due to an imperfection of the SiO_2 nanohole mask. However, at some occasional locations, random growth was observed as shown in Fig. 5.18(a). This is probably because the random growth was not completely suppressed at 850 ^{o}C (Fig. 5.18(b)). The random growth could be suppressed by further optimizing the growth temperature.
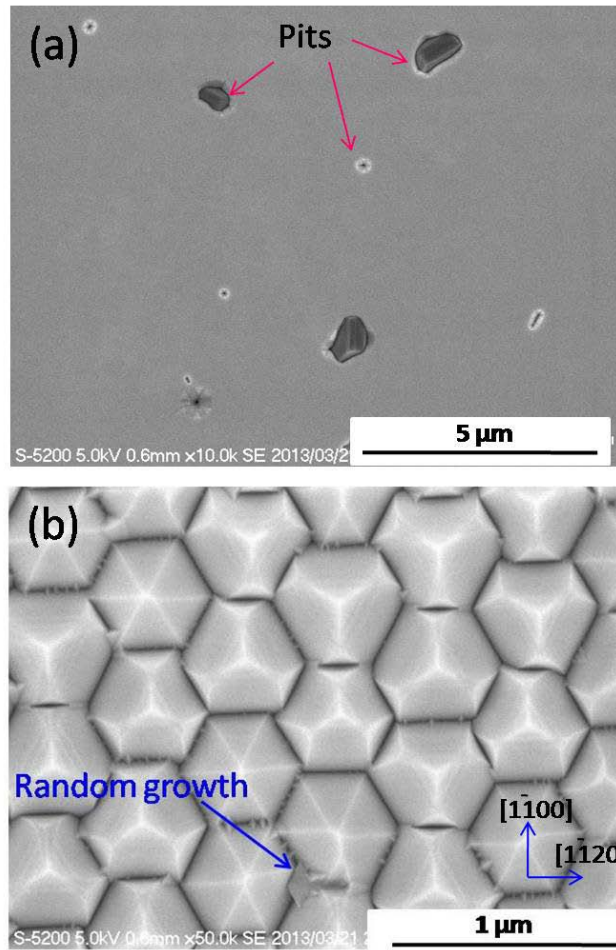
91

Fig. 5.18 (a) Random growth observed after p-GaN growth
(b) Occasional random growth observed after MQW growth.

Until now we used quite slow growth rate for GaN nanopyramid growth. However, similar

structure could also be obtained with a higher growth rate at a higher growth temperature using

nitrogen as carrier gas. Moreover, for application purpose, the new dislocations generated at the

regrowth interface and the embedded nanoscale voids need to be eliminated. We did some further

investigation of the growth condition with the showerhead configuration. Since the embedded

voids and the new dislocation generation was not observed when growing pyramids at high

temperature and hydrogen ambient, we tried a strategy to grow the nanopyramid "cores" using

hydrogen as the carrier gas first, and then switch to nitrogen ambient to uniformly enlarge the pyramid size. In the experiments, TMG was used instead of TEG and the Ga source supply was changed from 15.56 to 52 μmol/min. Therefore, the growth rate was greatly elevated. The nanopyramid core was first grown at a temperature of 980 ^{o}C in an hydrogen ambient for 8 min. Then the carrier gas was switched to nitrogen for 10 min growth, the other growth condition was kept the same. The plan-view SEM image of the sample was shown in Fig. 5.19.
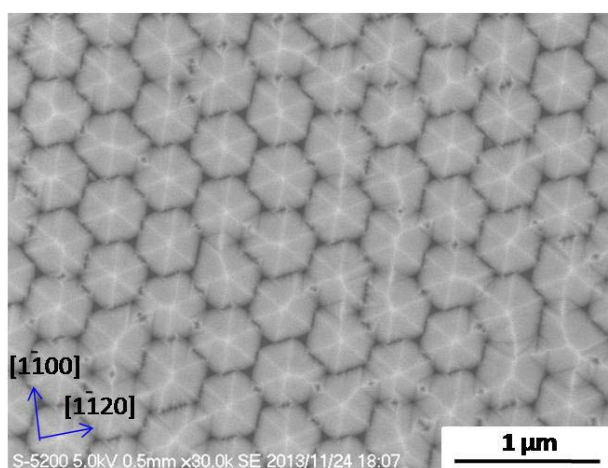
Fig. 5.19 Plan-view SEM image of GaN nanopyramids grown with a high growth rate.

Similar nanopyramid arrays were obtained with this high growth rate. No abnormal large islands were observed. However, there were "steps" on the pyramid surface, which was very similar to the previous case when a small amount of hydrogen was introduced. This might be due to more efficient NH$_3$ decomposition at high temperature, which generated more hydrogen.

5.4 Summary

In this chapter, InGaN/GaN MQWs grown on GaN nanopyramids were studied.

93

Unlike previous reported nanopyramids which had sizes restricted by the mask window, we successfully grew size-controllable nanopyramids by using lower growth temperatures and nitrogen as the carrier gas instead of hydrogen. The pyramid size was highly uniform and the abnormal growth of large islands was successfully suppressed. The nanopyramids exhibited two types of shapes, one had a six-fold symmetry and the other showed a threefold symmetry. There were two PL emission peaks from MQWs grown on the nanopyramids. The longer-wavelength peak originated only from the apexes of pyramids with threefold symmetry, where high-density stacking faults were observed. The high-density stacking faults might be responsible for the higher indium incorporation at the triangular apexes of the pyramids. In every nanopyramid an embedded void was observed. The formation mechanism was explained by a higher growth rate at the edge than at the center of the window region caused by SAG and the small diffusion length. After 300 nm p-GaN growth following the growth of MQWs, fully coalesced flat p-GaN surface was achieved, confirming the fast coalescence by this method.

References

1) T. Takeuchi, S. Sota, M. Katsuragawa, M. Komori, H. Takeuchi, H. Amano, and I. Akasaki: Jpn. J. Appl. Phys. **36** (1997) L382.

2) S. F. Chichibu, T. Sota, K. Wada, O. Brandt, K. H. Ploog, S. P. DenBaars, and S. Nakamura: Phys. Status Solidi A. **183** (2001) 91.

3) T. Wang, D. Nakagawa, J. Wang, T. Sugahara, and S. Sakai: Appl. Phys. Lett. **73** (1998) 3571.

4) H. Masui, S. Nakamura, S. P. DenBaars, and U. K. Mishra: IEEE Trans. Electron Devices **57** (2010) 88.

5) M. Funato, M. Ueda, Y. Kawakami, Y. Narukawa, T. Kosugi, M. Takahashi, and T. Mukai: Jpn. J. Appl. Phys. **45** (2006) L659.

6) A. E. Romanov, T. J. Baker, S. Nakamura, and J. S. Speck: J. Appl. Phys. **100** (2006) 023522.

7) Y. J. Hong, C. H. Lee, A. Yoon, M. Kim, H. K. Seong, H. J. Chung, C. Sone, Y. J. Park, and G. C. Yi: Adv. Mater. **23** (2011) 3284.

8) Y. H. Ko, J. H. Kim, L. H. Jin, S. M. Ko, B. J. Kwon, J. Kim, T. Kim, and Y. H. Cho: Adv. Mater. **23** (2011) 5364.

9) R. Leute, D. Heinz, J. Wang, F. Lipski, T. Meisch, K. Thonke, J. Thalmair, J. Zweck, and F. Scholz: J. Cryst. Growth **370** (2013) 101.

10) W. H. Goh, G. Patriarche, P. L. Bonanno, S. Gautier, T. Moudakir, M. Abid, G. Orsal, A. A. Sirenko, Z. H. Cai, A. Martinez, A. Ramdane, L. Le Gratiet, D. Troadec, A. Soltani, and A. Ougazzaden: J. Cryst. Growth **315** (2011) 160.

11) J. Bai, Q. Wang and T. Wang: J. Appl. Phys. **111** (2012) 113103.

12) V. Ramesh, A. Kikuchi, K. Kishino, M. Funato, and Y. Kawakami: J. Appl. Phys. **107** (2010) 114303.

13) C. H. Chiu, P. M. Tu, C. C. Lin, D. W. Lin, Z. Y. Li, K. L. Chuang, J. R. Chang, T. C. Lu, H. W. Zan, C. Y. Chen, H. C. Kuo, S. C. Wang, and C. Y. Chang: J. Sel. Top. Quantum Electron. **17** (2011) 971.

14) I. H. Wildeson, R. Colby, D. A. Ewoldt, Z. W. Liang, D. N. Zakharov, N. J. Zaluzec, R. E. Garcia, E. A. Stach, and T. D. Sands: J. Appl. Phys. **108** (2010) 044303.

15) C. Liu, P. A. Shields, Q. Chen, D. W. E. Allsopp, W. N. Wang, C. R. Bowen, T. L. Phan, and D. Cherns: Phys. Status Solidi (c) **7** (2010) 32.

16) C. W. Liu, A. Satka, L. K. Jagadamma, P. R. Edwards, D. Allsopp, R. W. Martin, P. Shields, J. Kovac, F. Uherek, and W. Wang: Appl. Phys. Express **2** (2009) 121002.

17) K. Y. Zang and S. J. Chua: physica status solidi (c) **5** (2008) 1585.

18) S. Kitamura, K. Hiramatsu and N. Sawaki: Jpn. J. Appl. Phys. **34** (1995) L1184.

19) D. Kapolnek, R. D. Underwood, B. P. Keller, S. Keller, S. P. Denbaars, and U. K. Mishra: J. Cryst. Growth **170** (1997) 340.

20) T. Kim, J. Kim, M. S. Yang, S. Lee, Y. Park, U. I. Chung, and Y. Cho: Appl. Phys. Lett. **97** (2010) 241111.

21) J. R. Chang, S. P. Chang, Y. J. Li, Y. J. Cheng, K. P. Sou, J. K. Huang, H. C. Kuo, and C. Y. Chang: Appl. Phys. Lett. **100** (2012) 261103.

22) K. Hiramatsu, K. Nishiyama, A. Motogaito, H. Miyake, Y. Iyechika, and T. Maeda: Phys. Status Solidi A. **176** (1999) 535.

6. LED Structure Grown on Nanohole-patterned Templates

6.1 Background and Motivation

In recent years, nanostructures such as nanorod and nanopyramid structures have been intensively studied by many groups for nitride growth.[1-4] In chapter 4 by thermally etched nanoporous templates, the dislocation density of the GaN template was reduced and the light extraction efficiency was also greatly improved. However, the QCSE in the MQWs could not be effectively reduced since the MQWs were grown on coalesced planar c-plane surface. The MQWs directly grown on nanorod or nanopyramid structures take advantage of the nonpolar (1-100) or the semipolar (1-101) planes. MQWs grown on these planes could not only greatly reduce the QCSE leading to a better internal quantum efficiency but also achieve a larger light emitting area. However, just as the MQWs grown on the nanopyramids in chapter 5, MQWs grown on these nanostructures usually exhibit a quite broad spectrum, which is caused by the different growth rates and indium incorporation at different locations of the nanostructures.[5,6] Moreover, directly forming good ohmic p-contact on such nanostructures is quite difficult due to the textured surface. LEDs grown on nanostructures with flat surface by p-GaN coalescence have been reported. However, the coalescence usually required a thick p-GaN layer,[2,3,7] which resulted in a large serial resistance. In chapter 5 we proposed an approach to effectively control the nanopyramid size and surface planarization with reduced p-GaN thickness was realized. However, the expected light extraction efficiency will also be minimized by forming a flat surface. In this chapter, we designed a new nanohole-patterned GaN template for improving the light extraction efficiency. MQWs as

well as LED structures were grown on the nanohole-patterned templates. Compared with the nanorod or nanopyramid structures, continuous c-plane surface remains after regrowth on a nanohole template. The light emission is quite uniform on the c-plane surface. The p-contact on flat c-plane surface might be easier to fabricate than on sharply textured semipolar (1-101) planes. An improved current spreading is also expected with respect to the isolated nanorod structure. The nanohole template is partially strain relaxed or even strain free at the surface, providing a possibility to reduce the QCSE. High light extraction efficiency can be preserved even after growing p-GaN layer by forming distinct nanostructures.

6.2 Growth of MQWs on Nanohole Patterned Templates

2-inch GaN template of 3 µm thickness was used for the nanohole template fabrication. The nominal diameter and center-to-center spacing of the holes were 230 and 460 nm, respectively. The etching depth was about 500 nm. The details of the fabrication process was described in chapter 3. Plan-view and inclined-view SEM images of the nanohole template were shown in Fig 6.1(a) and 6.1(b), respectively.
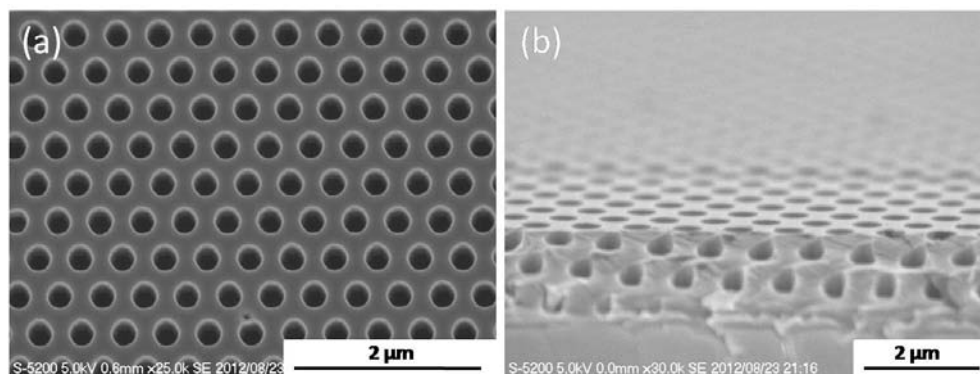

Fig. 6.1 (a) plan-view and (b) inclined-view SEM image of a fabricated nanohole template.

Strain relaxation in MQWs could reduce the strain induced QCSE and improve the radiative recombination rate. The strain state of the nanohole template was characterized by Raman spectra, The Ramn spectra after curve fitting is shown in Fig. 6.2. The peak positions of the GaN E_2^{high} mode were 569.1, 568.4, and 567.5 cm^{-1} for a planar GaN template, a nanohole GaN template, and a bulk GaN substrate (spectrum not shown here), respectively.
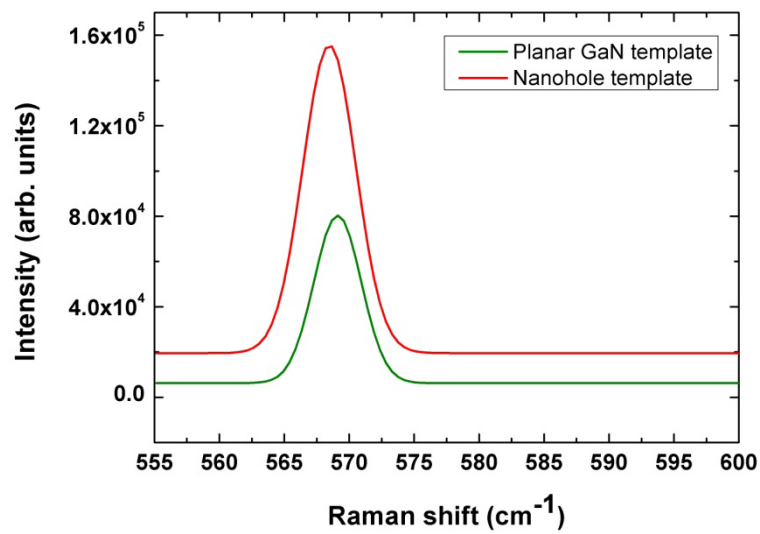

Fig. 6.2 Fitted Raman spectra of a planar GaN template and a GaN nanohole template.

The 0.7 cm^{-1} difference in peak position between the nanohole template and the planar GaN template corresponds to a stress relaxation by ~0.17 GPa, while the total stress of the planar GaN template was 0.38 GPa according to Ref. 8. Due to the limited etching depth, there was still a quite thick GaN film underneath the nanohole arrays. The strain relaxation might be underestimated because the Raman measurement adopts a 532 nm wavelength laser which has a deep penetration depth in the GaN film. The spectrum of the nanohole sample also includes signal from the

underlying GaN film. Besides the commonly used Raman spectrum, the peak position shift of

GaN bandedge emission in PL spectrum has also been reported for strain characterization.[9,10]

Compared with Raman measurement, the PL measurement has a much shorter penetration depth

due to the stronger absorption of the light with a shorter wavelength, therefore most of the signal

should be from within the nanohole etching depth. The PL spectra were measured with a 325 nm

He-Cd laser and the spectra were shown in Fig. 6.3. The peak wavelengths were 364.2, 365.0,

365.0 nm for the planar GaN template, the nanohole template and the bulk GaN substrate,

respectively.
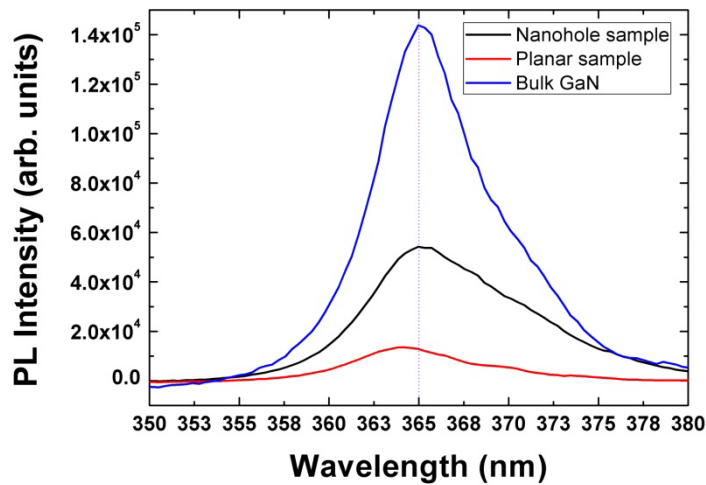
Fig. 6.3 PL spectra of a planar GaN template, a nanohole template,
and a bulk GaN substrate.measured with a 325 nm He-Cd laser.

Several planar and nanohole samples were measuered. The peak wavelengths of planar sample

were mostly at 363~364 nm, while all the nanohole templates showed a peak at 365 nm. The

redshift of the nanohole template might be associated with the relaxation of compressive stress. A

rough estimation of the in-plane stress was also conducted using the PL peak shift and a linear proportionality factor of 20 meV GPa^{-1}.[11] The derived stress 0.37 GPa of the planar GaN template agreed well with the value of 0.38 GPa calculated by the Raman spectra. The peak wavelength of nanohole sample was the same as the bulk GaN substrate, which implied an almost complete strain relaxation at the surface of the nanohole template. The PL intensity of the nanohole template also showed a four-fold increase compared with the planar GaN template, which was attributed to the increased light extraction efficiency.

After removing the residual SiO_2 by hydrogen fluoride and standard surface cleaning, the nanohole template was loaded into an MOVPE chamber for regrowth. Five-period InGaN/GaN quantum wells were grown on the nanohole template. TEG, TMI were used as the III precusors and ammonia were used as the V precursor. Nitrogen was used as the carrier gas. First the nanohole template was thermal cleaned at 950 ℃ for 5 min. Then the temperature was decreased to 760 ℃ for MQWs growth. The regrowth started by growing a GaN barrier. After MQW growth, finally the sample was capped with a GaN layer of 15 nm. The flow rates of TEG and TMI (only for quantum well growth) were 15.56 and 7.78 umol/min, respectively. A large NH_3 flow rate of 8 SLM was used to prevent InGaN decomposition. Figure 6.4 shows the plan-view SEM images of the nanohole sample after MQW growth.
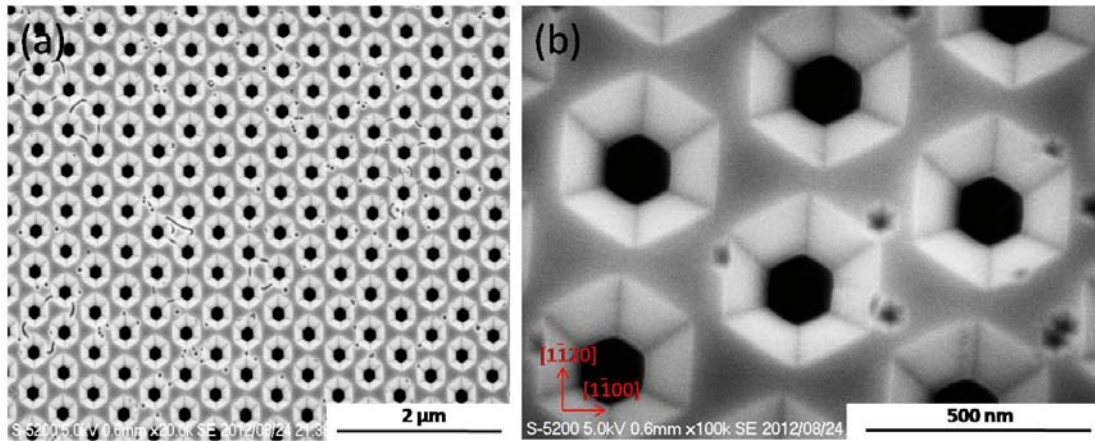
Fig. 6.4 Plan-view image (a) and plan-view image with larger magnification (b) of 5-period InGaN/GaN MQWs grown on a nanohole template.
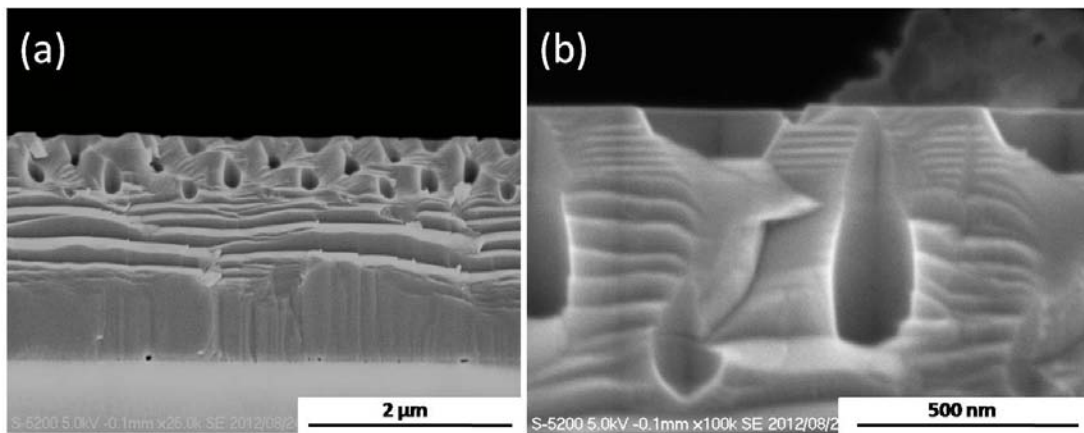

Fig. 6.5 Cross-sectional view (a) and cross-sectional view with larger magnification (b) of 5-period InGaN/GaN MQWs grown on a nanohole template.

The cross-sectional view SEM images are shown in Fig. 6.5. The shape of the holes was changed from round shape to hexagonal, and very smooth crystal planes were formed, which implies a recovery of surface damage caused by dry etching. According to the previously reported results,[2,5] the newly formed crystal planes were assigned as the {1-101} semipolar planes. The development of semipolar planes were accompanied by a decrease of both c-plane area and nanohole diameter. The diameter of the nanohole reduced from 255 nm to 157 nm, and the spacing

between edges of adjacent nanoholes reduced from 157 and 78 nm. From the cross-sectional view

image, we found that the MQWs were clearly observed on flat c-plane area but hard to discern on

the semipolar planes or sidewalls. This was due to much lower growth rates on the semipolar and

nonpolar planes. Similar results have also been reported for MQWs grown on other

nanostructures.[5,6] From the sample surface, some pits could be observed including some

line-shaped "pits". It was reported previously that the pits on the surface of InGaN/GaN MQWs

were related to the threading dislocations of the underlying GaN layer. However, at this point it

was not clear whether the formation of pits on the nanohole template could be explained in the

same way. The PL spectrum of MQWs grown on the nanohole template was shown in Fig. 6.6.

The PL spectrum of a planar control sample grown in parallel was also shown for comparison.
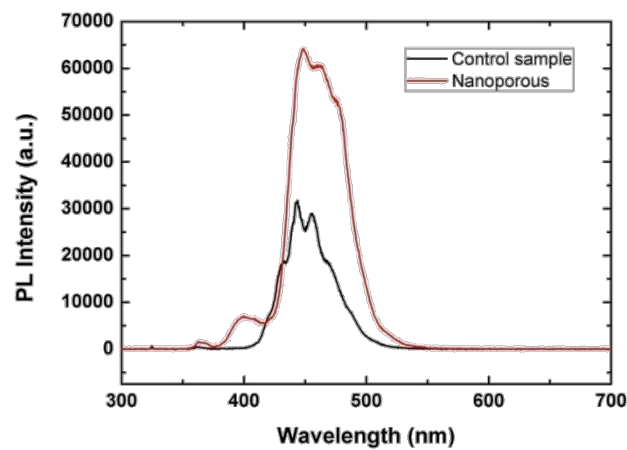

Fig. 6.6. PL spectra of MQWs grown on the nanohole template
and a planar GaN template.

The PL intensity of the nanohole sample showed a two-fold increase compared with the planar

sample. Compared with the planar sample, the spectrum of the nanohole sample showed a slight

red shift of peak position and a little broader FWHM. The FWHM of the nanoporous sample and the planar sample were 51 and 45 nm, respectively. The PL peak of the nanohole sample deviated from the Gaussian curve. Such broader peak of the nanohole sample might be due to a larger indium composition fluctuation compared with the planar sample. The integrated PL intensity of the nanohole sample was 2.5 times as that of the planar sample. Because the PL intensity of the nanohole GaN template showed even higher enhancement (~4 times enhancement) as shown in Fig. 6.3 compared with a planar GaN template due to the improved LEE, it's not likely that the PL intensity enhance of the MQWs was due to an improvement of the internal quantum efficiency, but probably also due to the improved LEE.

Sometimes much more dense pits on the MQW surface could be observed. The sample shown in Fig. 6.7 was grown using the same growth condition mentioned above. It's not likely the dense pits was formed due to the threading dislocation of the underlying GaN since the quality of the nanohole templates were almost the same. The origin of this phenomenon is still not clear at present. We suppose this might be because at the initial growth stage, layer-by-layer growth was not realized as a result of the very low diffusion length of the adatoms under such growth condition.
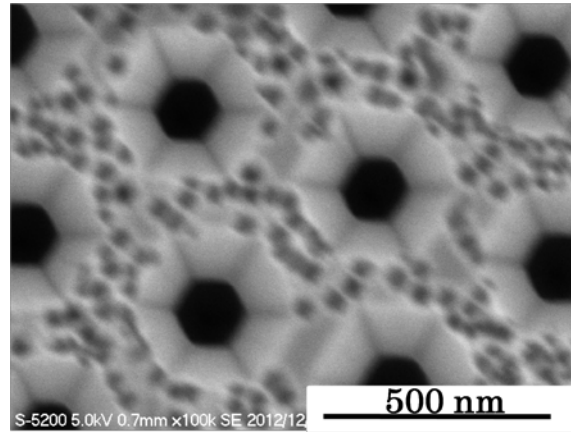
Fig. 6.7 Dense pits observed on the MQW surface due to a changed growth condition.

The spectrum of MQWs grown on the nanohole template with dense pits showed a 43%

increase in integrated PL intensity compared with a planar sample as shown in Fig. 6.8. Although

there were dense pits on the surface, the sample showed similar PL spectrum and intensity as the

previous sample with flat c-plane surface. The spectrum of the nanohole sample also showed a

broader peak and a slight redshift. Regarding the rougher surface of the nanohole sample, we

suppose the slightly broader peak for the nanohole sample was probably due to a larger indium

composition inhomogeneity in the MQWs grown on the nanohole template.
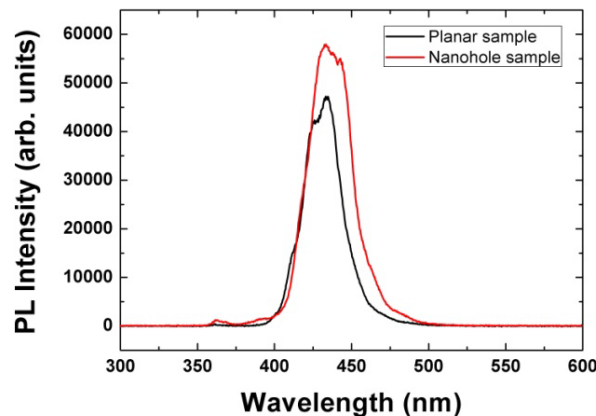
Fig. 6.8 PL spectra of MQWs grown on the nanohole template
with dense pits and on a planar sample.

From the previous reports, for MQWs on strain relaxed templates fabricated by top-down dry etching including nanohole structure, a blueshift of the PL peak position was usually observed.[12-14] This is caused by a reduction of internal electric field in the quantum wells, which results in an increase in bandgap energy. On the other hand, the strain relaxation by nanostructures was also reported to improve indium incorporation efficiency.[15] Therefore, a redshift in PL spectrum would be expected. To clarify the origin of this redshift, XRD (002) 2θ-ω scan and reciprocal space map (RSM) of the asymmetric (105) reflection was used to study the structural properties of the MQWs. From the RSM of (105) asymmetric reflection in Fig. 6.9, we confirmed that the MQWs were coherently grown on the nanohole template.
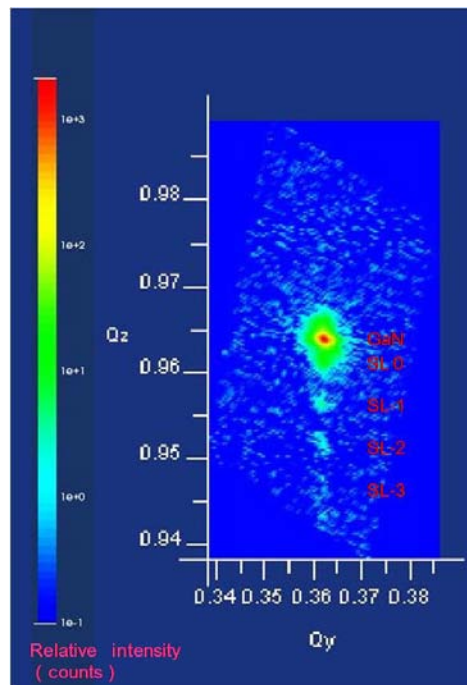

Fig. 6.9 XRD RSM of the asymmetric (105) reflection
of MQWs grown on the nanohole template.

It was reported that to relax the strain a certain thickness of mismatched layer was required.[16] Despite the nanoscale dimension of the nanohole template, the thickness of the InGaN wells was only around 5 nm, the strain relaxation might be very limited within such small thickness. In addition, compared with the lattice mismatch between InGaN well and the GaN template, the lattice constant change of GaN due to strain relaxation was quite small, therefore, the strain relaxation inside the InGaN well should be quite limited. Therefore, according the XRD result, it seems that strain relaxation played a minor role in the increase of PL intensity.

By fitting (002) 2θ-ω scan curve in Fig. 6.10 with a commercial software, the respective well widths and indium composition ratios of 5.15 nm, 8.9% and 6.7 nm, 6.2% for the control sample and the nanohole sample were obtained.
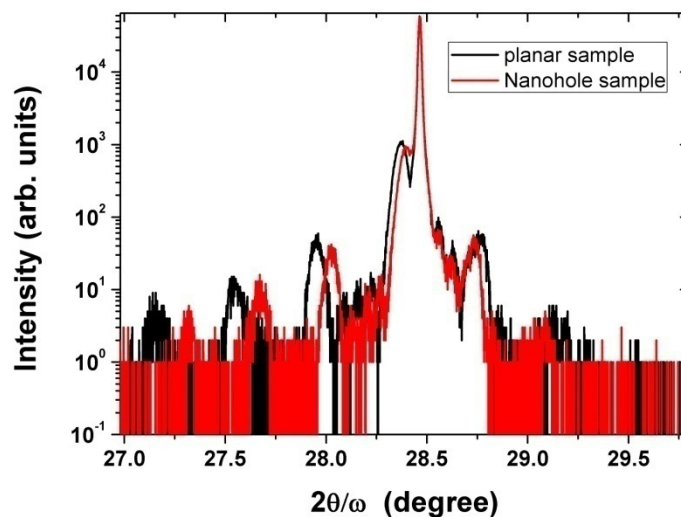

Fig. 6.10 (002) 2θ-ω scans for MQWs on a planar template and a nanohole template.

The slight redshift of PL peak in Fig. 6.8 was probably due to a wider InGaN well. The faster growth rate might be caused by a larger average concentration of precursors at the surface of the nanostructure. Surprisingly, we derived a lower indium composition for the nanohole sample although both higher growth rate and strain relaxation should promote the indium incorporation rate. At present the reason is not clear, one possible explanation is because of a faster desorption rate of indium on the nanostructures due to a higher surface energy. Similar phenomenon was also observed when growing (10-11) plane semipolar GaN on Si stripes.[17]

To study the origin of the light emission, CL measurement was carried out. Figures 6.11(a) showed the CL spectrum of MQWs on the nanohole template. Figures 6.11(b)-(e) were monochromatic CL images acquired at 390, 420, 460 and 480 nm, respectively. It could be clearly observed that a weak emission at around 400 nm was from the semipolar planes whereas the dominant broad peak originates from the emission of the c-plane MQWs. MQWs grown on nanostructures such as nanopyrmid or nanorods often exhibited a broad peak. At different locations, the quantum well thickness and In composition were different. However, in the nanohole sample, the dominant light emission came from MQWs grown on c-plane, and in the range of the dominant peak, the spatial distribution of the emission wavelength was quite uniform.
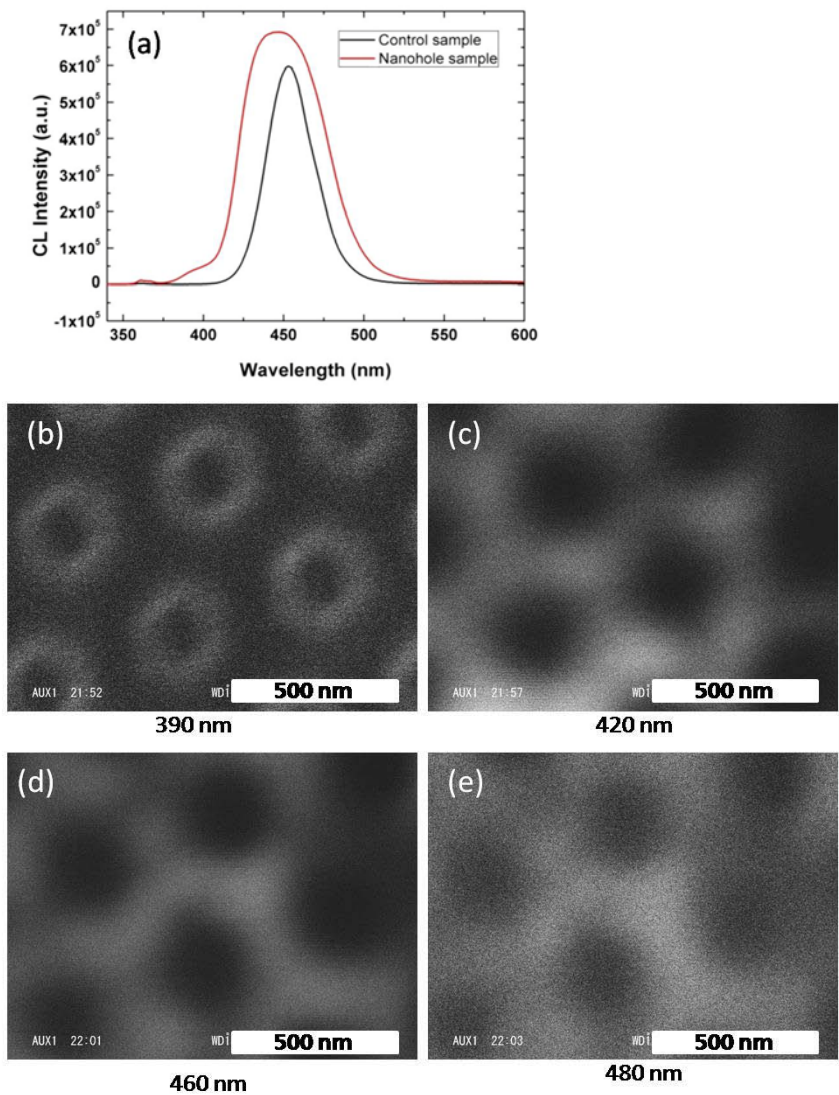
Figures 6.11 (a) CL spectrum of MQWs on the nanohole template.

(b)-(e) monochromatic CL images acquired at 390, 420, 460 and 480 nm.

6.3 LED Structure Grown on the Nanohole Templates

For LED structure, a 20 nm thick undoped $Al_{0.2}Ga_{0.8}N$ layer and a p-GaN layer with a thickness

of 130 nm was grown after the growth of MQWs. The chamber pressure was 250 Torr and the

growth temperature was 940 ℃. The same structure was also grown on a planar GaN template in

parallel for comparison. A schematic of the LED structure is shown in Fig. 6.12(a). The plan-view

and cross-sectional view SEM images of a full LED structure grown on the nanohole template are

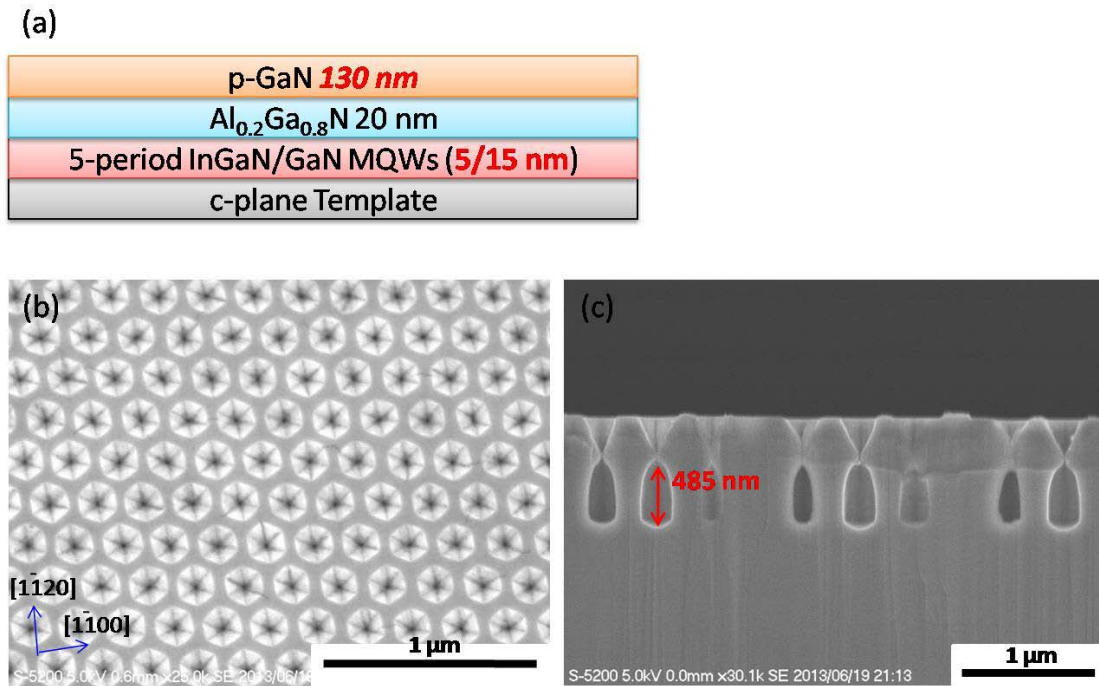shown in Figs. 6.12(b) and 6.12(c), respectively.

Fig. 6.12 (a) Schematic of the LED structure, (b) plan-view and (c) cross-sectional view SEM images of the LED structure grown on the nanohole template.

After growth, two types of nanostructure arrays were observed. At the p-GaN surface, very regular inverted-pyramid shaped arrays with smooth inclined crystal planes formed. The diameter of the inverted pyramids was about 360 nm. After growth the nanoholes were still not completely buried but leaving pores with a diameter of about 20 nm. The diameter of the pores could be adjusted by changing the growth time. The continuous c-plane area remained after growth. Another nanoscale embedded void array formed under the inverted-pyramid array. Actually there was an embedded void under every inverted pyramid. The height of the voids was around 480 nm. The c-plane MQWs were between these two arrays. This distinct structure could greatly improve the light extraction efficiency by strong scattering effect.

There were two critical factors that affect such distinct structure. The size of the embedded voids was strongly dependent on the nanohole etching depth. Figure 6.13 showed a cross-sectional view SEM image of a LED structure grown on a nanohole template with smaller depth (~350 nm). The size of the embedded voids became much smaller.
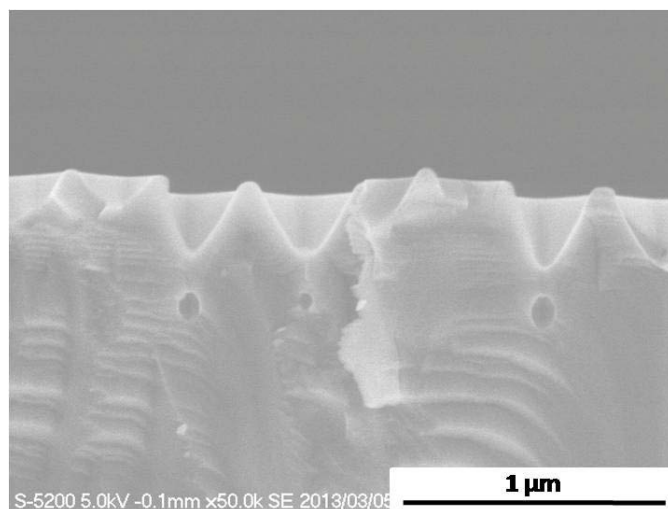

Fig. 6.13 Cross-sectional view SEM image of a LED structure
grown on a nanohole template with smaller depth (~350 nm).

The thickness of p-GaN layer is the other factor. If the thickness of the p-GaN layer is too thick, then the inverted pyramids on the top p-GaN layer would be completely filled up and the p-GaN will form flat surface. Figure 6.14 showed such case. The p-GaN layer was a little thicker (~150 nm). Part of the inverted pyramids were buried.
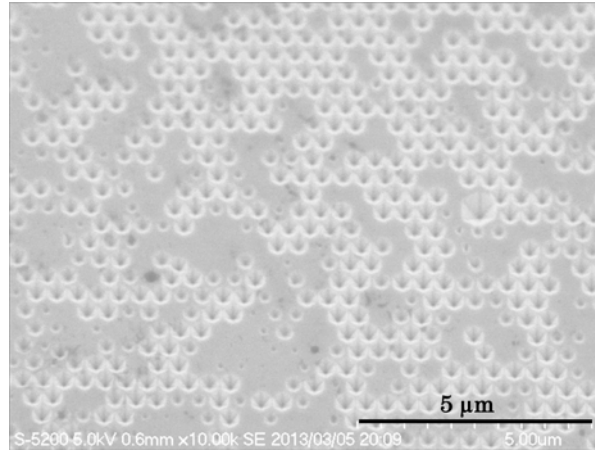
111

Fig. 6.14 Thicker p-GaN layer (~150 nm). Part of the
inverted pyramids were buried.

In such case, the light extraction efficiency would be degraded. Figure 6.15(b) showed the

panchromatic CL image of the partially flattened sample in Fig. 6.14. A corresponding SEM image

at the same location is shown in Fig. 6.15(a). It could be observed clearly that the flat area had a

lower intensity which was due to a lower light extraction efficiency.
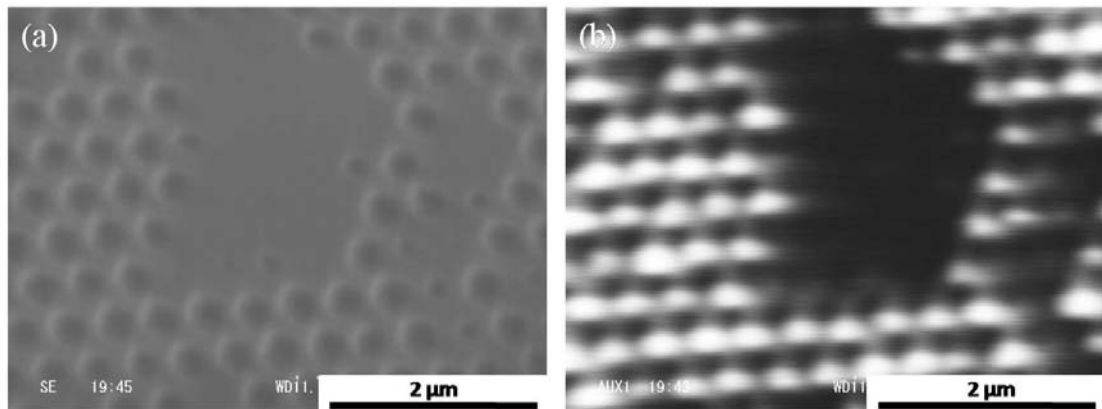

Fig. 6.15 (a) SEM image (b) panchromatic CL image of the same location in the partially
flattened sample.

LED device was fabricated with the standard device fabrication process for planar LEDs.

Although the almost fully coalesced p-GaN layer was expected to facilitate direct fabrication of

112

electrode without a planarization step with spin on glass, however, the fabricated LED device

exhibited a large leakage current and the light emission was quite weak. In order to clarify the

poor performance of the LED device, TEM measurement was carried out. Figure 6.16 (a) shows a

cross-sectional view bright field TEM image. The MQWs on the c-plane are not clear which

implies poor crystal quality of the MQWs. From the HAADF STEM image in Fig. 6.16(b), the

dislocations inside the MQWs could be more clearly observed.
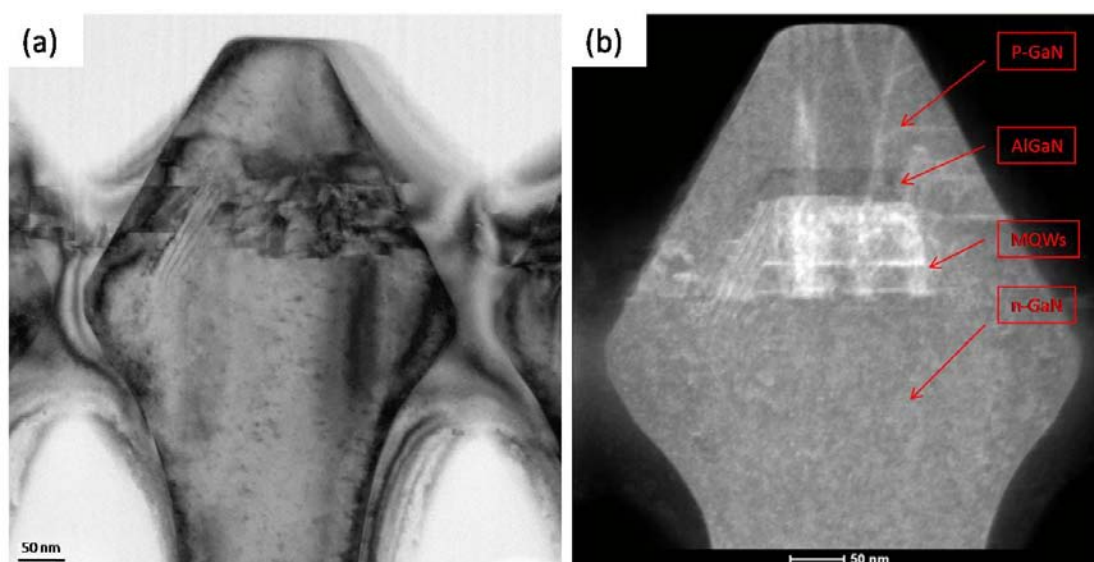

Fig. 6.16 (a) BFTEM image (b) HAADF STEM image of the LED structure grown on the nanohole template.

From the TEM images, we also found that there were also some metal deposited onto the

sidewalls of the embedded voids during TEM sample preparation by focused ion beam. This might

be because the voids were not completely embedded but left with small pores. This means it's also

likely that during p-electrode fabrication, the metal Ni could also penetrate through pores and

deposit on the sidewalls of the voids. In that case, even if the contact area is quite small, the

p-electrode will directly contact with the n-GaN. Besides the poor crystal quality of the MQWs, the p-electrode might also account for the large leakage current and weak light emission.

To improve the MQW crystal quality and control the nanohole diameter, we tried to initiate the regrowth by a high temperature GaN in hydrogen ambient. In Chapter 5, when growing nanopyramids in a nitrogen ambient, new dislocations generate at the regrowth interface were also observed. Therefore, starting the regrowth by low temperature with nitrogen carrier gas may generate new dislocation and degrade the crystal quality. By adjusting the high temperature GaN thickness, we may control the nanohole diameter to become sufficiently small before p-GaN growth. In that way, the p-GaN layer and the p-electrode will not contact with the underlying n-GaN. The growth was performed with the showerhead configuration. The regrowth was initiated by grown a silicon doped GaN layer at 1050 ^{o}C for 13 min in hydrogen ambient, the growth thickness was about 230 nm. Figure 6. 17(a) shows a plan-view image of the nanohole template after the high-temperature GaN growth. We found that the nanohole hole diameter became smaller and the c-plane area was extended. The regrowth temperature is a important factor for structure control. If the regrowth is initiated at 950 ^{o}C with other parameters kept the same, the semipolar planes will extend and the c-plane area decreases, as shown in Fig. 6.17(b).
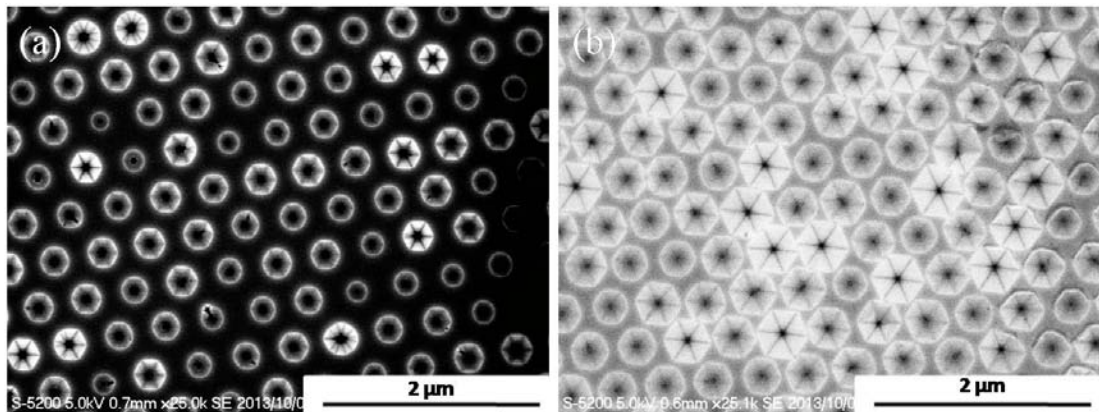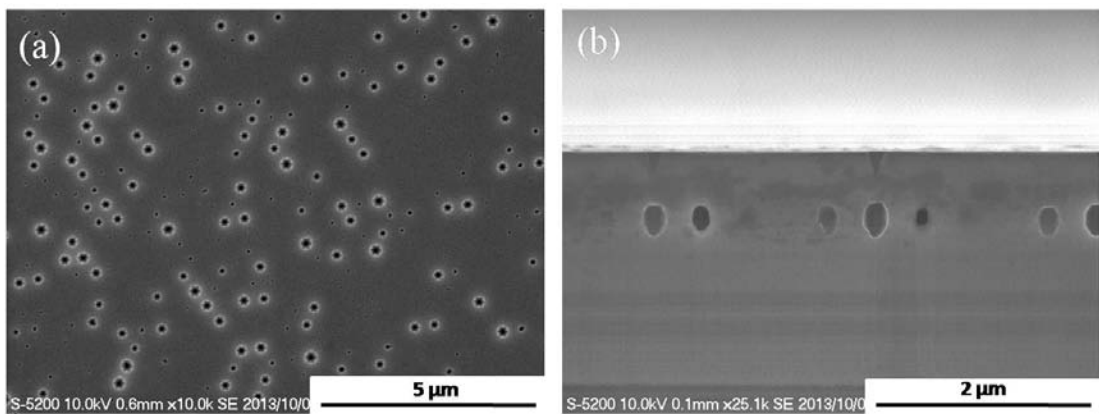
Fig. 6. 17 Plan-view image of the nanohole template after growing a silicon doped GaN layer at 1050 $^{\circ}$C (a) and 950 $^{\circ}$C (b) for 13 min.

Then five-period InGaN/GaN quantum wells were grown. The thicknesses for the quantum well and barrier were 3.7 and 9.5 nm, respectively. The chamber pressure was 200 Torr and the growth temperature was kept at 780 ℃ for MQWs growth. The plan-view and cross-sectional view SEM images of the nanohole sample after MQW growth were shown in Figs. 6.18(a) and 18(b), respectively.

Figs. 6.18 (a) plan-view and (b) cross-sectional view SEM images of the MQWs grown on the nanohole template.

Two nanostructure arrays were also observed. However, the surface was partially flattened and the size of the remaining holes was also small. The room temperature PL spectra of the MQWs grown on the nanohole sample and on a planar control sample were shown in Fig. 6.19. Despite of a reduced light emitting area, the spectrum of MQWs grown on the nanohole template showed a 4 fold increase in integrated PL intensity and exhibited a broader peak. Compared with the 2.5 fold increase reported previously, the more enhanced PL intensity might be related to a better crystal quality caused by the initial high-temperature growth. Moreover, the pit density became lower and the line-shaped "pits" were not observed. The full width at half maximum of the PL spectra for the planar sample and nanohole sample were 21 and 47 nm, respectively. A slight shift of the peak position from 455 to 464 nm was also observed, which is in agreement with the previous results.
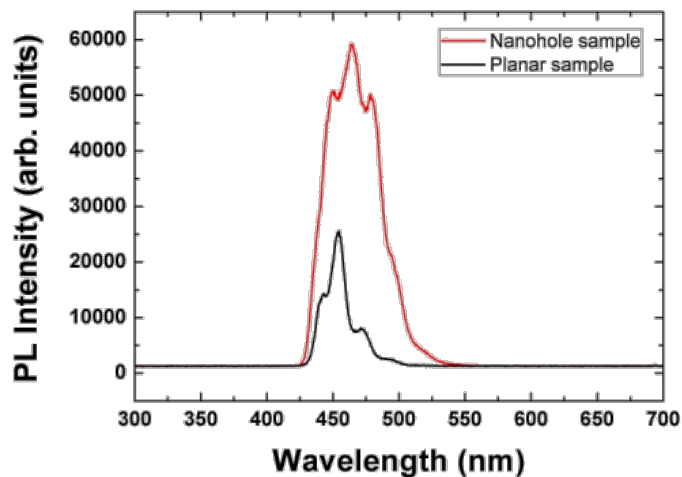

Fig. 6.19 Room temperature PL spectra of the MQWs grown
on the nanohole sample and on a planar control sample.

For the LED structure, following the MQW growth 20 nm thick undoped $Al_{0.15}Ga_{0.85}N$ layer and a p-GaN layer with a thickness of 140 nm was grown at a growth temperature of 950 ℃. The embedded void array and the inverted pyramids on the surface were observed (Fig. 6.20). Compared with the sample after MQW growth, the sample after p-GaN growth had dedper inverted pyramids on the surface.
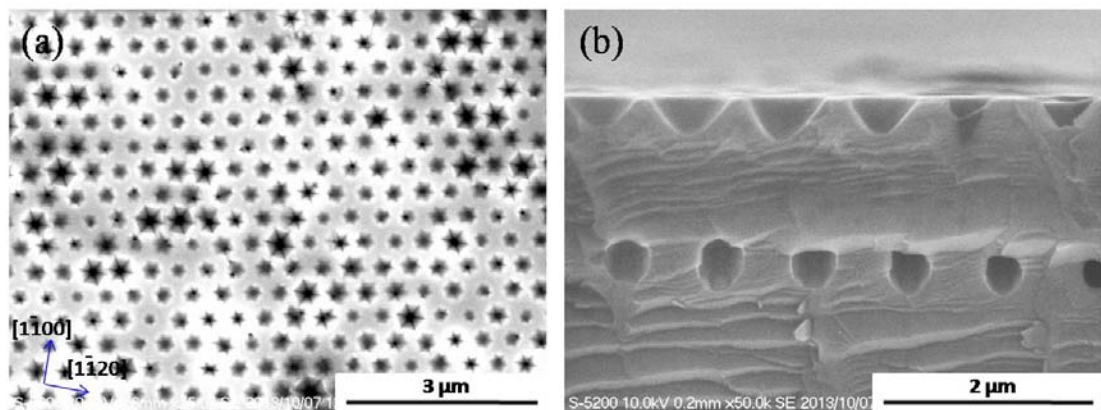

Fig. 6.20 (a) plan-view and (b) cross-sectional view SEM images of the LED structure grown on the nanohole template.

The PL spectra of the LED structures grown on a nanohole template and on a planar template were shown in Fig. 6.20. A 405 nm laser was used as the excitation source. As high as 3.5 times increase in integrated PL intensity was observed for LED grown on the nanohole template compared with that grown on a planar sample owing to a much improved light extraction efficiency.
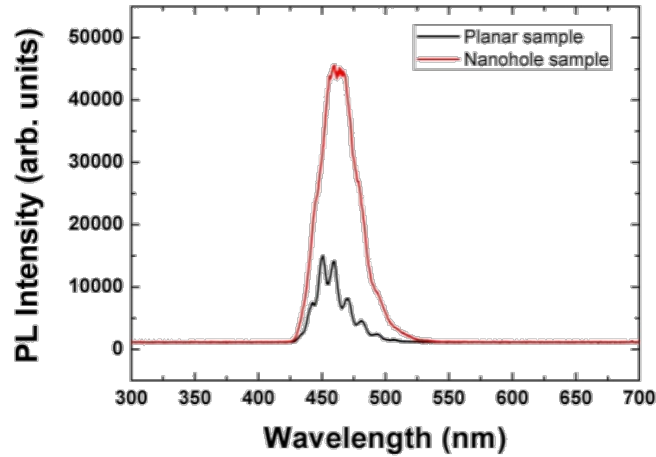
Fig. 6.21 Room temperature PL spectra of the LED grown
on the nanohole sample and on a planar control sample.

To confirm the increased PL intensity was mainly due to the greatly enhanced light extraction

efficiency, the internal quantum efficiency of a LED structure grown on a nanohole template was

measured and compared with a planar LED grown in parallel. The IQE was measured using a 405

nm PL system with variable excitation power. The calculation is based on the theoretical model

proposed in Ref. 18. In bulk semiconductors, the main carrier-recombination mechanisms are

Shockley–Read–Hall nonradiative recombination An, bimolecular radiative recombination Bn^2,

and Auger nonradiative recombination Cn^3, where A, B, and C are the respective recombination

coefficients and n is the carrier concentration. The Auger recombination was not considered in our

experiment due to the weak excitation condition. The generation rate G and the IQE at steady state

can be expressed as

$$G = An + Bn^2, \quad (1)$$

$$IQE = Bn^2/(An + Bn^2) = Bn^2/G, \quad (2)$$

and the integrated PL intensity can be expressed as

$$I_{PL} = \eta Bn^2, \qquad (3)$$

Where η is a constant determined by the volume of the excited active region and the total collection efficiency of luminescence. By eliminating n in Eqs. (1) and (3), the generation rate could be expressed as

$$G = \frac{A}{\sqrt{\eta B}} I_{PL}^{1/2} + \frac{1}{\eta} I_{PL}, \qquad (4)$$

On the other hand, the generation rate G can be also calculated from experimental parameters using

$$G = P_{laser}(1\text{-}R)\alpha l/(A_{spot}lh\nu) = P_{laser}(1\text{-}R)\alpha/(A_{spot}h\nu), \qquad (5)$$

where P_{laser} is the excitation power of the laser source, R (17%) is the reflection at the sample surface, l (15 nm) is the total thickness of the InGaN QWs, A_{spot} (12.56 μm^2) is the area of the laser spot on the sample surface, hν (3.07 eV) is the energy of a 405 nm photon, and α (5.4 μm^{-1}) is the absorption coefficient of the InGaN well at 405 nm.
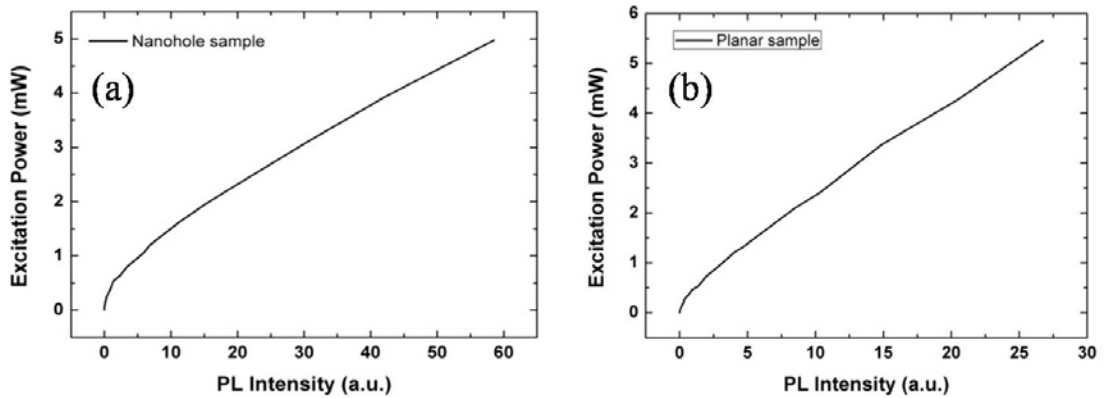

Fig. 6.22 Excitation power as a function of I_{PL} for (a) the nanohole sample and (b) the planar sample.

The experimental results for excitation power as a function of I_{PL} is shown in Fig. 6.22(a) and

6.22(b) for the nanohole sample and the planar sample, respectively. The carrier generation rate of

the nanohole sample and the planar sample obtained using Eq. (5) as a function of I_{PL} is shown in

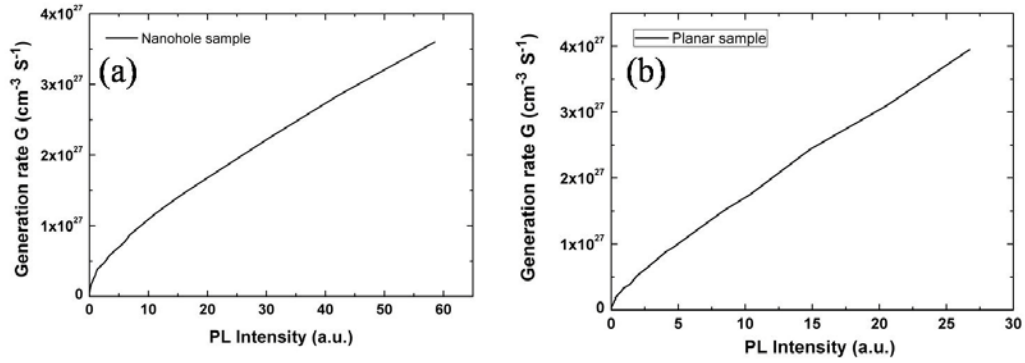Fig. 6.23. The corresponding graphs ploted in logarithmic coordinates are shown in Fig. 6.24.

Fig. 6.23 Calculated carrier generation rates for (a) the nanohole sample
and (b) the planar sample.
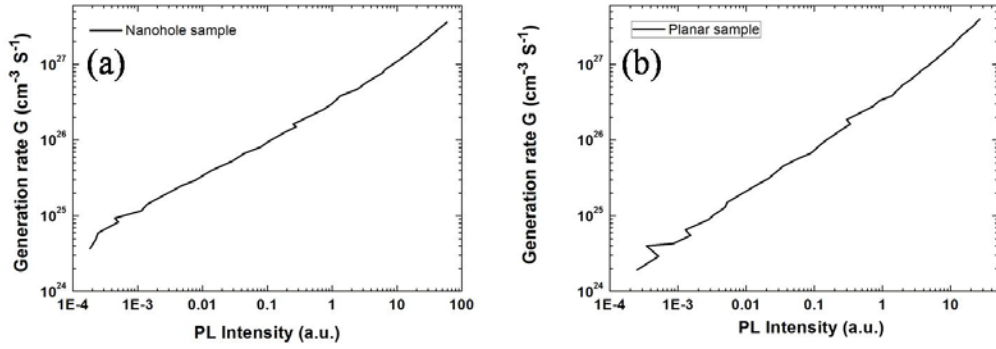

Fig. 6.24 Carrier generation rates for (a) the nanohole sample and (b) the planar
sample as a function of PL intensity in logarithmic coordinates.

Using Eq. (4) to fit the experimental data, we then obtain the coefficients $P_1=A (B\eta)^{-1/2}$ and

$P_2=1/\eta$. Eliminating A from $P_1=A (B\eta)^{-1/2}$ and Eq. (1) we get

$$G = P_1\sqrt{\eta}\sqrt{B}n + (\sqrt{B}n)^2, \quad (6)$$

By solving Eq. (6) for $B^{1/2}n$ and inserting into Eq. (2), the IQE is obtained. If one assumes a

value of B at room temperature of 1×10^{-10} cm^3/s, the value of carrier concentration n can also be

obtained. In Fig. 6.25, the measured IQE is plotted as a function of carrier concentration n for the

nanohole sample and the planar sample. The planar sample showed a higher internal quantum

efficiency than the nanohole sample at a carrier concentration of 4×10^{18} cm^{-3}. The crystal quality

of the MQWs grown on the nanohole template was affected by this nanostructure and was not as

good as the planar sample. Therefore, the great enhancement of the PL intensity for the nanohole

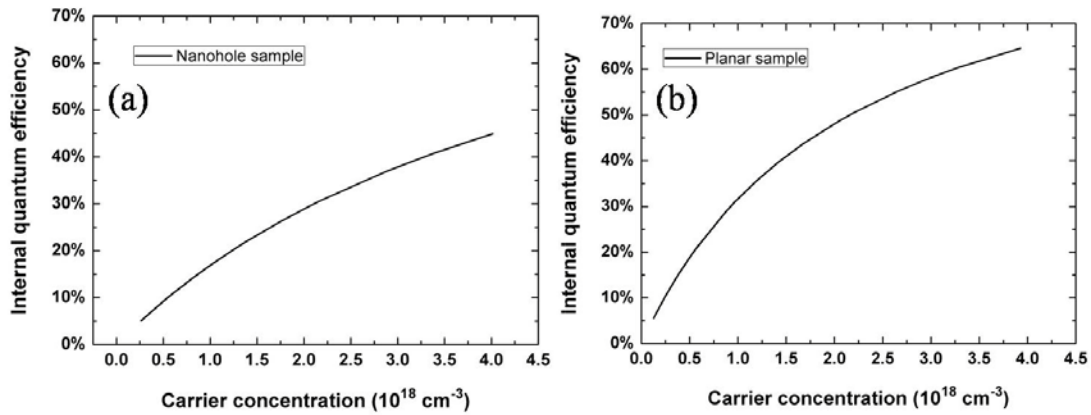sample was due to the great improvement of the light extraction efficiency.

Fig. 6.25 Calculated IQE plotted as a function of carrier concentration n for (a) the nanohole
sample and (b) the planar sample.

6.4 Simulation of the light extraction efficiency

The LEE of the nanostructures was simulated with a commercial software Poynting (Fijutsu).

This software was based on the finite difference time domain (FDTD) method. Software such as

LightTools could not be used for the simulation here since only geometric optics is considered.

When the size comes to the nanoscale, the same scale of the light wavelength, the diffraction

effect could not be neglected. The structure of the simulation is based on the LED structure shown in Fig.6.12.

Four types of LED structures were simulated: a conventional planar LED, a LED structure with embedded voids, a LED structure with inverted pyramids on the top surface and a LED structure with both embedded voids and inverted pyramids.

Due to the limited volume of the memory, the simulated size was choose to be 4×4 μm^2. Generally, the simulated structures consist of a 200 nm p-GaN layer, a 20 nm AlGaN electron blocking layer, a 25 nm InGaN layer, a 750 nm n-GaN layer and a sapphire substrate of 500 nm thickness. The p-GaN and n-GaN layer was set to have the same refractive index of 2.47. A InGaN layer with a thickness of 25 nm, which is equivalent to the total thickness of the InGaN quantum wells, was used instead of the MQWs for simplicity. The refractive indices of the InGaN layer and the AlGaN layer were set to be 2.8 and 2.4, respectively. The light absorption inside the chip was neglected. To save the memory volume, a n-GaN thickness of 750 nm and a sapphire thickness of 500 nm was used, which was much less than the real thickness of 430 μm. This would not obviously degrade the simulation results since the total absorption boundary condition was used in this simulation. On the contrary, we found that when a larger thickness was used, the accuracy would decrease because a larger portion of the light will be absorbed by the sidewalls due to the total absorption boundary condition. The embedded voids had a length of 480 nm and a width at the center of 250 nm. The inverted pyramids were set to have a depth of 260 nm and a diameter of

360 nm. Both the embedded voids and the inverted pyramids were distributed in a hexagonal array with a pitch of 460 nm. There was a embedded void under every inverted pyramid. A cubic light source with a small lateral size of 5 nm was set at the center of the InGaN layer. The wavelength was set to be 450 nm and the light emission duration was 30 fs. The grid was set to have a maximum size of 10 nm and a minimum of 5 nm. Such grid parameters were selected to save the memory volume and simulation time while keeping a sufficient accuracy for our simulation purpose. Plan-view and cross-sectional view images of the simulated LED structure with both embedded voids and inverted pyramids were shown in Fig. 6.26(a) and 6.26(b), respectively.
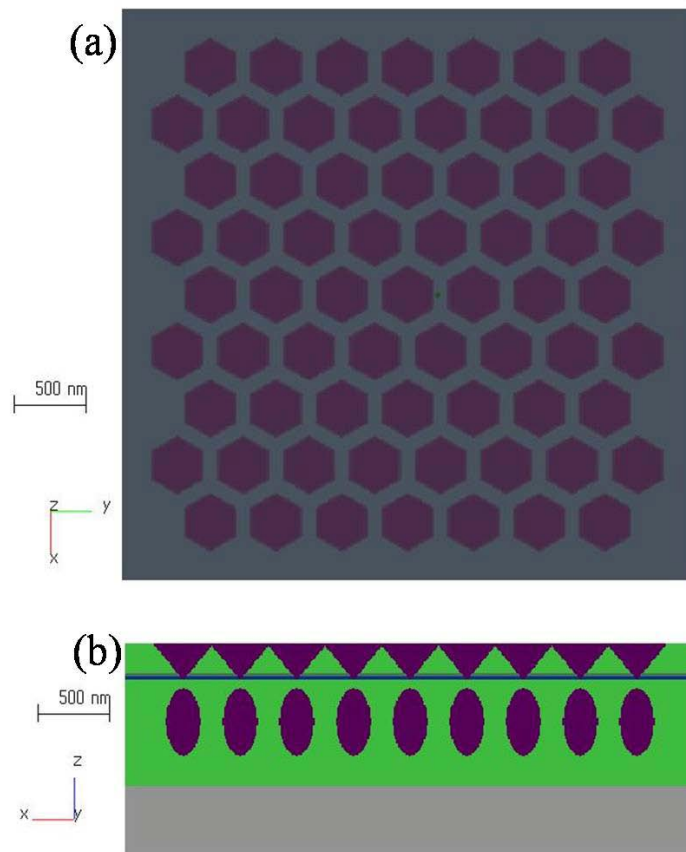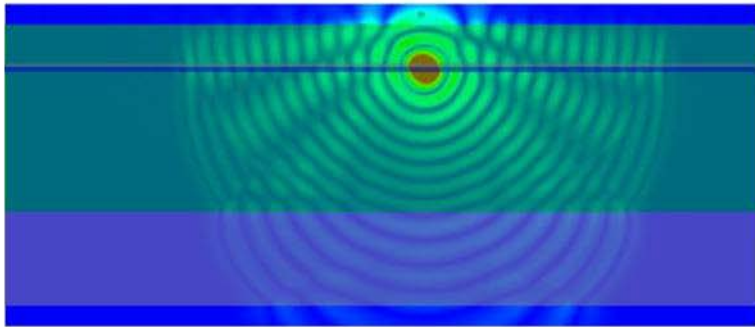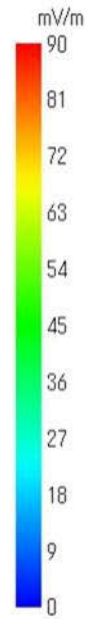

Fig. 6.26 (a) Plan-view and (b) cross-sectional view images of the simulated LED structure with both embedded voids and inverted pyramids.

The electromagnetic field distributions of the simulated structures at 11.25 fs were shown in Figs. 6.27(a)-(d). From the electromagnetic field distribution, we found that the light extraction was obviously enhanced by the nanostructures. The light propagation from the top surface was much enhanced by the inverted pyramids. On the other hand, the embedded nanoholes were more effective for light extraction from the bottom side.
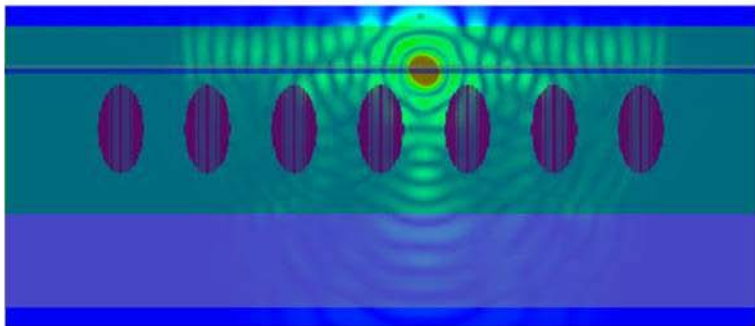

Cross-sectional view image of a planar LED

Cross-sectional view image of a LED with only nanoholes

(c)

Cross-sectional view image of a LED with only pyramids

(d)

Cross-sectional view image of a LED with both nanohole and pyramid structures
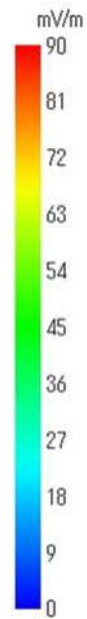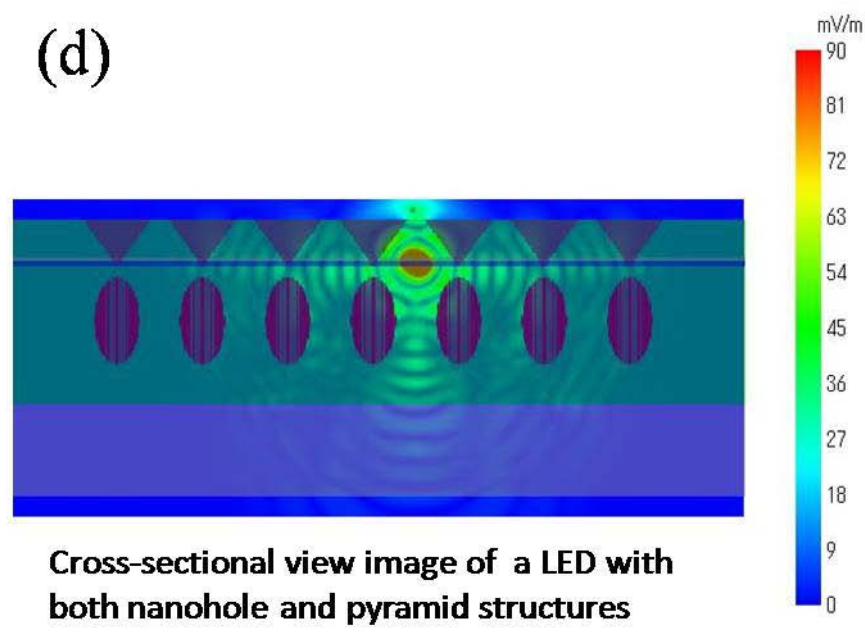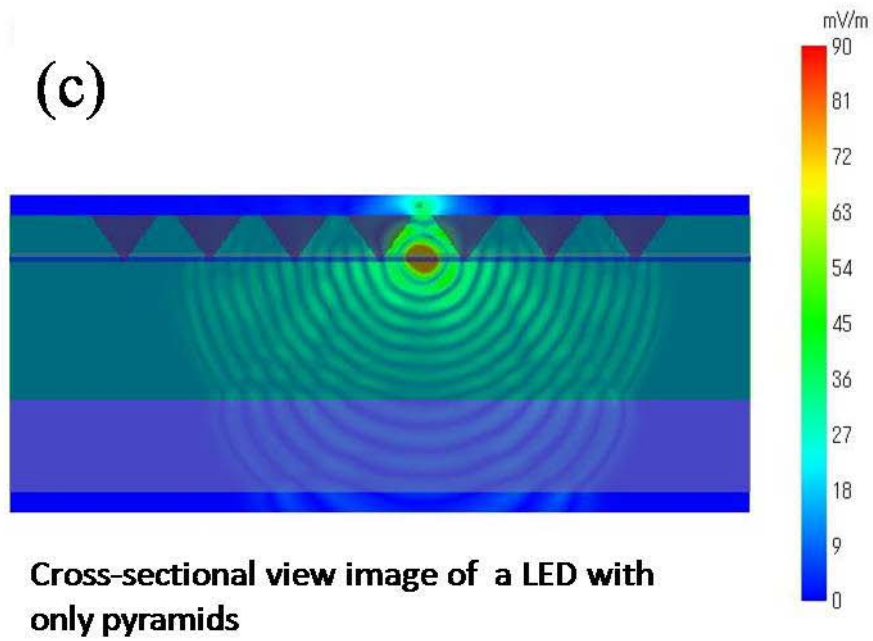
Fig. 6.27 The electromagnetic field distributions of the simulated structures at 11.25 fs.
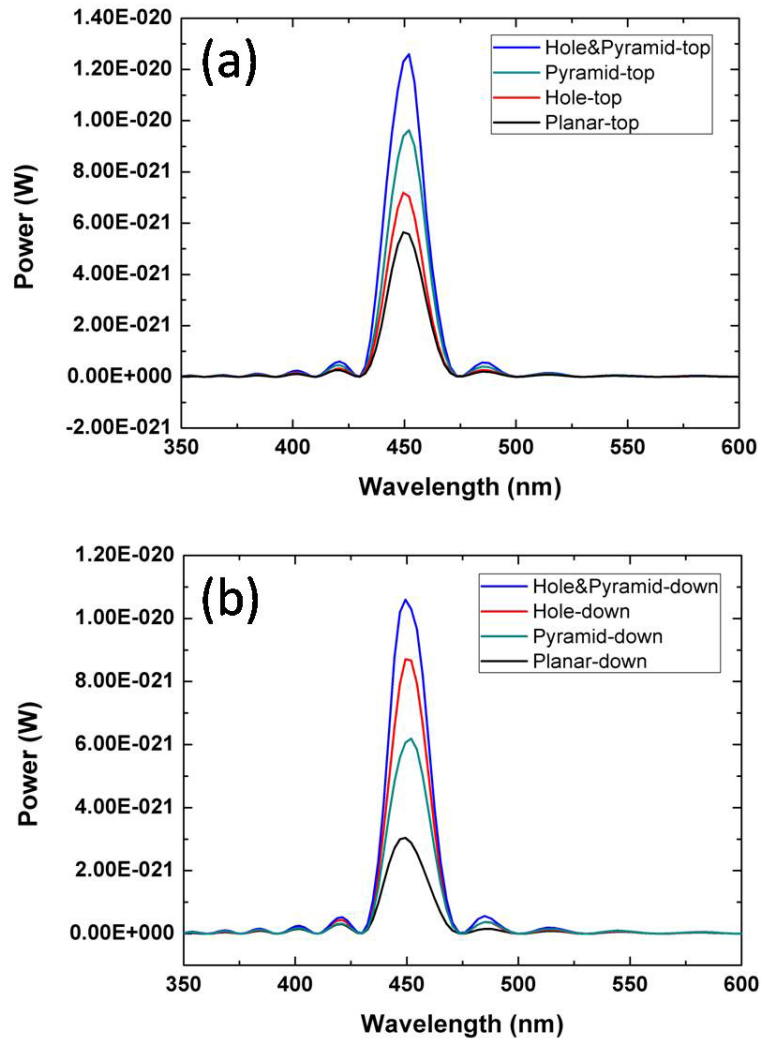
Fig. 6.28 The output power of light emission measured from the top surface (a)
and the bottom of the four LED structures (b).

The output power of light emission measured from the top surface and the bottom of the four

LED structures were shown in Figs. 6.28(a) and 6.28(b), respectively. We found the output power

from the top surface and bottom side were both enhanced by the nanostructures. The LED

structure with inverted pyramids had a larger output power from the top surface than the LED

structure with embedded voids. On the other hand, the LED structure with embedded voids

126

showed a larger output power from the back side than the LED with inverted pyramids. However, from both the top surface and the backside, the LED structure with both inverted pyramids and embedded voids showed the largest output power. The light extraction efficiency of the up and bottom directions exhibit as large as 2.2 and 3.5 times enhancement compared with the planar sample, respectively. The measured PL intensity enhancement is even slightly higher than the simulated value, probably due to an extra factor of better light coupling of the incident light at the nano-patterned surface. The calculated output power is small owing to the small sizes of the light source and simulated area as well as the short light emission time of 30 fs. This simulation result showed the great advantage of the LED structure grown on the nanohole templates in improving the light extraction efficiency.

6.5 Summary

In this chapter, InGaN/GaN MQWs grown on regular nanohole-patterned templates were studied. The nanohole template was measured to be almost completely strain relaxed. The integrated PL intensity of MQWs grown on a nanohole sample showed a 4-fold increase compared with a planar sample. The MQWs were coherently growth on the nanohole template. The slight red shift and the broader peak in PL spectrum were attributed to a thicker InGaN well width and a larger indium inhomogeneity. The light emission mainly came from the MQWs grown on c-plane, and the spatial distribution of the emission intensity and wavelength were

quite uniform. Two sets of nanoscale inverted pyramid and embedded void arrays were formed at the same time after growing the LED structure on a nanohole template. As high as 3.5 times increase in integrated PL intensity was observed for LED structure grown on a nanohole template compared with a planar sample owing to a much improved LEE. Although QCSE might be reduced by the strain relaxed nanohole template, the IQE of the nanohole based LED was measured to be lower than that of a planar LED, which implied a lower crystal quality of the MQWs grown directly on the nanohole template. This confirms that the great enhance of the PL intensity for the nanohole samples was attributed to the great improvement of the LEE. By simulation of the nanostructures with a FDTD software, it was confirmed that the distinct nanostructures exhibited the largest LEE compared with conventional nanostructures with only embedded voids or only inverted nanopyramids on the surface.

References

1) S. P. Chang, Y. C. Chen, J. K. Huang, Y. J. Cheng, J. R. Chang, K. P. Sou, Y. T. Kang, H. C. Yang, T. C. Hsu, H. C. Kuo, and C. Y. Chang: Appl. Phys. Lett. **100** (2012) 061106.

2) Y. H. Ko, J. H. Kim, L. H. Jin, S. M. Ko, B. J. Kwon, J. Kim, T. Kim, and Y. H. Cho: Adv. Mater. **23** (2011) 5364.

3) I. H. Wildeson, R. Colby, D. A. Ewoldt, Z. W. Liang, D. N. Zakharov, N. J. Zaluzec, R. E. Garcia, E. A. Stach, and T. D. Sands: J. Appl. Phys. **108** (2010) 044303.

4) C. H. Chiu, H. H. Yen, C. L. Chao, Z. Y. Li, P. C. Yu, H. C. Kuo, T. C. Lu, S. C. Wang, K. M. Lau, and S. J. Cheng: Appl. Phys. Lett. **93** (2008) 081108.

5) C. H. Liao, W. M. Chang, H. S. Chen, C. Y. Chen, Y. F. Yao, H. T. Chen, C. Y. Su, S. Y. Ting, Y. W. Kiang, and C. C. Yang: Opt. Express **20** (2012) 15859.

6) T. W. Yeh, Y. T. Lin, L. S. Stewart, P. D. Dapkus, R. Sarkissian, J. D. O'Brien, B. Ahn, and S. R. Nutt: Nano Lett. **12** (2012) 3257.

7) Y. J. Hong, C. H. Lee, A. Yoon, M. Kim, H. K. Seong, H. J. Chung, C. Sone, Y. J. Park, and G. C. Yi: Adv. Mater. **23** (2011) 3284.

8) C. Kisielowski, J. Kruger, S. Ruvimov, T. Suski, J. W. Ager, E. Jones, Z. LilientalWeber, M. Rubin, E. R. Weber, M. D. Bremser, and R. F. Davis: Phys. Rev. B **54** (1996) 17745.

9) S. Krylyuk, D. Paramanik, M. King, A. Motayed, J. Y. Ha, J. E. Bonevich, A. Talin, and A. V. Davydov: Appl. Phys. Lett. **101** (2012) 241119.

10) A. Najar, M. Gerland and M. Jouiad: J. Appl. Phys. **111** (2012) 093513.

11) V. Y. Davydov, N. S. Averkiev, I. N. Goncharuk, D. K. Nelson, I. P. Nikitina, A. S. Polkovnikov, A. N. Smirnov, M. A. Jacobsen, and O. K. Semchinova: J. Appl. Phys. **82** (1997) 5097.

12) C. H. Chiu, T. C. Lu, H. W. Huang, C. F. Lai, C. C. Kao, J. T. Chu, C. C. Yu, H. C. Kuo, S. C. Wang, C. F. Lin, and T. H. Hsueh: Nanotechnology **18** (2007) 445201.

13) Y. R. Wu, C. H. Chiu, C. Y. Chang, P. C. Yu, and H. C. Kuo: IEEE J. Sel. Top. Quantum Electron. **15** (2009) 1226.

14) V. Ramesh, A. Kikuchi, K. Kishino, M. Funato, and Y. Kawakami: J. Appl. Phys. **107** (2010) 114303.

15) C. B. Soh, S. Y. Chow, L. Y. Tan, H. Hartono, W. Liu, and S. J. Chua: Appl. Phys. Lett. **93** (2008) 173107.

16) Q. Li, Y. Lin, J. R. Creighton, J. J. Figiel, and G. T. Wang: Adv. Mater. **21** (2009) 2416.

17) T. Tanikawa, Y. Honda, M. Yamaguchi, and H. Amano: Phys. Status Solidi A-Appl. Mat. **208** (2011) 1175.

18) Q. Dai, M. F. Schubert, M. H. Kim, J. K. Kim, E. F. Schubert, D. D. Koleske, M. H. Crawford, S. R. Lee, A. J. Fischer, G. Thaler, and M. A. Banas: Appl. Phys. Lett. **94** (2009) 111109.

7. Conclusions and Prospects for Future Work

7.1 Conclusions

A novel thermal etching process in an MOVPE reactor for nanoporous template fabrication was proposed. This method shows the capability of fabrication very deep nanoporous templates with high density. This method is also threading sensitive, which may make it more effective in dislocation reduction. The diameter of the nanoscale pores could be tuned by the etching condition. Continuous NH_3 flow would greatly increase the aspect ratio of the anisotropic etching while pulsed NH_3 flow would laterally increase the pore diameter. The nanoporous template showed a nearly complete strain relaxation and a fivefold increase in PL intensity. The threading dislocation density after overgrowth was greatly reduced for the GaN template with poor crystal quality. The surface flatness of the GaN layer overgrown on the nanohole template was also obviously improved. However, little crystal quality improvement was observed for the high-quality GaN template. MQWs grown on a nanoporous template fabricated from the high-quality GaN template were used to assess the effect on LED performance. Owing to the increased light extraction efficiency caused by the nanoporous structure, MQWs grown on an overgrown nanoporous template exhibited a twofold increase in PL intensity.

Regularly distributed nanopyramid arrays were grown by selective area growth. We successfully suppressed the "self limiting growth" reported previously. Pyramid size was not limited by mask window but could be controlled by growth parameters. The pyramids exhibited uniform size and no abnormal large islands were observed throughout the whole sample. Distinct

nanostructures were observed for nanopyramids. In every nanopyramid an embedded void was observed, which was explained by different growth rates at the edge and center of the window region caused by SAG and a low diffusion length. Two PL emission peaks from MQWs grown on the nanopyramids were observed. The longer wavelength peak originated only from the apexes of pyramids with a shape of threefold symmetry. The formation of pyramids of threefold symmetry might be related to the high-density stacking faults formed during the growth according to the TEM analysis. This approach has potential merits such as fast p-GaN coalescence, larger light emitting area, as well as dislocation reduction by lateral overgrowth. This research could be used for realizing nanopyramid based high-efficiency LEDs in the future.

MQWs as well as full LED structures grown on regular nanohole-patterned templates were studied. The nanohole template was measured to be almost completely strain relaxed. The integrated PL intensity of MQWs grown on a nanohole sample showed a 4-fold increase compared with a planar sample. The light emission mainly came from the MQWs grown on c-plane, and the spatial distribution of the emission intensity and wavelength was quite uniform. Two sets of nanoscale inverted pyramid and void arrays were formed at the same time after growing the LED structure on a nanohole template. As high as 3.5 times increase in integrated PL intensity was observed for LED structure grown on a nanohole template compared with a planar sample owing to a much improved light extraction efficiency. This study suggests the nanohole-patterned template as an promising nanostructure for realizing high efficient LEDs.

7.2 Future Work

For GaN templates with high dislocation density, the dislocation density could be greatly reduced by GaN layer overgrowth on the thermally etched nanoporous template. However, for high-quality GaN templates, the dislocation reduction was not obvious. The origin of this difference is still not clear. A further study of the dislocation reduction mechanism and a comparison between GaN templates with different dislocation density are required in the future. This may lead to an optimization of the nanoporous structure for high-quality overgrown GaN layers.

The thermal etching conducted inside the MOVPE chamber offers a possibility to integrate the nanoporous template fabrication with the crystal growth process. GaN overgrowth could be performed directly after the thermal etching process without removing the SiO_2 mask. This will not only reduce the complexity of the regrowth step but may also provide a further dislocation reduction. Previously GaN overgrowth with nanoscale patterned dielectric mask has been reported for effective dislocation reduction. However, we found the coalescence of the overgrown GaN was very difficult despite of the nanoscale pattern. The growth condition optimization is required in the future.

We have successfully suppressed the "self-limiting" growth during GaN nanopyramid growth. The size of the nanopyramid array was uniform throughout the whole sample and could be well controlled by growth parameters. Using the present growth condition, however, we found

embedded nano voids inside every pyramids. Besides, there were also new dislocations generated at the regrowth interface. These issues might be solved by first growing a nanopyramid "core" with hydrogen as carrier gas at a higher temperature. The growth condition optimization is necessary.

For MQW and LED structures grown on the GaN nanohole templates, greatly enhanced PL intensity was observed and was attributed to the improved light extraction efficiency. LED devices based on the GaN nanohole template have also be fabricated and tested. However, the electroluminescence showed quite weak output power possibly due to the poor quality of the p-GaN layer. The optimization of the LED growth condition and demonstration of LED device requires further study in the future.

Acknowledgments

I sincerely thank Professor Hiroshi Amano for offering the opportunity to join his research group and for his support and guidance throughout this work. His beneficial comments and discussions, encouragements and support have made my research in Nagoya University an enjoyable experience.

I would like to thank my committee members: Professor Hirotaka Toyoda in Department of Electrical Engineering and Computer Science, Nagoya University, Professor Yutaka Ohno in Department of Quantum Engineering, Nagoya University and Professor Kazuyuki Tadatomo in Graduate School of Science and Engineering, Yamaguchi University, for their valuable suggestions and comments on my research.

I would also like to thank Professor Masahito Yamaguchi and Professor Yoshio Honda for their valuable comments and advices, and for their support throughout my graduate career.

I would like to thank Dr. Tomoyuki Tanikawa, Dr. Takayuki Sugiyama, Dr. Kouji Okuno, Dr. Ji-Su Son, Dr. Tadashi Mitsunari, Dr. Maki Kushimoto, and all the other members in our lab for endless help with my experiments. This work could not be completed without your help!

I would like to give sincere acknowledgement to Kato san, Neishi san and Kikuta san in Tokyo Electron Limited, for their valuable discussions and suggestions and tremendous help in

experiments using #6 MOCVD.

Finally, I would like to thank my parents for their unconditional love and support.

It's their encouragement and comfort gave me strength to overcome all the obstacles.

Research Achievements

I.   Presented Paper

（1）C. Miao, H. Lu, X. Z. Du, Y. Li, R. Zhang and Y. D. Zheng;

"InGaN/GaN multi-quantum-well planar metal-semiconductor-metal light-emitting diodes",

Electron. Lett. **44** (2008) 441.

(2) Z. Xue, H. Lu, <u>C. Miao</u>, D. J. Chen, R. Zhang and Y. Zheng;

"Low-dark-current metal-semiconductor-metal ultraviolet photodetector fabricated on homoepitaxial GaN",

Electron. Lett. **45** (2009) 651.

(3) C. Miao, H. Lu, D. J. Chen, R. Zhang, and Y. D. Zheng;

"InGaN/GaN multi-quantum-well-based light-emitting and photodetective dual-functional devices",

Front. Optoelectron. China **2** (2009) 442.

(4) C. Miao, Y. Honda, M. Yamaguchi, and H. Amano;

"GaN Overgrowth on Thermally Etched Nanoporous GaN Template",

Jpn. J. Appl. Phys. **52** (2013) 08JB03.

(5) J. S. Son, C. Miao, Y. Honda, M. Yamaguchi, H. Amano, Y. G. Seo, S. M. Hwang, and K. H. Baik;

"Effects of Nano- and Microscale SiO2 Masks on the Growth of a-Plane GaN Layers

on r-Plane Sapphire",

Jpn. J. Appl. Phys. 52 (2013) 08JC04.

(6) C. Miao, Y. Honda, M. Yamaguchi, and H. Amano;

"Growth of InGaN/GaN multiple quantum wells on size-controllable nano-pyramid

arrays",

Jpn. J. Appl. Phys., accepted.

II.   International Conference

(1) C. Miao, Y. Honda, M. Yamaguchi, and H. Amano;

"GaN Overgrowth on Thermally Etched Nanoporous GaN Template",

International Workshop on Nitride Semiconductors (IWN 2012)

(2) J. S. Son, C. Miao, Y. Honda, M. Yamaguchi, H. Amano, Y. G. Seo, S. M. Hwang,

and K. H. Baik;

"Optical property of a-plane GaN grown on r-plane sapphire using nano- and

microscale SiO_2 masks",

International Workshop on Nitride Semiconductors (IWN 2012)

(3) C. Miao, Y. Honda, M. Yamaguchi, and H. Amano;

"InGaN/GaN Multiple-Quantum Wells Grown on Nanohole-Patterned Templates",

5th International Symposium on Advanced Plasma Science and its Applications for

Nitrides and Nanomaterials (ISPlasma 2013)

(4) C. Miao, Y. Honda, M. Yamaguchi, and H. Amano;

"Light emitting diodes grown on nanohole-patterned GaN templates",

10th International Conference on Nitride Semiconductors (ICNS 10th 2013)